Université catholique de Louvain
École Polytechinique de Louvain
ICTEAM Electrical Engineering

Université libre de Bruxelles
École Polytechnique de Bruxelles
OPERA Dpt. Wireless Communications Group

Cooperative Wireless Channel Characterization and Modeling:

Application to Body Area and Cellular Networks

PAR

Lingfeng Liu

THÈSE PRÉSENTÉE EN VUE DE L'OBTENSION DU GRADE DE DOCTEUR EN SCIENCES DE L'INGÉNIEUR

Composition du Jury

Prof. Claude Oestges (Advisor)	UCL, Belgium
Prof. Philippe De Doncker (Advisor)	ULB, Belgium
Prof. Danielle Vanhoenacker-Janvier	UCL, Belgium
Prof. Christophe Craeye	UCL, Belgium
Prof. François Horlin	ULB, Belgium
Prof. Jean-Michel Dricot	ULB, Belgium
Dr. Raffaele D'Errico	CEA-LETI, France

Mars 2012

Acknowledgements

First, I would like to express my greatest gratitude to my advisors, Prof. Claude Oestges and Prof. Philippe De Doncker, for their guidance, patience, encouragement, and enthusiasm to my study. This work won't be finished without their supports and advices. I am always inspired by their rich experience and insight. Their positive altitudes lead me through the doubts and drive me to step forward. I want to specially thank Prof. Claude Oestges for his generous contributions of time and funding that help me to concentrate on my research.

I would like to give my sincere gratitude to Prof. Christophe Craeye and Dr. Farshad Keshmiri for a really good joint research experience during my study. I learned a lot from Prof. Christophe Craeye and I am impressed by his enthusiasm in science. I appreciate Mr. Farshad Keshmiri for his sage advices, active participation, and well cooperation in some of the most important measurements in the study.

I would like to thank the jury, Prof. Danielle Vanhoenacker-Janvier, Prof. François Horlin, Prof. Jean-Michel Dricot, and Dr. Raffaele D'Errico, for their time, comments, and concerning to my work.

I would like to thank my colleagues, Mr. Vaibhav Bhatnagar, Dr. Stéphane Van Roy, and Dr. François Quitin for their cooperation, assistance, and discussion in various projects.

I want to thank Dr. Katsuyuki Haneda, Dr. Juho Poutanen, Prof. Fredrik Tufvessen, Dr. Nicolai Czink for their active participation and discussion, which have inspired a great part of the achievement in this work.

I want to also thank the technicians of the WELCOME lab and ICTEAM department, particularly to Mr. Pascal Simon, for their technical and logistical assistance.

Finally and most importantly, my special thanks go to my wife Qin for her patience, understanding, and support during the hardest time of writing this dissertation. The joy and happiness she brings to my life are the biggest motivations all these years to keep me a great passion in the work.

Contents

List of Figures

List of Tables

List of Acronyms

AoA	Azimuth-of-Arrival
AoD	Azimuth-of-Departure
BAN	Body Area Network
BER	Bit Error Rate
BLE	Bluetooth Low Energy
BS	Base Station
CDF	Cumulative Density Function
CIR	Channel Impulse Response
CMC	Correlation Matrix Co-linearity
CoMP	COordinated Multi-Point
CSI	Channel State Information
CW	Continuous Wave
DF	Decode-and-Forward
DMC	Dense Multipath Component
DoA	Direction-of-Arrival
DoD	Direction-of-Departure
ECG	electrocardiography
EEG	electroencephalography
EoA	Elevation-of-Arrival
EoD	Elevation-of-Departure
FDTD	Finite-Difference Time-Domain
GSCM	Geometry-based Stochastic Channel Model
ISM	Industrial, Scientific and Medical

iid	independent and identically distributed
LOS	Line-Of-Sight
LSP	Large Scale Parameter
LTE	Long-Term-Evolution
MIMO	Multi-Input Multi-Output
MISO	Multi-Input Single-Output
MPC	Multi-Path Component
MLE	Maximum Likelihood Estimator
MS	Mobile Station
MSE	Mean Square Error
NLOS	Non Line-Of-Sight
PDF	Probability Density Function
PSD	Power Spectrum Density
QPSK	Quadrature Phase Shift Keying
Rx	Receiver
SISO	Single-Input Single-Output
SIMO	Single-Input Multi-Output
SNR	Signal-to-Noise Ratio
STBC	Space Time Block Coding
STD	Standard Deviation
Tx	Transmitter
UWB	Ultra Wideband
V2V	Vehicle-to-Vehicle
VNA	Vector Network Analyzer
VR	Visibility Region

List of Symbols

Common symbols in Parts I & II:

$\vec{\bullet}$	Basis of direction vector
$\hat{\bullet}$	Estimated value
$\bullet^H$	Hermitian transpose
δ	Dirac function
γ	SNR
Λ	Eigenvalue
λ	Wavelength
μ	Mean
ϕ	Azimuth
$\mathbf{\Omega}$	Direction vector
ω	Rad
σ	STD
τ	Delay
θ	Elevation
a	Complex amplitude of MPC
C	Capacity
c_0	Wave speed
d	Distance
$E[\bullet]$	Expectation operator
E_s	Transmit power
err	BER
f	Frequency
f_D	Doppler frequency shift

$\mathbf{H}$	MIMO channel matrix
$\mathbf{I}$	Identity matrix
h	Channel impulse response
j	Imaginary unit
L	Pathloss level
N_0	Noise level
$\mathcal{N}(\mu, \sigma)$	Normal distribution function
P_{out}	Outage probability
Pr	Probability
r	Radius
$\boldsymbol{s}$	Antenna / antenna array steering vector
t	Time
U	Random variable following a truncated normal distribution
W	Random variable following a normal distribution

Symbols in Part I:

ϵ_0	Electric permittivity in free space
ϵ_c	Electric permittivity of cylinders
μ_0	Magnetic permeability in free space
μ_c	Magnetic permeability of cylinders
$\rho_{x,y}$	Correlation coefficient between x and y
ρ	Radial coordinate
σ_F	Temporal fading STD
θ_{24}	Angular difference between channels S_{21} and S_{41} in $\vec{z} - V$ scenarios of canonical measurements
$\boldsymbol{A}_{line}$	Vector potential
a_D	Additional local spread parameter of Doppler PSD model

a_k	Integration path in analytical model
$B(a_B, b_B)$	Beta distribution with parameters a_B and b_B
D	Destination node
E_α	Eletronic field along $\vec{\alpha}$
g_{div}	Diversity gain
H_α	Magnetic field along $\vec{\alpha}$
$H_n^{(2)}$	Hankel function of the second kind at order n
I	Magnitude of current intensity
$\boldsymbol{I}$	Current intensity vector
$\boldsymbol{J}$	Current source vector
J_n	Bessel function of the first kind at order n
k	Wavenumber
k_α	Wavenumber along $\vec{\alpha}$
l_k	Scaling factor of integration contour in analytical model
n_F	Temporal fading STD increasing rate
n_L	Pathloss increasing rate
R	Relay node
R_ϕ	Antenna radiation pattern at azimuth ϕ
S	Source node
S_{xy}	S-parameter
s	Transmission symbol
s_D	Overall spread parameter of Doppler PSD model
x_D	Extra decaying parameter of Doppler PSD model

Symbols used in Part II:

Δ_C	Cluster delay spread

η	Cluster BS-commonness ratio
κ_τ	Decaying factor of clusters
κ_{DMC}	Decaying factor of clusters
$\phi_{C,MS}$	Cluster's AoA
$\phi_{C,BS}$	Cluster's AoD
Φ_C	Cluster's distribution angle
Θ_C	Cluster's distribution angle
$\boldsymbol{\rho}$	Correlation matrix
ρ_C	VR density
τ_0	LOS delay
τ_B	Cut-off delay of cluster attenuation
τ_C	Cluster delay
$\tau_{C,link}$	Cluster-link delay
$\theta_{C,MS}$	Cluster's EoA
$\theta_{C,BS}$	Cluster's EoD
φ	Random phase of MPC polarization components
ζ	Power factor of LOS
$\boldsymbol{A}$	Cholesky factorization of correlation matrix $\boldsymbol{\rho}$
A_C	Cluster attenuation
A_{LOS}	LOS attenuation
A_{MPC}	Complex intra-cluster MPC fading
A_{VR}	Visibility gain
a_C	Extend of cluster in space that leads the delay spread
B	Bandwidth
b_C	Extend of cluster in space that leads the azimuth spread
$\mathscr{C}$	Set of visible clusters

f_c	Carrier frequency
$\boldsymbol{G}$	MPC polarization matrix
g_i	Weight of power allocation on the ith eigen-channel
h_C	Extend of cluster in space that leads the elevation spread
K_{sel}	K-selection factor of twin cluster ratio
L_C	Width of transition region
L_m	Number of VRs that are connected to m BSs
N_C	Average number of visible clusters
n_{VR}	Number of VR in the VR group of a remote cluster
R_C	Size of visibility region
R_{LOS}	VR size of LOS
SF	Shadow fading
t_{total}	Total lifetime of cluster
t_{VR}	Lifetime of cluster in single VR

CHAPTER 1

Introduction

1.1 Cooperative wireless communications

In recent years, an intensive emergence of wireless applications is bringing great challenges to the design of smart and efficient wireless communication systems. To support faster and more robust data transmission under intricate demands by these applications and in various networks, wireless systems must overcome the decaying and fading radio channels in order to improve the link quality in terms of the trade-off between data rate and outage/throughput, and spectrum efficiency. The complex contexts of the applications further require the systems to be context-aware and adaptive to the environments. Although wireless technologies have experienced a revolutionary development to meet these challenges, conventional point-to-point (single-link) communications are fundamentally restricted by the resource limitation, signal interference, and channel impairment. This urges advanced communication paradigms to exceed the single-link limitations to further improve the communication performance in future wireless systems.

Under this background, cooperative communications are receiving increasing interest for their potentials to exploit the channel spatial spectrum. The concept of cooperative communication was first described in relay networks by Cover and El Gamal in [CG79] and other classic studies in [LTW04,NBK04,KMY07,NG06], showing significant diversity gains achieved in cooperative relays. Later, this concept was generalized into multi-link communications and was described based on the physics of radio channels.

The basic idea of cooperative communications is to coordinate terminals across multiple links to form virtual antenna arrays and distributed Multi-Input Multi-Output (MIMO) systems. Such coordination can be realized asynchronously as in relay networks, or synchronously as in general multi-link communications. The advantages of MIMO systems on the spectrum efficiency have already been widely acknowledged in point-to-point communications. Based on coordination among the antennas in collocated antenna arrays, MIMO systems benefit from the exploitation of the channel spatial spectrum by the well-known spatial diversity and/or spatial multiplexing [ZT03, GJJV03]. Because of the broadcast and stochastic nature of wireless channels, such channel spatial spectrum can also be exploited more widely in the environment with great potential. This allows cooperative communications in multiple links to achieve diversity and capacity gains analogue to collocated MIMO systems.

There are three basic types of cooperation over time and space:

1. Cooperative relay
2. Transmitter cooperation
3. Receiver cooperation

where type 1 refers to relay networks, and type 2 and 3 refer to cooperation in general multi-link communications.

Cooperative multi-link communications bring two attractive advantages over single-link MIMO systems: 1) deploying multiple antenna arrays in collocated MIMO systems is costly in most wireless networks especially at the user terminals, while distributed MIMO systems offer a more flexible solution to achieve the spatial diversity and capacity gains; 2) user-cooperation [NHH04] and COordinated Multi-Point (CoMP) transmission [KFV06] can group individual MIMO systems to further enhance the data transmission. The second issue has been considered in the LTE-Advanced as the future solutions to improve the mobile communications in LTE/3GPP. In short, cooperative communications generalize the approach applied in collocated MIMO systems to exploit the huge potential of channel spatial spectrum beyond single-link communications.

1.2 Cooperative multi-link channels

One of the primary parameters of radio channels in cooperative multi-link communications is the spatial channel correlation or cross-channel correlation on different links. Moreover, the spatial dependence of the channel properties, such as the pathloss and fading, is also important to affect the cooperation performance. These aspects are not covered in single-link channel models and it essentially requires a more fundamental understanding on the physical mechanisms of radio propagation in space. Our study concerns two important features of multi-link channels in future wireless networks as stated below.

First, describing multi-link channels will heavily resort to spatial channel characterization and geometry-based modeling approaches. Describing radio propagation in spatial and angular domains is much more complex than in time and frequency domains, because the exact physical interactions of radio waves with the environment have to be explained. Modeling multi-link channel models require a more global description of such interactions to cover distributed terminals. Meanwhile, keeping the consistency between single-link channel and multi-link channel descriptions will be important to make the models backward compatible. These bring many challenges to the estimation and complexity control of multi-link channel modeling.

Second, future wireless systems will be intensively related to the application contexts and environments. The systems will have distinct emphases, e.g. on the terminal mobility as in Vehicle-to-Vehicle (V2V) communications [MTKM09, WCL09], or on the communication ranges as in Femtocell [CAG08] and Body Area Networks (BANs) [ZLK07]. Communications in specific contexts do not only differ in performance requirements, but also differ in the physical mechanisms of radio propagation. Therefore, the physical differences of radio propagation in different contexts should be well understood to correctly model the channels.

1.3 Motivation and dissertation outline

This dissertation presents the research results of multi-link channel characterization and modeling in various networks. The research has been involved in several scientific activities, including the WALIBI (Wireless Acquisition and LInk for Body Information) project founded by the Wallon, Belgium, the COST 2100 action, and the NEWCOM++ network of excellence. The primary goals of the study are: 1) to characterize and model the spatial cross-channel correlations in multi-link communications; 2) to characterize and model the spatial dependence of channel properties. Two types of networks have been investigated in the study: body area and cellular mobile networks. On the one hand, the study has focused on different aspects in both networks because of their distinct propagation mechanisms. On the other hand, in both networks, we have resorted to geometry-based channel modeling methods and described the spatial channel correlation by the so-called scattering commonness. In doing so, we will highlight the common problems, solutions, and system benefits of cooperative multi-link channel modeling in different networks.

1.3.1 Cooperative channel modeling in body area networks

The study in BANs focuses on the radio channels on the body surface. As BANs are featured as small-scale and body-centric networks, the physical mechanisms of BAN propagation are expected to be distinct from conventional large-scale propagation. Therefore extensive on-body measurements were conducted, serving as both preliminary understanding of the physical propagation mechanisms and advanced spatial characterization of radio channels in BANs. The study puts a particular emphasis on the aspects of near-field propagation and dynamic body scattering, which are typically observed in BANs. The dissertation in this part is organized as follows.

Chapter 2 introduces the backgrounds of BANs and the radio propagation in the body area.

Chapter 3 and Chapter 4 present measurement results and statistical modeling of time-varying on-body channels, including canonical on-body channel measurements in anechoic environments and scenario-based on-body channel measurements in realistic environments.

Chapter 5 presents a closed-form analytical model to describe the static and dynamic body scattering. The model is validated through deterministic and statistical comparisons to the measurement results. Later, the model is applied to characterize the modification of on-body antenna radiation pattern in off-body communication by the body scattering.

Chapter 6 evaluates the channel impacts to simple cooperative protocols deployed in on-body communications based on the measurements made in realistic environments. Relay networks and distributed MIMO communications are evaluated by the capacity and diversity gains achieved in the cooperation.

1.3.2 Multi-link MIMO channel modeling

The study on multi-link MIMO channel modeling in cellular mobile networks is based on the single-link and multi-link COST 2100 MIMO channel model. Our work was a joint study carried out under the framework of the COST 2100 action, with participants from Aalto University, Finland, Lund University, Sweden, UCL, and ULB. The major part of the study includes: 1) supplementary modeling, complete parameterization and implementation of the single-link COST 2100 model; 2) modeling of multi-link MIMO channels based on the structure of the COST 2100 model. The dissertation in this part is organized as follows.

Chapter 7 gives a short introduction to MIMO channel modeling methods.

Chapter 8 presents the basic structure, concepts, and parameters of the single-link COST 2100 model.

Chapter 9 presents the multi-link extension of the COST 2100 model by introducing the concept of cluster link-commonness.

Chapter 10 presents the implementation details of the COST 2100 model. An implementation example is presented at the end of this chapter.

Chapter 11 evaluates the influence of cluster link-commonness to multi-link communications by comparing the sum-rate capacities of distributed MIMO systems under different cluster link-commonness ratios.

Part I

Cooperative channels in body area networks

CHAPTER 2

Introduction to body area networks

2.1 Backgrounds

BANs are body-centric wireless networks deployed in a close range of the human body [XZ09]. Technically, BAN is a general concept to enable body-centric data transmissions as proposed by early work in [DPB01]. In 2007, the IEEE established a standardization group, known as IEEE 802.15 TG6 [IEE], to develop BAN communication standards that optimize the performance in low-power devices. A formal definition of BAN given by IEEE 802.15.6 is "*communications for low-power devices and operation on, in or around the human body (but not limited to humans) to serve a variety of applications including medical, consumer electronics / personal entertainment and others*". The emphases on the transmission scale, power consumption, and operating environment make BAN distinct from the other networks.

In the fast growth of personal wireless voice and data communications, BANs offer local-body data transmissions that are particularly suitable to convey physiological signals. This makes BAN a promising and key technology to realize wireless medical services as intensively studied in [LhH09, SAF+08]. Future medical applications like remote diagnosis and monitoring expect BANs to free the patients from the cables and transmit the medical data in a more economic, flexible, and comfortable way. The potentials of BANs have also attracted applications on a more general background. Some of the most interesting ones are:

1. Wireless healthcare
2. Sports and body motion monitoring
3. Personal multimedia transmission
4. Secured personal data exchange

BANs cover a wide range of frequencies. In [Rei09], it is shown that the following frequency bands are considered by IEEE 802.15.6 and other studies:

1. Industrial, Scientific and Medical (ISM) bands at 400, 600, 900 MHz

2. ISM bands at 2.4 GHz

3. Ultra Wideband (UWB) at 3-10 GHz

Among these frequency bands, the 400, 600, and 900 MHz bands are typical medical radio bands. UWB is attractive to meet the BAN requirements because of its short communication range and power-efficient technique developed, as studied in [AHH$^+$06,vROHDD10]. The 2.4 GHz band is widely applied in the design of BANs because it has a larger bandwidth than the 400, 600, and 900 MHz bands to support higher data rates. Moreover, the functions of BANs can be partially realized by the existing short-range wireless standards operating at 2.4 GHz, such as the Bluetooth Low Energy (BLE), Zigbee [Zig], and ANT+ [ANT], which offer alternative solutions of BANs.

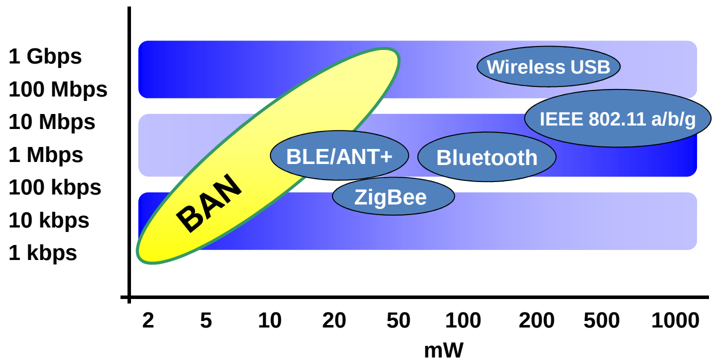

Figure 2.1: Comparison of BAN and other wireless standards at 2.4 GHz

Fig. 2.1 compares the requirements on the power consumption and data rate of BANs to various wireless standards at 2.4 GHz. Ideal BANs are expected to operate in ultra-low power and support a large dynamic range of data rate because the communication range is quite limited. Low-power standards such as the BLE are likely to meet these requirements, but the trade-off between the power consumption and data rate in these standards need to be further optimized to support generic BAN communications. In addition, designers should also handle the interference [HMRG09] as well as the security [LLR10] problems in both physical and network layers.

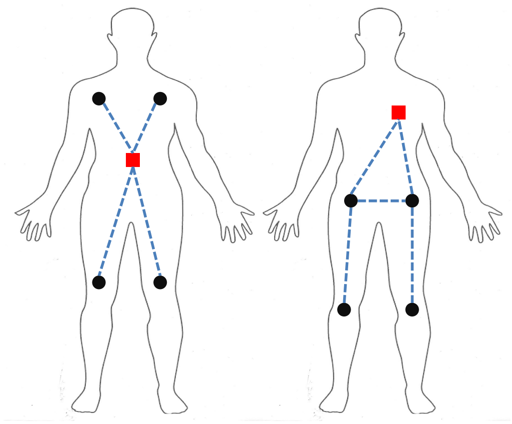

Figure 2.2: Two parctical topologies of BANs, star (left) and mesh (right) topology. Both topologies are supported by a central coordinator (square) as the master node, and distributed sensors (circles) as the slave nodes

Practical BANs are usually deployed by battery-powered devices or sensors. To guarantee the data transmission under strict power consumption, the networks usually consist of one master node that coordinates, collects, and proceeds the data from the sensors (slave nodes). This configuration can be realized in a star or mesh topology as described in Fig. 2.2. The mesh topology can play a relaying role to alleviate the signal loss in long distance transmissions, e.g. from the foot to the chest. The topologies should support transmissions from both single sensor and multiple sensors depending on the signals, e.g. the simple pulse rate or the complex electrocardiography (ECG) / electroencephalography (EEG) signals. Considering the above requirements, BANs should be designed as scalable, context-aware, and capable to connect to outer networks to extend the range of BAN services.

2.2 Radio propagation in BAN

BANs usually operate under low Signal-to-Noise Ratios (SNRs) because of the power limitation. Therefore, links are sensitive to the influences of decaying (pathloss) and fluctuation (fading) from the radio channels. Radio propagation in the range of body area is different from the radio propagation in large-scale networks. The difficulties to describe BAN propagation can be found in the following aspects:

1. Radio propagation in BAN usually occurs in a distance comparable to the wavelength. It belongs to near-field propagation with a more complex electromagnetic description than the plane-wave assumption in far-field propagation.

2. Links in BANs are formed with the presence of a strong and complex interference from the body scattering. Because of various compositions, shapes, and motions of the body, such scattering effects show large variation in time and space.

3. The deterministic and stochastic properties of BAN channels are highly scenario-dependent with respect to the link geometries, polarizations, body motion modes, and off-body environments. A proper scenario classification will be critical to develop efficient BAN channel models.

4. The implanted and on-body communication nodes are heavily coupled with the body. In practice, it is difficult to separate the impacts of the devices from the physical channels, which further increases the analysis difficulty.

2.2.1 Classification of BAN communication scenarios

IEEE 802.15.6 introduces a four-layer cascaded classification of the communication scenarios in BAN, covering different emplacements of the communication nodes: implanted, on-body, and off-body. Fig. 2.3 depicts this classification, where different layers are labeled as CM_i $i = 1, 2, 3, 4$.

$\mathbf{CM}_1$ refers to the wireless communication between two implanted nodes, named in-body communication. CM_1 primarily serves medical applications. The bio-tissues constitute a highly lossy environment

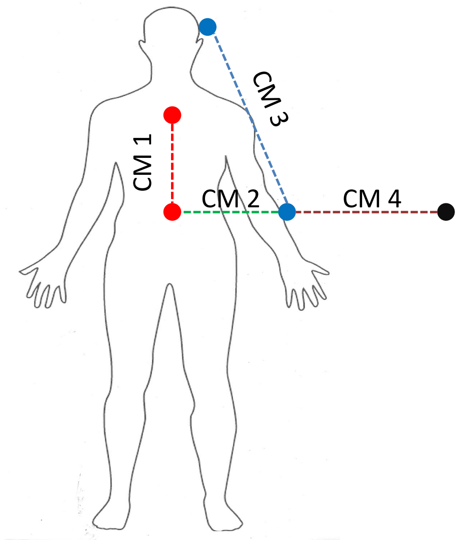

Figure 2.3: Four-layer classification of BAN communication scenarios by IEEE 802.15.6. CM_1 represents in-body communications, CM_2 represents in-body-to-on-body communications, CM_3 represents on-body communications, and CM_4 represents off-body communications

to the implanted nodes. Therefore low frequency bands at e.g. 400, 600, 900 MHz are suggested for CM_1 [YK07].

CM$_2$ refers to the wireless communication between an implanted nodes and an on-body nodes, named in-body-to-on-body communication. It can also serve medical applications e.g. to send out the data from implanted devices and to send back control signals. Similarly to CM_1, large in-body signal loss is anticipated in CM_2 as the radio waves must travel across the bio-tissues and the air [CNHM10].

CM$_3$ refers to the wireless communication between two on-body nodes, named on-body communication. On-body communications constitute the primary part of local-body wireless transmission. Signals in CM_3 receive significant impacts from both the body and the environment, which are much more complicated than in CM_1 and CM_2. This is the major communication scenario studied in our work.

CM_4 refers to the wireless communication between an on-body node and an off-body nodes, named off-body communication. Off-body communications offer connections of BANs to outer networks. The communications are more impacted by the environment while the body scattering effect is still significant.

2.2.2 Body propagation modes

Depending on the regions where the propagation occurs, there are three basic types of BAN propagation: in-body, on-body, and off-body.

2.2.2.1 In-body propagation

In-body propagation is the radio propagation inside the body in CM_1 and CM_2. The bio-tissues of the body constitute a stationary and lossy environment with little influences from the outside. Consequently, studies of in-body channels mainly focus on the pathloss, as in [SPYH$^+$09].

2.2.2.2 On-body propagation

On-body propagation in CM_3 is the radio propagation on the surface of the body. Due to the lossy properties of the body, radio waves, particularly at 2.4 GHz and UWB, will decay fast when they are penetrating the body [MBea04]. Therefore, the interaction between the waves and the body is restricted on the body surface.

On-body propagation is formed with a strong influence from the body scattering, which is usually represented by surface waves (creeping waves) [AANH10, APL11]. In Line-Of-Sight (LOS) conditions, the body scattering leads to high pathloss levels in short distance [vROHDD10]. In Non Line-Of-Sight (NLOS) conditions where the nodes are shadowed by the body, the signals are guided by the surface waves (creeping waves) to travel around the body [APL11]. For the above reasons, the effective propagation distances of on-body channels are usually measured on the body surface instead of in free-space.

Human body is a complex propagation environment. It contains different compositions and shapes, e.g. in legs, arms, trunk, and head. It also takes various postures and motions in distinct spatial and temporal patterns. Making a generic channel description covering different body parts and motion modes is usually impractical, while propagation scenarios should be well specified to describe the scattering differences.

Body scattering impacts the on-body channel fading in both spatial and temporal domains.

In the spatial domain, the shape and composition variety of different bodies can cause the variation of on-body pathloss in different link geometries.

In the temporal domain, different body motions, such as the active motions (walking, running, etc.) and passive motions (breathing, etc.), will lead to different dynamics that affect the temporal variation of on-body channels [LDDO09, DO09]. On-body channels in dynamic scenarios can be further classified by the mobility of the nodes based on their emplacements on the body. In general, there are three types:

1. A *fixed-fixed* on-body channel has both nodes placed on static parts of the body without relative movements. The moving parts of the body form dynamic scatterers to the channel.

2. A *fixed-mobile* on-body channel has one node placed on a moving part and the other one placed on a static part of the body. Consequently, the propagation distance between the nodes varies along with the movement of the body. Therefore, the temporal variation of the channel is caused by: 1) the pathloss variation due to the varying of propagation distance; and 2) the dynamic body scattering.

3. A *mobile-mobile* on-body channel has both nodes placed on moving parts of the body. The dynamic range of the distance between the nodes will further increase and create larger temporal variation of the channel than fixed-mobile on-body channels.

2.2.2.3 Off-body propagation

Off-body propagation is the propagation between the body and the off-body environment. Off-body propagation can be found in CM_4 between an on-body node and an off-body device. On-body communications in realistic environment also receive off-body propagation components like the ground reflection. In realistic applications, scattering from the off-body environment may improve the gain of an on-body link, since it brings extra power to the link, as observed in [DO09]. Due to the lossy behavior of the body, multiple scattering between the environment and the body is usually negligible, and is ignored in our study.

Off-body propagation usually occurs over distance long enough to be described as far-field propagation by plane-waves. It can then be described by the channel characterization and modeling methods in conventional large-scale networks, such as the Multi-Path Component (MPC) effects. The influence of body scattering to off-body propagation should be considered at the body side [LVRDDO09], which is usually independent from the off-body scattering.

2.3 Overview of channel characterization issues

2.3.1 On-body pathloss

Compared with the pathloss of radio propagation through space, pathloss on the body surface is featured by the near-field propagation, body coupling, and surface waves. The difficulties to characterize on-body pathloss can be found in the following aspects:

1. On-body pathloss differs largely under different link geometries and polarizations.

2. Defining the pathloss for fixed-mobile and mobile-mobile on-body channels is difficult, because the propagation distances will fluctuate along with the body motions.

3. Large spatial variation of on-body pathloss is expected in realistic applications due to subject differences and device displacements.

There are two statistical on-body pathloss models that are dependent on the on-body propagation distances. The first one is an exponential model, expressed in dB as:

$$L_{dB} = L_0 + 10n_L \lg(d/d_0), \tag{2.1}$$

where L_0 is the reference pathloss at distance d_0. Eq. 2.1 is found effective when the communication nodes are in LOS condition [MBea04, FDR+05].

Other studies like in [RDDM+04, LDDO09] suggest linear pathloss model in dB as:

$$L_{dB} = L_0 + n_L(d - d_0), \tag{2.2}$$

which is found effective when the communication nodes are in NLOS condition.

Eq. 2.1 and Eq. 2.2 are primarily applied to describe the fixed-fixed on-body pathloss on the trunk and other individual body parts with simple shapes. The pathloss levels of links distributed on the parts with complex shapes, e.g. head and hands, are expected to receive large spatial variation. For links distributed across different body parts, radio waves will have to travel both in the air and on the body. Although these particular link geometries can be covered by specific scenarios, pathloss in realistic on-body links are usually less dependent on the propagation distances. In practice, the on-body pathloss is also characterized by its average value and the distribution of its spatial variation in a specific scenario, as studied in [DO09].

2.3.2 Accounting for the impact of antennas

Radio propagation in BAN is a mutual coupling result between the antennas and the body. The body coupling effects change the input impedance, the current distribution, and the radiation gain of on-body antennas. Consequently, the design of on-body antennas should ideally consider the presence of the human body [IXTS09, YK06, KC10] instead of designing the antennas in free-space.

In reverse, the antennas have three significant impacts to the on-body channels. First, on-body antenna return-loss is sensitive to the change of the antenna-skin distance, which will change the input power levels of on-body channels. Second, the radiation pattern of on-body antenna will be modified in off-body communications, which will be superimposed to the radio channels. Third, the antenna polarization-mismatch is expected in static body due to antenna displacements, and in dynamic body due to the body motions, as demonstrated in [YH10].

In practical on-body channel scenarios, the antenna impacts show stochastic behaviors and are deeply mixed with the channels. Separating the antenna impacts from the channel measurements is difficult, thus most BAN measurements consider the antenna impacts as a part of the channels. The drawback of this consideration is that the measurement results are usually antenna dependent and incompatible to other antenna systems. Therefore, characterizing the antenna impacts helps to better estimate the physical channels.

CHAPTER 3
Canonical channel characterization

In this chapter, we present statistical models extracted from canonical on-body channel measurements. The goal of canonical measurements is to investigate the spatial dependence of on-body channel statistics under specific body motions. To have an explicit geometric description of the channel statistics, simple on-body scenarios are defined. The scenarios contain a single and regular body motion mode, explicit channel polarizations, and simple link geometries that are measurable with finite parameters. Statistical characterization and modeling are then made on the pathloss, temporal fading, Doppler spectrum, and the spatial channel correlation

3.1 General context

The on-body measurements were conducted in anechoic environments, hence off-body scattering is ignored. In the measurements, we placed compact and linearly polarized antennas on the front trunk of a male subject, as shown in Fig. 3.1(a). The antennas were fixed on the trunk without significant displacements during each measurement. We then assume that the properties of the antennas remain invariant in the measurements and have trivial impacts to the channel temporal variation.

On-body propagation occurring on the trunk surface are mainly affected by the scattering from the trunk and the arms. The propagation distance is then measured on the trunk surface. The positions of the nodes can be described by their relative positions to the trunk center, i.e. the navel, as depicted in Fig. 3.1(a). The link geometry of a channel distributed along a single direction, e.g. horizontal or vertical direction on the trunk, is described by the position of the Transmitter (Tx), denoted as d_{y0}, and the propagation distance, denoted as d_{xy}, where x and y stand for the index of the Receiver (Rx) and Tx.

During the measurements, the subject kept a standing posture, and swung his arms analogue to a typical walking movement, as depicted in Fig. 3.1(b). The arm swing is a small-scale, regular, and quasi-

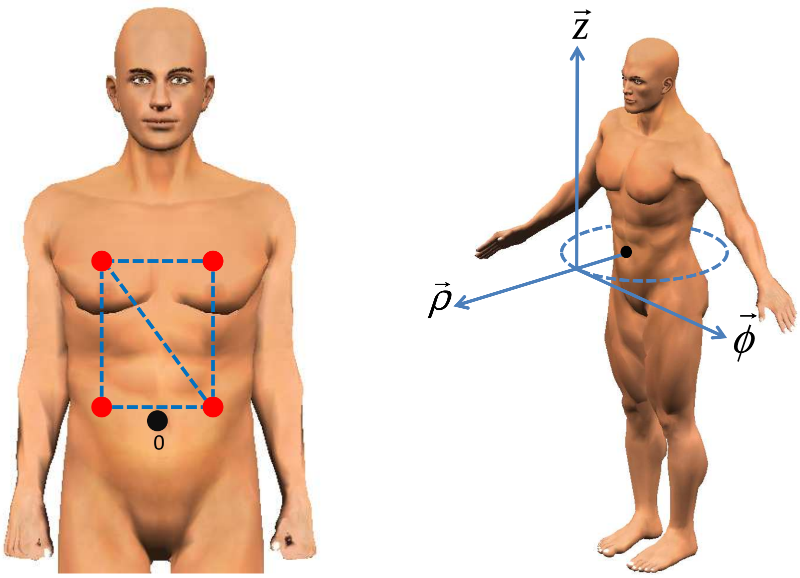

(a) (b)

Figure 3.1: General description of link geometry, body shape, body posture, and body motions in canonical on-body channel measurements. (a) Link geometries of on-body channels on the front trunk. The light points represent the possible positions of the antennas. The dash lines represent the channels. The dark point, denoted as 0, represents the trunk center to determine the relative positions of the antennas. (b) Body motion mode and coordinate system.

periodic motion mode. A typical cycle of the arm swing is around 1 s. We excluded other active body motions, therefore the arm swing consituted the principle dynamic body scattering in the measurements. Naturally, the measured channels belong to fixed-fixed on-body channels as described in Chapter 2.

Considering the link geometry and the single body motion, a simple body geometry is applied by a few parameters to describe the sizes and the positions of the trunk and the arms: perimeter of the arms, denoted as d_{arm}, perimeter of the trunk, denoted as d_{body}), and space between the arms and the trunk to determine their relative positions, denoted as d_{ab}.

We define a z-polar coordinate system to describe the direction on the trunk, as shown in Fig. 3.1(b). The direction $\vec{z}$ represents the vertical direction tangential to the skin; the direction $\vec{\phi}$ represents the horizontal direction tangential to the skin; the direction $\vec{\rho}$ represents the direction normal to the skin. This coordinate system can fully describe the direction of the link geometries and channel polarizations.

Narrowband channel measurements were made at 2.45 GHz in the temporal domain. The duration of each measurement is 10 seconds or 20 seconds to cover several cycles of the arm swing. The channels were measured through Vector Network Analyzers (VNAs) by the transmission S-parameters between the antennas. We then denoted the on-body channels as S_{xy}. The antennas were connected to the VNAs through stable coaxial cables. The current influence from the cables was found negligible to the measurements.

The measurements cover two channel polarizations: tangential and normal polarization to the trunk. Both polarizations were investigated in two sets of measurements that differ in test-beds, environments, and subjects. The measurements share common settings on link geometries, body motions, antenna emplacements, and VNA configurations, to guarantee the consistency between different measurements.

3.2 Canonical scenario description

3.2.1 Tangentially polarized scenarios

The tangentially polarized on-body channels are channels with both Tx and Rx in tangential polarization to the skin and along the $\vec{z}$ direction of the trunk. We denote this polarization as the $\vec{z}$ polarization. The $\vec{z}$-polarized channel measurements were conducted in the high-voltage laboratory of ULB. The environment was considered as quasi-anechoic since the surrounding objects were far away from the subject. Scattering from the surround objects was then ignored. Furthermore, the ground reflection had trivial influence to the channels considering the height of the antennas.

3.2.1.1 Test-bed

A four-port R&S ZVA VNA was used. The VNA has a dynamic range of 110 dB and can simultaneously measure the S-parameters between any two ports. By the reciprocity theorem [R.02], channels S_{xy} and S_{yx} in one measurement describe the same on-body propagation. Therefore we only investigated one of them. Table 3.1 summarizes the VNA settings.

Input power	0 dBm
Sweep mode	Continuous Wave (CW)
Frequency	2.45 GHz
Sampling rate	1 ms
IF bandwidth	10 KHz
Measurement length	20 s

Table 3.1: VNA settings in $\vec{z}$-polarized scenarios

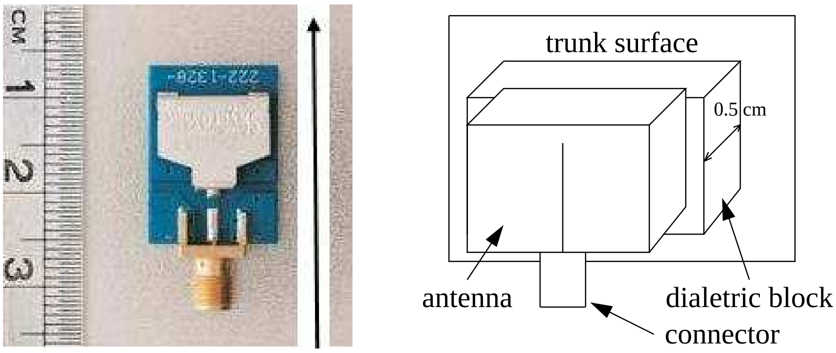

(a) (b)

Figure 3.2: Skycross antennas used in $\vec{z}$-polarized scenarios. (a) Antenna structure. The arrow points the direction of the antenna polarization. (b) Antenna emplacement on the trunk surface, with a fixed distance to the skin dielectric blocks

The Skycross SMT-3TO10M antennas were used, as shown in Fig. 3.2(a). The antennas are linearly polarized along the direction described in the figure. The Skycross antennas are originally designed to work in UWB in free-space. At 2.45 GHz, the antenna return-loss, i.e. the S_{11}, is -6 dB in free-space. When the antennas are tangentially attached to the skin, the body coupling effects will significantly change the antenna return-loss. This change is sensitive to the antenna-skin distance. We found that when the antenna-skin distance is between 0.5 and 1 cm, the antenna return-loss wil become sufficiently small, varying between -8 dB and -11 dB. In the measurements, we used dielectric blocks to fix the antenna-skin distance at 0.5 cm, as shown in Fig. 3.2(b). Thanks to the large dynamic range of the VNA and the improvement of the antenna return-loss, the reliability of the measurements was guaranteed.

3.2.1.2 Body and link geometries

Table 3.2 presents the essential geometry and other information of the subject in $\vec{z}$-polarized scenarios.

Height/Weight	183 cm/78 kg
Arm perimeter	26.3 cm
Trunk perimeter	91 cm
Arm-Trunk space	3 cm
Leg length	≥115 cm

Table 3.2: Body geometry and other information of the subject in $\vec{z}$-polarized scenarios

There are two different link geometries investigated in the $\vec{z}$-polarizted measurements.

1, Horizontal links ($\vec{z} - H$ scenario)

Fig. 3.3(a) describes the horizontal links in $\vec{z}$ polarization. Three antennas were placed at the same height to form horizontal on-body transmissions around the trunk. In this scenario, the geometry of a channel is fully described by the relative position of its Tx and its propagation distance. The quantization of the link geometry is given in Fig. 3.3(b). To control the scenario complexity, only three channels are investigated, S_{21}, S_{31} and S_{32}. The canonical measurements were made as follows: distance d_{12} was fixed at 12 cm and 14 cm to form the propagation distance of S_{21}; position of antenna 1, d_{10}, changed to form different channel positions; distance d_{23} changed to form different propagation distances of S_{31} and S_{32}. By default, in this scenario the radio waves propagate from the left side to the right side of the trunk.

2, Vertical links ($\vec{z} - V$ scenario)

The measurements of vertical links in $\vec{z}$ polarization were made as a supplementary investigation of various link geometries. Fig. 3.4(a) describes the links geometry. Four antennas are placed on the trunk to form a rectangular geometry. Antennas 1 and 2 are at the same height of the trunk center. In this configuration, we only investigated the vertical channels S_{42} and S_{31}, and the tilted channels S_{41} and S_{32} that contain vertical propagation components. The link geometry in Fig. 3.4(a) can be described by the following parameters: the position of antenna 2 d_{20} as the position of the

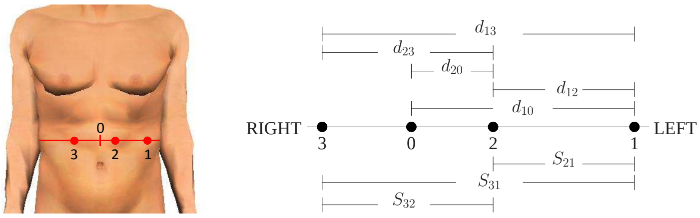

(a) Horizontal channel distribution (b) Geometric quantization of the horizontal channel distribution

Figure 3.3: Geometric description of horizontal on-body channels in $\vec{z}$-polarized scenarios. 1, 2, 3 designate the antenna positions and 0 is the trunk center

rectangle, the distances d_{12} and d_{24} as the sizes of the rectangle. Fig. 3.4(b) presents the quantization of the link geometry. The canonical measurements were made as follows: d_{24} and d_{13} were fixed at 12 cm; d_{20} changed to form different channel positions; d_{12} changed to form different vertical propagation distances.

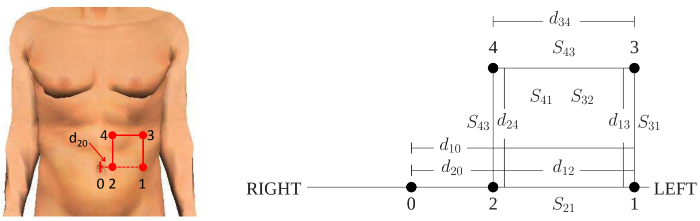

(a) Vertical channel distribution (b) Geometric quantization of the vertical channels

Figure 3.4: Geometric description of vertical on-body channels in $\vec{z}$-polarized scenarios. 1, 2, 3, 4 designate the antenna positions and 0 is the trunk center

3.2.2 Normally polarized scenarios

The normally polarized on-body channels are channels with both Tx and Rx in normal polarization to the skin, i.e. along the $\vec{\rho}$ direction in Fig. 3.1(b). We denote this polarization also as $\vec{\rho}$ polarization. The $\vec{\rho}$-polarized channel measurements were conducted in an anechoic chamber in the WELCOME laboratory, UCL. Hence, the interference from the off-body environment was excluded, and the on-body channels were only impacted by the body scattering.

3.2.2.1 Test-bed

A four-port Agilent N5242A VNA was used to measure the S-parameters of the antennas. It has a system dynamic range of 132 dB and receiver dynamic range of 130 dB. This VNA simultaneously measures S-parameters sharing the same Tx port. We then conducted the measurements with port 1 as the Tx and the remaining ports as the Rxs. Table 3.3 gives the details of the VNA settings.

Input power	5 dBm
Sweep mode	CW
Frequency	2.45 GHz
Sampling rate	1 ms
IF bandwidth	10 KHz
Measurement length	10 s

Table 3.3: VNA settings in $\vec{\rho}$-polarized scenarios

An innovative type of folded dipole antennas were designed for the $\vec{\rho}$-polarized scenarios. The folded dipole antennas maintain a linear polarization despite their compact size, as shown in Fig. 3.5(a). The antennas are designed to work in the 2.4 GHz band and are optimized when the antennas are placed on the skin in normal orientation. Fig. 3.5(b) presents the S_{11} of a folded dipole antenna when it is placed on the skin in normal polarization. It shows that the antenna return-loss is much lower than -10 dB at 2.4 GHz band, i.e. less than 10% energy is reflected back by the antenna. The lowest value of S_{11} is found at 2.45 GHz, which satisfies the needs in our measurements.

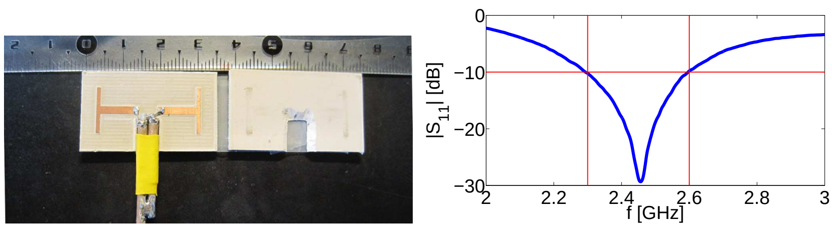

(a) Structure and packaging of a folded dipole antenna

(b) Antenna return loss (S_{11}) measured at trunk surface

Figure 3.5: Structure and performance of folded dipole antennas in $\vec{\rho}$-polarized scenarios

In the measurements, the antennas were fixed by foam blocks to keep the normal orientation, as shown in Fig. 3.6.

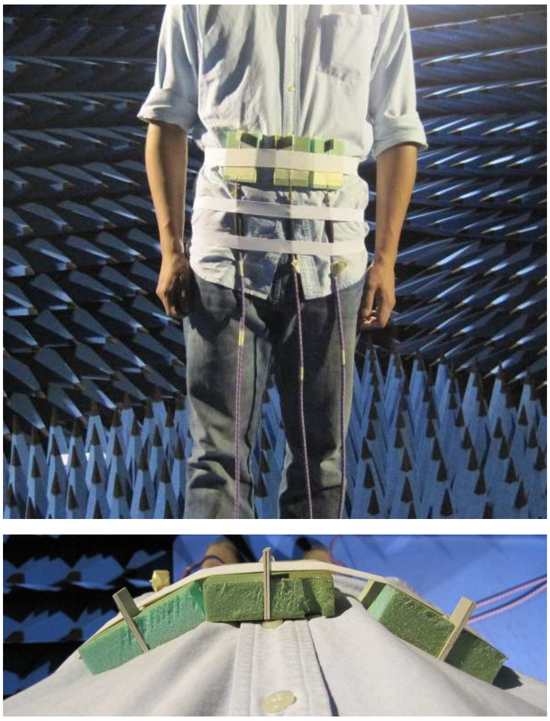

Figure 3.6: Position and polarization of the folded dipole antennas on the trunk in $\vec{\rho}$-polarized scenarios. The antennas were fixed by green foam blocks.

3.2.2.2 Body and link geometry

Table 3.4 provides the geometric parameters of the body in $\vec{\rho}$-polarized scenarios.

There are also two different link geometries investigated in the $\vec{\rho}$-polarized scenarios.

Horizontal links ($\vec{\rho} - H$ scenario)

Fig. 3.7(a) describes the horizontal link geometry in $\vec{\rho}$-polarized scenario. This geometry is analogue to $\vec{z} - H$ scenario by putting three antennas on a horizontal plane on the front trunk. The difference is that in Fig. 3.7(a) the channels propagate from the right side to the left side of the trunk. Therefore a similar quantization

Height/Weight	183 cm/75 kg
Arm perimeter	28 cm
Trunk perimeter	89 cm
Arm-Trunk space	3 cm
Leg length	≥110 cm

Table 3.4: Body geometry and other information of the subject in $\vec{\rho}$-polarized scenarios

of the link geometry is made in Fig. 3.7(b). The canonical measurements were made as follows: distance d_{12} was fixed at 12 cm and 14 cm to form the propagation distance of S_{21}; d_{10} changed to form different channel positions; d_{23} changed to form different propagation distances of S_{31} and S_{32}.

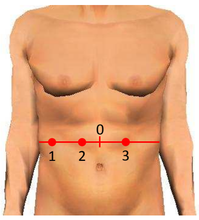

(a) Horizontal channel distribution

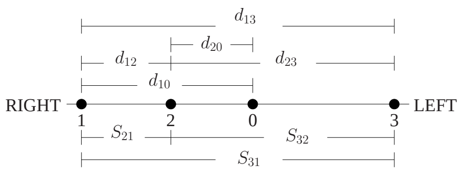

(b) Geometric quantization

Figure 3.7: Geometric description of horizontal on-body channels in $\vec{\rho}$-polarized scenarios. 1, 2, 3 designate the antenna allocations and 0 is the trunk center

Vertical links ($\vec{\rho} - V$ scenario)

Fig. 3.8(a) describes the vertical link geometry in $\vec{\rho}$-polarized scenarios. Three antennas were located along the trunk in the vertical direction. The antenna 1 was at the same height of the trunk center. The positions of the channels are described by d_{10}, i.e. the horizontal distance between antenna 1 and the trunk center 0. Fig. 3.8(b) presents the quantization of the link geometry. The canonical measurements were made as follows: distance d_{12} was fixed at 7 cm and 12 cm to form the propagation distance of S_{21}; position of antenna 1, d_{10} changed to form different channel locations; distance d_{23} changed to form different propagation distances of S_{31} and S_{32}.

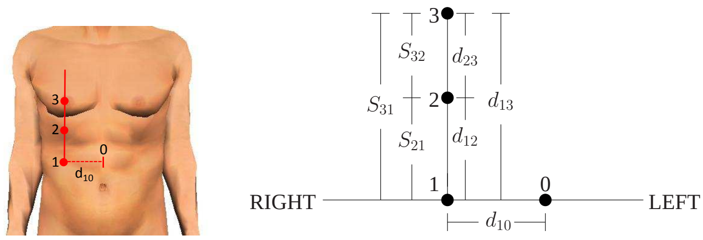

(a) Vertical channel distribution

(b) Geometric quantization

Figure 3.8: Geometric description of on-body vertical channels in $\vec{\rho}$-ploarized scenarios. 1, 2, 3 designate the antenna allocations and 0 is the trunk center

3.2.3 Summary of canonical scenarios

Table 3.5 summarizes the scenarios in the canonical on-body measurements, and the geometric identification of the measurements in each scenario.

Scenarios	Notation	Geometric identification
$\vec{z}$-polarized, horizontal links	$\vec{z} - H$	$d_{12} - d_{10} - d_{23}$
$\vec{z}$-polarized, vertical links	$\vec{z} - V$	$d_{20} - d_{12} - d_{24}$
$\vec{\rho}$-polarized, horizontal links	$\vec{\rho} - H$	$d_{12} - d_{10} - d_{23}$
$\vec{\rho}$-polarized, vertical links	$\vec{\rho} - V$	$d_{12} - d_{10} - d_{23}$

Table 3.5: Summary of canonical on-body scenarios

3.3 Statistical characterization and modeling

3.3.1 Channel estimation

We did not apply additional estimations to extract the channels from the measurements based on several facts: 1) the narrowband on-body channels were directly measured through the S-parameters; 2) the measurements were made in anechoic environment without off-body interference to be canceled; 3) the antennas were firmly fixed without significant dynamic impact to the measurements. Consequently, the measured S-parameters were treated as the direct complex channel measurements. In $\vec{z}-H$ and $\vec{z}-V$ scenarios, we applied a moving average by a rectangle window of 50 ms to suppress the noise in the measurements as:

$$\bar{S}_{xy}(n) = \frac{1}{N} \sum_{m=n-N/2}^{n+N/2} S_{xy}(m) \quad N = 50. \tag{3.1}$$

The channel fading is the channel variation observed in various domains. We define both temporal fading and spatial fading of narrowband on-body channels. The temporal fading is the time-variation of the channels under the dynamic body scattering in a single measurement. The spatial fading is the variation of the channel statistics observed in multiple measurements, also referred as the spatial variation. However, the conventional definitions of slow fading (shadowing) and fast fading in large-scale propagation are not applicable for on-body channels. This is because the limited scattering components resulting from the body are insufficient to cause significant multipath effects. Therefore the fading on the temporal domain is a single description of the time-variation of the channels.

The statistics of the on-body channels are characterized per measurement lasting for 20 seconds in $\vec{z}$-polarized scenarios and 10 seconds in $\vec{\rho}$-polarized scenarios. The statistical results are collected and related to the link geometries to enable canonical spatial descriptions.

3.3.2 Pathloss

The narrowband on-body pathloss is the inverse of the average of the channel amplitudes in temporal domain, which is calculated in dB:

$$L_{dB} = -\mathrm{E}[|S|_{\mathrm{dB}}(t)] \tag{3.2}$$

where $\mathrm{E}[\bullet]$ is the expectation operator applied in the temporal domain.

Fig. 3.9 presents the on-body pathloss in different scenarios. The results in $\vec{z} - V$ scenario cover only the vertical channels S_{43} and S_{31}. In the figures, each point represents a single measurement of an on-body channel given specific position and propagation distance. Such notation is used throughout this chapter.

The results are related to the propagation distances of the considered channels. We observe high pathloss levels within short propagation distances. The pathloss levels show quasi-linear increase along with the increase of the propagation distance in all the scenarios. Linear models are applied to describe the average increasing rates of the pathloss levels, which is also plotted in the figures.

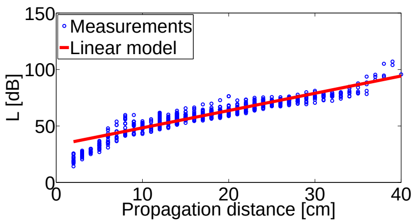

(a) $\vec{z}-H$ scenario

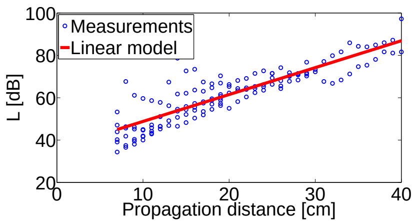

(b) $\vec{z}-V$ scenario

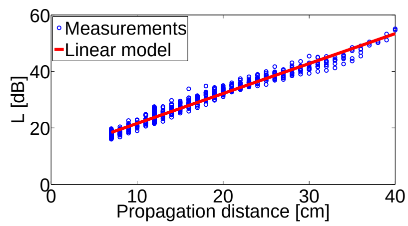

(c) $\vec{\rho}-H$ scenario

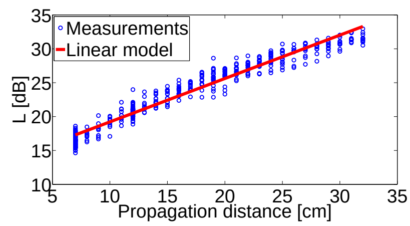

(d) $\vec{\rho}-V$ scenario

Figure 3.9: On-body pathloss in dB in different scenarios

Spatial variation of the pathloss is observed in Fig. 3.9, which is the fluctuation of the pathloss levels around their local means at a certain propagation distance. Such variation is brought by measuring the channels at different positions. The variation levels are stable at different propagation distances. Therefore we model the overall spatial variation of the pathloss by a zero-mean normal distribution, which matches the measurements well as shown in Fig. 3.10. The spatial variation of the pathloss is then characterized by its Standard Deviation (STD), denoted as σ_L.

We then propose an empirical model to describe both the linear increasing rate and and the spatial variation of the on-body pathloss in our measurements:

$$\begin{aligned} L(d)_{\mathrm{dB}} &= \mu_L(d) + \sigma_L W \\ \mu_L(d) &= L_0 + n_L(d - d_0), \end{aligned} \tag{3.3}$$

where μ_L is the linear model of the average pathloss increasing rate described by n_L, d is the propagation distance on the trunk, L_0 and d_0 are the reference pathloss level and propagation distance, σ_L is the STD of the pathloss spatial variation, $W \sim \mathcal{N}(0,1)$ is a random variable following a normal distribution. All the distances in Eq. 3.3 are measured in centimeters. The estimation by the model in each scenario is presented

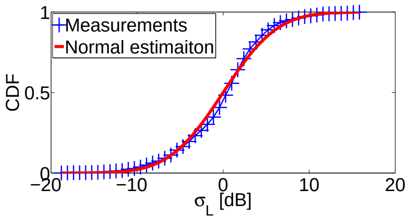

(a) $\vec{z} - H$ scenario

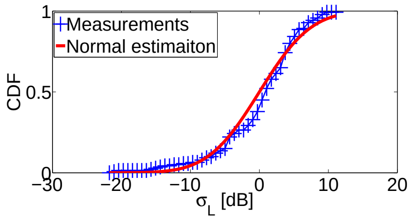

(b) $\vec{z} - V$ scenario

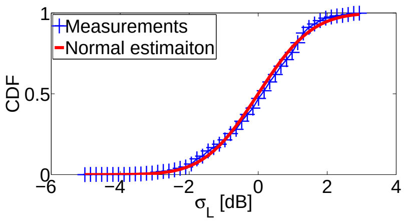

(c) $\vec{\rho} - H$ scenario

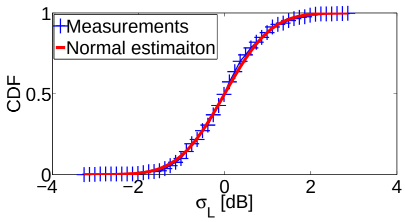

(d) $\vec{\rho} - V$ scenario

Figure 3.10: Distribution of on-body pathloss spatial variation in dB

as follows:

1. For $\vec{z} - H$ links:

$$L_{\text{dB}} = 36.1 + 1.53(d - 2) + 3.25W \tag{3.4}$$

2. For $\vec{z} - V$ links:

$$L_{\text{dB}} = 45 + 1.27(d - 7) + 5.99W \tag{3.5}$$

3. For $\vec{\rho} - H$ links:

$$L_{\text{dB}} = 18.4 + 1.06(d - 7) + 1.21W \tag{3.6}$$

4. For $\vec{\rho} - V$ links:

$$L_{\text{dB}} = 17.3 + 0.64(d - 7) + 0.89W \tag{3.7}$$

The comparison on the pathloss increasing rates brings two conclusions. First, the pathloss levels in $\vec{\rho}$-polarized scenarios are much lower than in $\vec{z}$-polarized scenarios. The better link quality in normal polarization can be explained by several reasons: 1) the normally polarized antennas are closer to LOS conditions, therefore they are less shadowed by the body; 2) the body scattering influence is also smaller to the normally polarized antennas; 3) creeping waves are formed are formed on the trunk for normal polarization [KC10], which helps to alleviate the body shadowing effect. Second, in both polarizations, vertical channels along the trunk have lower pathloss increasing rate than horizontal channels around the trunk. Such difference is because horizontal propagation around the cylindrical trunk is closer to NLOS condition and receives larger shadowing from the body than the vertical propagation.

The results also show that the pathloss spatial variation in the $\vec{\rho}$-polarized scenarios are lower than in the $\vec{z}$-polarized scenarios. First, this is because the LOS propagation condition in the $\vec{\rho}$-polarized scenarios alleviates the influence of body scattering variety to the pathloss levels in different positions. Second, this is also because antennas in normal orientation are less sensitive to the antenna displacement than the antennas tangentially attached to the skin, which further weakens the pathloss spatial variation in the measurements.

3.3.3 Temporal fading

Temporal fading describes the time-variation of each individual channel. We estimated the Cumulative Density Function (CDF) and Probability Density Function (PDF) of the temporal fading amplitudes on linear scale in each measurement, i.e. $|S_{xy}|_{\text{lin}}$. Different distribution models are investigated to estimate the fading distribution by Maximum Likelihood Estimator (MLE) [Ibe05], including the Lognormal, Normal, Exponential, Weibull, Gamma, Nakagami, Rayleigh, and Rice distribution models. The estimation results are evaluated through the Mean Square Error (MSE) as:

$$\text{MSE} = E[(x_n - \hat{x}_n)^2], \tag{3.8}$$

where x_n and $\hat{x}_n$ correspond to the observed and estimated PDF of the random variables, n is the index of the intervals.

To make a fair comparison, we estimated the fading distribution of the normalized channels, i.e. the fading amplitudes are normalized so that the average energy is one. Fig. 3.11 compares the average MSE of the estimation results in each scenario. The comparison shows close and good estimation performances of the Lognormal, Nakagami, and Gamma distribution models in $\vec{z} - H$, $\vec{\rho} - H$ and $\vec{\rho} - V$ scenarios.

Fig. 3.12 presents the Lognormal estimation of the average fading distribution, which fits well the measurements. A χ^2 goodness-of-fit test

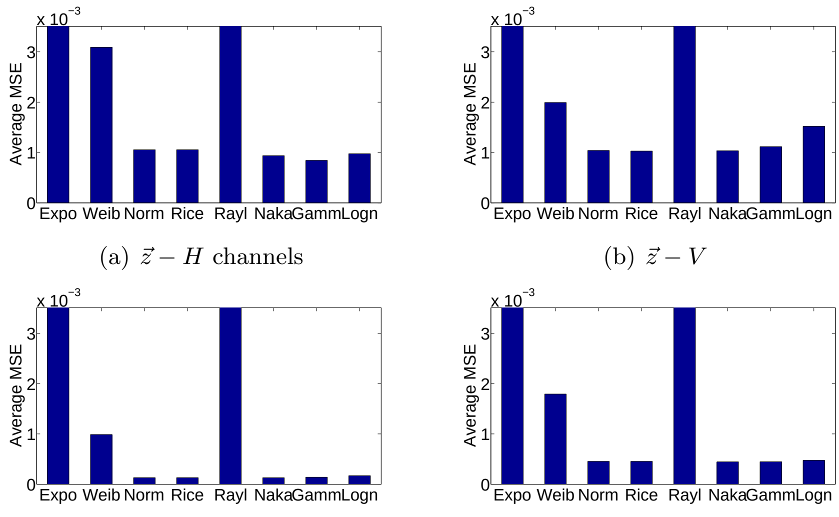

(a) $\vec{z} - H$ channels (b) $\vec{z} - V$

(c) $\vec{\rho} - H$ channels (d) $\vec{\rho} - V$ channels

Figure 3.11: Average MSE of estimation results of fading amplitude distribution on linear scale in canonical measurements

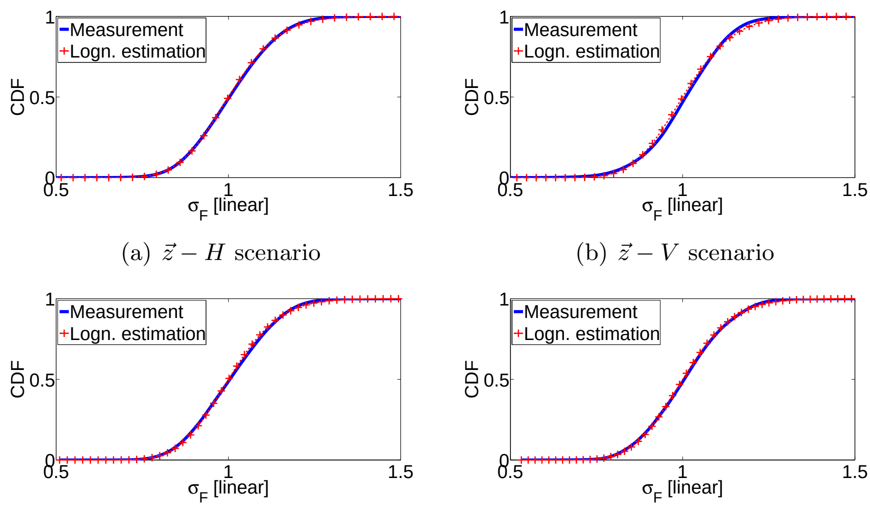

(a) $\vec{z} - H$ scenario (b) $\vec{z} - V$ scenario

(c) $\vec{\rho} - H$ scenario (d) $\vec{\rho} - V$ scenario

Figure 3.12: Lognormal estimation of the average fading amplitude on linear scale

has also successfully confirmed the adequacy of the Lognormal distribution. We then adopt the Lognormal model to describe the temporal fading distribution based on its estimation performance and simple representation, i.e. normal distribution in dB. Hence, the temporal fading is characterized by its STD in dB as:

$$\sigma_F = \mathrm{E}[\sqrt{(|S|_{\mathrm{dB}} - \mathrm{E}[|S|_{\mathrm{dB}}])^2}], \tag{3.9}$$

Fig. 3.13 presents the results of σ_F in each scenario, which are also related to the propagation distance of the considered channels. Similarly to the pathloss L results in Sec. 3.3.2, σ_F shows quasi-linear increase along with the increase of the propagation distance and spatial variation in all the scenarios. The spatial variation of σ_F is caused by two reasons: the different locations of the channels, and the motion variation of the arm swing in different measurements.

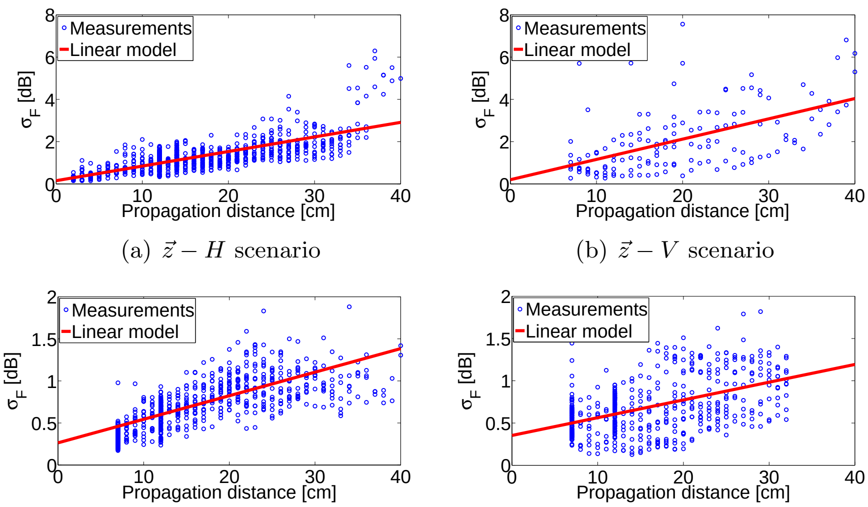

(a) $\vec{z} - H$ scenario

(b) $\vec{z} - V$ scenario

(c) $\vec{\rho} - H$ scenario

(d) $\vec{\rho} - V$ scenario

Figure 3.13: Temporal fading STD in dB in different scenarios

Therefore, as analogue to Eq. 3.3, we propose an empirical model to describe the linear increasing rate and spatial variation of σ_F in dB as:

$$\begin{aligned} \sigma_F &= \mu_{\sigma_F} + \sigma_{\sigma_F} W \\ \mu_{\sigma_F} &= \sigma_{F0} + n_{\sigma_F}(d - d_0) \end{aligned} \tag{3.10}$$

where d is also measured in centimeters. The estimation results of μ_{σ_F} match the increasing rates in measurements as shown in Fig. 3.13. Table 3.6 summarizes the parameter estimation of the model in each scenario.

Scenarios	σ_{F0}	d_0	n_{σ_F}	σ_{σ_F}
$\vec{z} - H$	0.29	2	0.069	0.51
$\vec{z} - V$	0.87	7	0.096	1.3
$\vec{\rho} - H$	0.46	7	0.028	0.3
$\vec{\rho} - V$	0.5	7	0.021	0.32

Table 3.6: Statistical summaries of the temporal fading in canonical on-body channel measurements

Results in Table 3.6 show higher increasing rates of σ_F in $\vec{z}$-polarized scenarios than in $\vec{\rho}$-polarized scenarios. This is because $\vec{z}$-polarized on-body channels receive larger attenuation than the $\vec{\rho}$-polarized channels, therefore the dynamic interference from the arms is relatively amplified to the $\vec{z}$-polarized channels.

The increasing rates of σ_F are close between horizontal and vertical links in $\vec{\rho}$-polarized scenarios. It means that the normally polarized antennas are insensitive to the dynamic arm scattering, which thereby causes close dynamic scattering interference in both directions.

The results also show smaller spatial variation of σ_F in $\vec{\rho}$-polarized scenarios than in $\vec{z}$-polarized scenarios. First, it is because the lower pathloss levels in $\vec{\rho}$-polarized scenarios mitigate the variation from the dynamic arm scattering. Second, it is also because the normally polarized antennas are less sensitive to the arm scattering.

3.3.4 Doppler spectrum

The Doppler spectrum of a propagation channel models the mobility of Tx, Rx, or the surrounding scatterers. In the canonical measurements, we measured fixed-fixed on-body channels. The swinging arms then become the local moving scatterers that form the Doppler spectra of the on-body channels. We estimated the Doppler Power Spectrum Density (PSD) in the measurements by the periodogram method.

Body motions like walk and arm swing are typically local and repetitive movements. It means that in a certain posture, the dynamic body scattering will show temporal variation around an average value. Consequently, the Doppler spectrum of an on-body channel will be centered at 0 Hz Doppler frequency shift and has certain spread corresponding to the motions. The arm swing is a periodic motion. Therefore the scattering from the swinging arms will also contain strong periodic components that bring periodic temporal fading of the on-body channels.

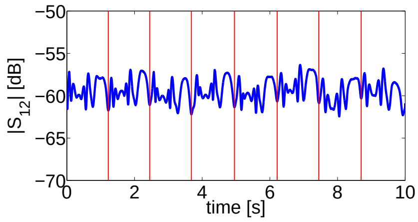

(a) Channel amplitude, red lines divide the cycles

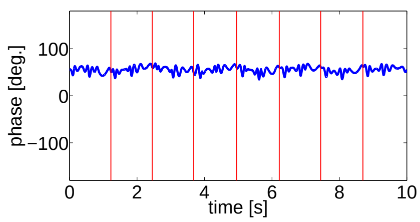

(b) Channel phase, red lines divide the cycles

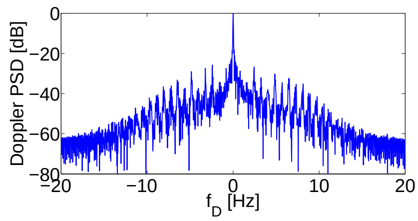

(c) Doppler PSD of complex channel

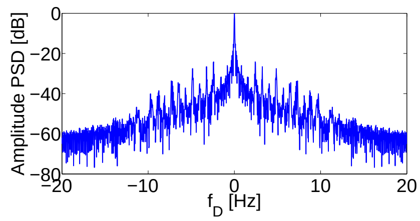

(d) PSD of channel amplitude

Figure 3.14: An example of a periodic on-body channel and its Doppler PSD, selected from S_{21} in a $\vec{z}-H$ measurement identified by $d_{12}-d_{10}-d_{23} = 14-19-23$ [cm]

An example of periodic on-body channel is shown in Fig. 3.14. A measurement sample of channel S_{21} is selected from a measurement in $\vec{z}-H$ scenario, identified by $d_{12}-d_{10}-d_{23} = 14-19-23$ [cm]. Both the amplitude and phase of the channel show cycles as marked in Fig. 3.14(a) and Fig. 3.14(b). The cycle of the channel's time-variation corresponds to the cycle of the arm swing, which is around 1.2 seconds. We further observe periodic and symmetric patterns of the channel in the first half and second half of one cycle, which is consistent with the regular forward-and-backward pattern of the arm swing. The phase of the channel varies in a smaller range ($< 30°$) in Fig. 3.14(b) compared to the range of the arm swing (> 20 cm). It means that the interference from the dynamic arm scattering is much smaller than the trunk scattering to the channel, where the latter determines the pathloss level.

Fig. 3.14(c) presents the Doppler PSD of the channel taken as an example. The strong peaks at the frequency harmonics in the spectrum correspond to the cycles of the channel. Because the phase of the channel has small variation, the spectrum spread of the channel amplitude in Fig. 3.14(d) is close to the Doppler spread of the channel.

Fig. 3.15 presents the average normalized Doppler PSD in each scenario. The normalization of the Doppler PSD is made by normalizing the channel gains to 0 dB. The averaging on the normalized Doppler PSD covers all the measured channels in one scenario. The results show that in all the scenarios, the Doppler spread is concentrated within 10 Hz, which is consistent with the slow body motions. In all the scenarios, peaks are found in the Doppler PSDs at fundamental frequencies around 1 Hz and the harmonics, which correspond to the cycle of the arm swing. Because of a larger temporal fading in $\vec{z}$-polarized scenarios, the PSD distributions at the frequency harmonics in $\vec{z}$-polarized scenarios are larger than in $\vec{\rho}$-polarized scenarios.

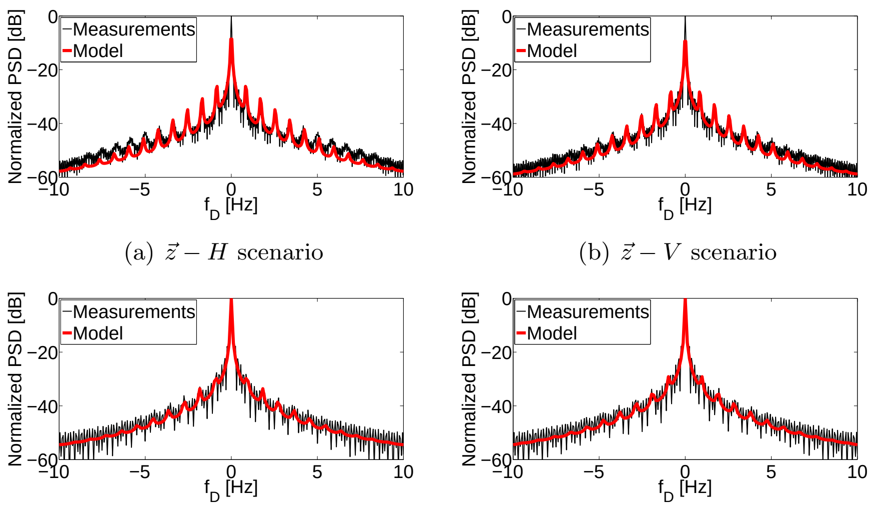

(a) $\vec{z} - H$ scenario (b) $\vec{z} - V$ scenario

(c) $\vec{\rho} - H$ scenario (d) $\vec{\rho} - V$ scenario

Figure 3.15: Doppler PSD and empirical model estimation in different scenarios

An experimental model of the Doppler spread is proposed in [ANP$^+$09] by assuming uniform moving scattering environment, expressed as:

$$\mathrm{PSD}(f_D) = \frac{1}{s_D + f_D^2}, \tag{3.11}$$

where f_D is the Doppler frequency, and s_D is the spread parameter which is inversely proportional to the Doppler spread. This model is found to well fit the Doppler PSDs of on-body channels measured in an indoor environment as in [DO11]. For the scenarios under periodic arm swing, we modify Eq. 3.11 to fit both the overall spectrum spread and the local spectrum spreads at the frequency harmonics, expressed as:

$$\mathrm{PSD}(f_D) = \sum_{m=0}^{\infty} \frac{1}{1 + ma_D + s_D(f_D - mf_0)^2} \frac{1}{x_D 2^m}, \tag{3.12}$$

where f_0 is the fundamental frequency, s_D describes the overall Doppler PSD spread, a_D describes the extra local spectrum spread the frequency harmonics, x_D is a the decaying of the Doppler PSD at the fundamental frequency compared with $f_D = 0$ Hz, and 2^m is an extra fitting of the spectrum decrease between adjacent frequency harmonics. The parameters a_D, s_D, and x_D describe three independent properties of the Doppler PSDs of periodic on-body channels. They are then estimated sequentially. Fig. 3.15 also presents the estimation results, which match the measurements well. In Table 3.7, the parameter estimations of the model in each scenario are summarized.

scenario	f_0 [Hz]	s_D [W^{-1}Hz^{-2}]	x_D	a_D
$\vec{z} - H$	0.85	6740	23	5.4
$\vec{z} - V$	0.85	8340	29	7.5
$\vec{\rho} - H$	0.91	3030	51	7.2
$\vec{\rho} - V$	0.95	2950	56	8.3

Table 3.7: Model estimation of the Doppler PSD in each scenario by Eq. 3.12

3.3.5 Spatial channel correlation

The spatial channel correlation, or inter-channel correlation, is usually explained by the scattering commonness in large-scale propagation. Studies on shadowing correlation in large-scale propagation use mobile networks use geometry-based approaches to describe such common scattering effect, like models in [WTN06, Sør99, AP09, Gud91]. In these models, the distance or angle difference is an important parameter to describe the shadowing cross-correlation.

The canonical on-body channels have shown strong spatial dependence on their statistics. Fixed-fixed on-body channels distributed in a small area are expected to receive geometry-dependent body scattering interferences that bring common scattering effect to the channels. Therefore, we also resort to geometry-based investigations and the geometry difference to characterize and model the spatial on-body channel correlation.

By the conclusion that on-body channel fading follows Lognormal distribution as in Sec. 3.3.3, the correlation coefficient between two on-body channels is defined as:

$$\rho_{1,2} = \frac{\mathrm{E}[(|S_1|_{dB} - \mathrm{E}[|S_2|_{dB}])(|S_2|_{dB} - \mathrm{E}[|S_2|_{dB}])]}{\sigma_{|S_1|_{dB}}\sigma_{|S_2|_{dB}}} \tag{3.13}$$

Similarly to the investigations on the pathloss and temporal fading in Sec. 3.3.2 and Sec. 3.3.3, we propose an empirical model trying to cover both the average and spatial variation of $\rho_{1,2}$, as:

$$\rho_{1,2} = \mu_{\rho_{1,2}} + \sigma_{\rho_{1,2}} U, \tag{3.14}$$

where $U \sim \mathcal{N}(0,1)$ is a random variable following a truncated normal distribution, which should guarantee that $|\rho_{1,2}| \leq 1$. $\mu_{\rho_{1,2}}$ is expected to be modeled in geometric way.

3.3.5.1 $\vec{z} - H$ scenario

In the $\vec{z} - H$ scenario described in Fig. 3.3, the correlation coefficient between channels S_{21} and S_{31} is investigated. The overlapping channels share a common Tx (antenna 1) and differ in the locations of their Rxs, which is described by the distance difference between antennas 2 and 3, denoted as d_{23}.

Fig. 3.16 presents two examples of $\rho_{21,31}$ as a function of d_{23} from measurements with $d_{12} = 12$ cm and $d_{12} = 14$ cm. Decreasing trends can be observed in both examples. It means that overlapping channels in the $\vec{z} - H$ scenario will lose their correlation when their distance difference increases. This conclusion is valid when the channels are distributed on the front trunk.

The average decreasing trend of $\rho_{21,31}$, $\mu_{\rho_{21,31}}$, is then described by a linear model. A natural boundary condition should hold in the model that $\mu_{\rho_{21,31}} = 1$ when $d_{23} = 0$ cm, representing a total overlapping of S_{21} and S_{31}. Finally, $\rho_{21,31}$ in $\vec{z} - H$ scenario is modeled as:

$$\rho_{21,31}(d_{23}[\text{cm}]) = \begin{cases} 1 - 0.043 d_{23} + 0.19U & 0 \leqslant d_{23} < 23\text{cm} \\ 0 & d_{23} \geqslant 23\text{cm} \end{cases}, \tag{3.15}$$

The estimation of $\mu_{\rho_{21,31}}$ by the model well matches the average decreasing rate of the overall results, as shown in Fig. 3.17.

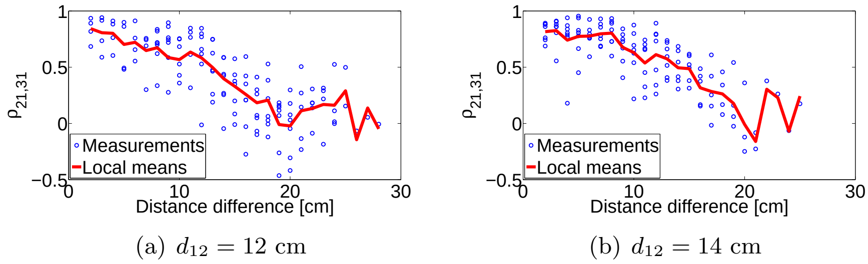

Figure 3.16: Two examples of $\rho_{21,31}$ in $\vec{z} - H$ scenario with different d_{12}

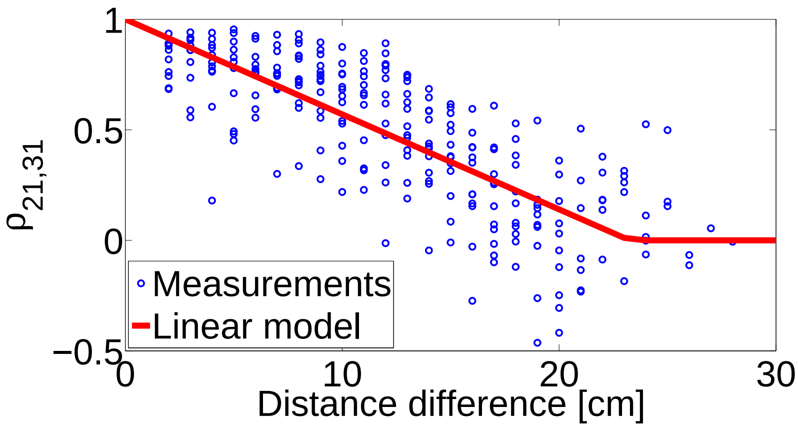

Figure 3.17: Overall results and the linear model of $\rho_{21,31}$ in $\vec{z} - H$ scenario

3.3.5.2 $\vec{z} - V$ scenario

In the $\vec{z} - V$ scenario described in Fig. 3.4, we investigate the correlation coefficient between channels S_{21} and S_{41}, denoted as $\rho_{21,41}$. The geometric difference between S_{41} and S_{21} is described by the angle as shown in Fig. 3.18, denoted as θ_{24}, $\theta_{24} = \arctan(d_{24}/d_{21})$. Fig. 3.19(a) presents the results of $\rho_{21,41}$ as a function of θ_{24}.

The results do not show any trend of $\rho_{21,41}$ when θ_{24} varies. It means that the vertical channels receive a more complicated dynamic arm scattering. In reality, both horizontal and vertical arm swing will impact the vertical channels. The arm swing also includes complex small movements like the bending of the forearm, which will also complicate the time-variation of the arm scattering. In the absence of any significant trend, $\rho_{21,41}$ is modeled as following a truncated normal distribution, as shown in Fig. 3.19(b), and is expressed as:

$$\rho_{21,41} = 0.14 + 0.35U \tag{3.16}$$

The absolute value of $\rho_{21,41}$ is characterized in Fig. 3.19(c). Fig. 3.19(d) presents a MSE comparison of the estimations by different distribution models on $|\rho_{21,41}|$, which suggests that $|\rho_{21,41}|$ follows the Beta distribution:

$$\text{PDF}(\rho) = \frac{1}{B(a_B, b_B)}(1-x)^{b_B - 1} \tag{3.17}$$

where $B(a_B, b_B)$ is the Beta function with parameters a_B and b_B. The estimation results of $|\rho_{21,41}|$ is summarized in Table 3.4.

3.3.5.3 $\vec{\rho} - H$ scenario

In the $\vec{\rho} - H$ scenario described in Fig. 3.7, we investigate the correlation coefficient between overlapping channels S_{21} and S_{31} similarly to the investigation in the $\vec{z} - H$ scenario. $\rho_{21,31}$ is then described as a function of d_{23}. Fig. 3.20(a) presents the collection of $\rho_{21,31}$. The results show a large variation of $\rho_{21,31}$ especially at small d_{23}. The overall $\rho_{21,31}$ is then modeled to follow a truncated Guassian distribution as shown in Fig. 3.20(b), expressed as:

$$\rho_{21,31} = 0.51 + 0.31U \tag{3.18}$$

Furthermore, Fig. 3.20(c) presents the distribution of $|\rho_{21,31}|$. Using similar estimation approach as in $\vec{z} - V$ scenario, the MSE comparison results shown in Fig. 3.20(d) $|\rho_{21,31}|$ suggest that $|\rho_{21,31}|$ follows a Beta distribution. The statistics of $|\rho_{21,31}|$ are summarized in Table 3.4.

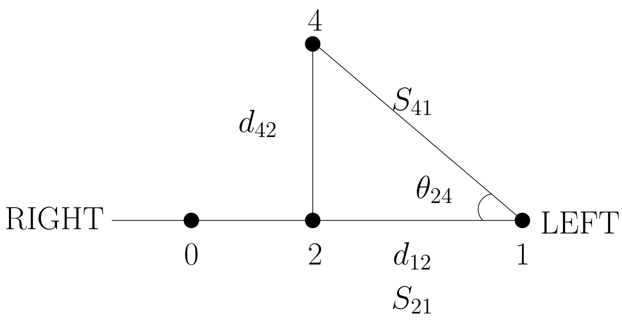

Figure 3.18: Angle difference between S_{41} and S_{21} in $\vec{z} - V$ scenario

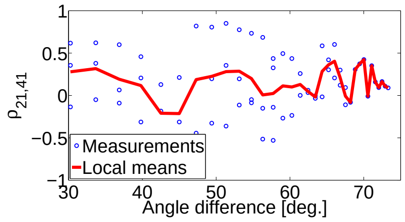

(a) $\rho_{21,41}$

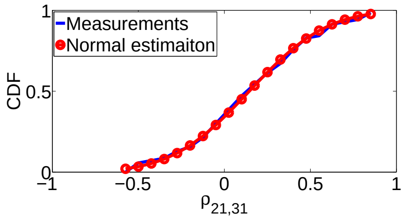

(b) Distribution of $\rho_{21,41}$

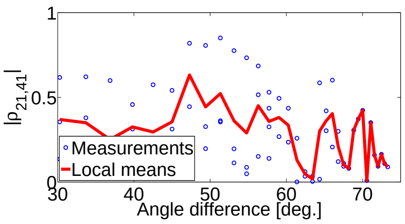

(c) $|\rho_{21,41}|$

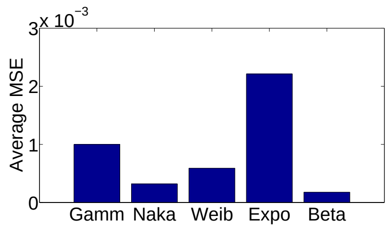

(d) MSE comparison of different distribution models of $|\rho_{21,41}|$

Figure 3.19: $\rho_{21,41}$ in $\vec{z} - V$ scenarios

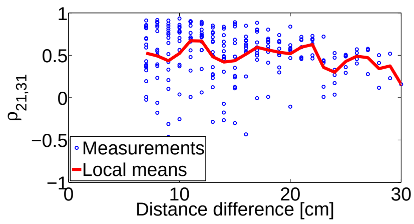

(a) $\rho_{21,31}$

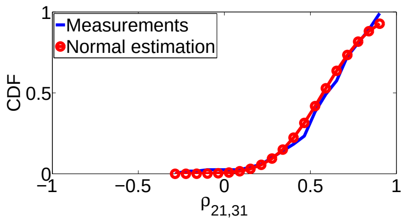

(b) Distribution of $\rho_{21,31}$

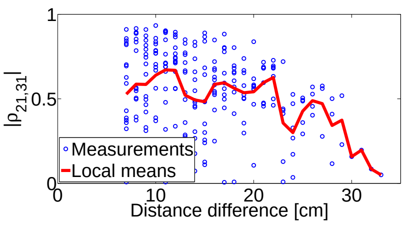

(c) $|\rho_{21,31}|$

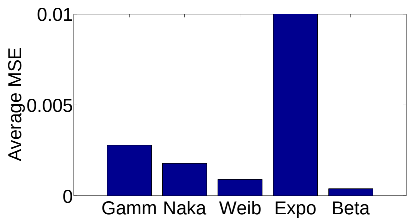

(d) MSE comparison of different distribution models of $|\rho_{21,31}|$

Figure 3.20: $\rho_{21,31}$ in $\vec{\rho} - H$ scenario

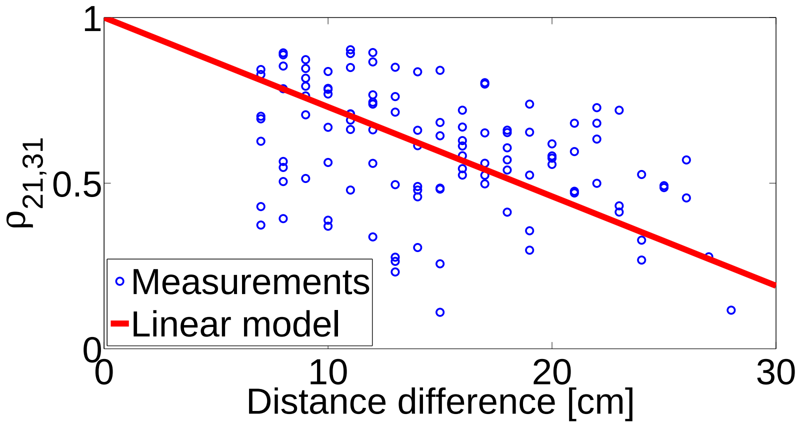

Figure 3.21: $\rho_{21,31}$ when $d_{20} > 0$ cm in $\vec{\rho} - H$ scenario

A decreasing trend of $\rho_{21,31}$ is observed when the position of antenna 2 is located on the right side of the trunk ($d_{20} > 0$), as shown in Fig. 3.21. Therefore, similarly the $\vec{z} - H$ scenario by Eq. 3.15, an empirical model is proposed to describe the average decreasing rate and spatial variation of $\rho_{21,31}$ in this condition:

$$\rho_{21,31}(d_{23}[\text{cm}]) = \begin{cases} 1 - 0.027d_{23} + 0.20U & 0 \leqslant d_{23} < 30\text{cm} \\ 0 & d_{23} \geqslant 30\text{cm} \end{cases}, \quad (3.19)$$

where the linear part of this model matches the average decreasing rate of the measurement results well as shown in Fig. 3.17.

The decreasing rate of $\rho_{21,31}$ in Eq. 3.19 is smaller than the decreasing rate of $\rho_{21,31}$ in Eq. 3.15 in $\vec{z} - H$ scenario. It means that the horizontal channels in $\vec{\rho}$ polarization receive less changes of dynamic arm scattering at different positions.

3.3.5.4 $\vec{\rho} - V$ scenario

In the $\vec{\rho} - V$ scenario described in Fig. 3.8, the correlation coefficient between overlapping channels S_{21} and S_{31} is investigated. The $\rho_{21,31}$ is still related to d_{23} as in the $\vec{z} - H$ and $\vec{\rho} - H$ scenarios. Fig. 3.22(a) presents the results of $\rho_{21,31}$ versus d_{23}. The results show a random variation of $\rho_{21,31}$ that is unrelated to d_{23}. $\rho_{21,31}$ is also modeled as following a normal distribution as in Fig. 3.22(b), which is expressed as:

$$\rho_{21,31} = -0.036 + 0.35U \quad (3.20)$$

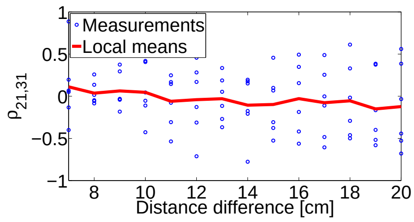

(a) $\rho_{21,31}$

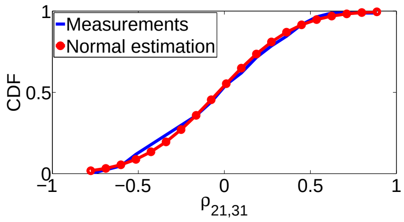

(b) Distribution of $\rho_{21,31}$

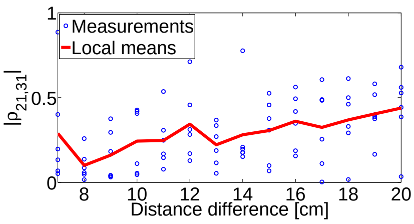

(c) $|\rho_{21,31}|$

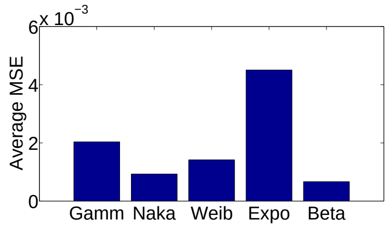

(d) MSE comparison of different distribution models of $|\rho_{21,31}|$

Figure 3.22: $\rho_{21,31}$ and $|\rho_{21,31}|$ in $\vec{\rho} - V$ scenario

Fig. 3.22(c) presents the distribution of $|\rho_{21,31}|$. By similar comparison approach, $|\rho_{21,31}|$ is modeled as following a Beta distribution, as in Fig. 3.22(d). The statistics of $\rho_{21,31}$ are summarized in Table 3.4.

3.4 Conclusion on spatial on-body channel correlation

Table 3.4 summarizes the modeling of the spatial on-body channel correlation in each scenario.

scenarios	$\rho_{1,2}$	Beta distr. of $\lvert\rho_{1,2}\rvert$
$\vec{z} - H$, $\rho_{21,31}$	$1 - 0.043d + 0.19U$	n.a.
$\vec{z} - V$, $\rho_{21,41}$	$0.14 + 0.35U$	a_B/b_B=0.94/2.15
$\vec{\rho} - H$, $\rho_{21,31}$ (overall)	$0.51 + 0.31U$	a_B/b_B=1.62/1.46
$\vec{\rho} - H$, $\rho_{21,31}$ ($d_{20} > 0$)	$1 - 0.027d + 0.20U$	n.a.
$\vec{\rho} - V$, $\rho_{21,31}$	$-0.036 + 0.35U$	a_B/b_B=1.14/2.79

Table 3.8: Statistical summaries of spatial channel correlation in canonical on-body measurements

The results show large spatial variation of the correlation coefficients in all the scenarios. In addition to the complexity of the dynamic body scattering and the varying of channel locations, the limited duration of each measurement also raises such spatial variation.

The horizontal overlapping channels in both $\vec{z}$- and $\vec{\rho}$-polarized scenarios have shown significant decreasing trends as the geometric difference, i.e. the distance differences between the channels increase. It shows a clear spatial dependence of the arm scattering along the horizontal direction. Therefore the correlations of horizontal channels are described in geometry as a function of their distance difference.

On the contrary, vertical channels in both polarization scenarios receive more complicated arm scattering in both temporal and spatial domains. The spatial dependence of the arm scattering is then weak. As a result, the correlation of vertical channels shows random distribution. The correlation coefficients are then modeled as following normal distributions, and their absolute values are modeled as following Beta distributions.

CHAPTER 4

Scenario-based channel characterization

The canonical measurements in Ch. 3 have shown a strong influence of the scenario specification to on-body channel properties. The scenarios in realistic applications are much more complicated than the simple scenarios defined in the canonical measurements. The complexity of realistic scenarios can be found in the following aspects:

1. The on-body communications will cover a large area across different body parts, which are difficult to describe with quantized geometry.
2. Various body motion modes will bring distinct dynamic body scattering effects as far as temporal channel fading is concerned.
3. On-body antennas may have significant displacements in both positions and orientations, which will increase the antenna interference to the channels.
4. Scattering from off-body environment will also impact on-body propagations.

In scenario-based on-body channel measurements, less emphasis is put on the geometric description. Instead, on-body channels are described by the concerned body parts, e.g. from head to chest. This allows the measurements to investigate on-body links in a larger area and offer a more general channel description aimed at specific but practical BAN systems.

In this chapter, we present two kinds of scenario-based dynamic narrowband on-body measurements conducted in indoor environments: dual-link measurements at 2.47 GHz and multi-link measurements at 4.2 GHz. The measurements differ by their test-beds, environments, subjects, and body motion modes. We resort to similar characterization and modeling methods as in the canonical measurements to keep a consistent study. The results provide a preliminary knowledge of the dynamic on-body channels in realistic environments.

4.1 2.47 GHz dual-link measurements

4.1.1 Measurement context

The measurements were conducted in narrowband at 2.47 GHz in the temporal domain. On-body channels in a dual-link topology with one Tx and two Rxs were recorded on a female subject (height 170 cm, weight 65 kg) as shown in Fig. 4.1.

Figure 4.1: Test-bed and female subject in scenario-based 2.47 GHz dual-link measurements, viewed from front and back sides.

We used the Agilent PNA-X N5242A [Agi] to measure the transmission S-parameters between the antennas. Analogue to canonical measurements, the Skycross SMT-3TO10M antennas as shown in Fig. 3.2 were used. The antennas were directly attached to the skin in tangential polarization along the vertical direction, as shown in Fig. 4.1. This was found to provide small antenna return-loss on the subject. We used 4 meters and 8 meters coaxial cables to connect the antennas to the VNA. The loss from the cables is 0.45 dB per meter at 2.47 GHz, which is negligible. Table 4.1 presents the detailed informations of the VNA and the subject.

We investigated five scenarios as depicted in Fig. 4.2. The locations of the antennas in these scenarios correspond to critical regions in medical applications, such as the chest, arms, etc. The different link geometries in the scenarios are only identified by the indexes of the sce-

Input power	5 dBm	IF bandwidth	1 kHz
Frequency	2.47 GHz	Subject's height	170 cm
Polarization	tangential	Subject's weight	65 kg
Sampling rate	1 ms	Waist perimeter	77 cm
Measurement length	10 s	Hip perimeter	87 cm
Sweeping mode	CW		

Table 4.1: Contexts and subject's information in scenario-based 2.47 GHz dual-link measurements

narios.

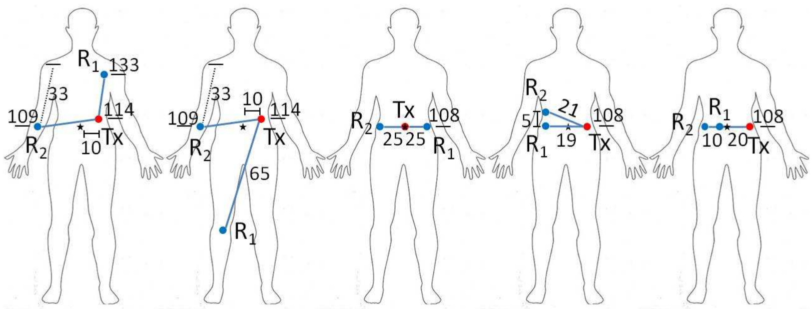

Figure 4.2: On-body link geometries in dual-link measurements, labeled as scenario 1, 2, 3, 4, and 5 from the left to the right. R_1 and R_2 represent the Rxs of channel 1 and 2. Distances marked in the figure are measured in centimeters.

Three motion modes were investigated in each scenario: sleep, sit-stand, and walk. In the sleep mode, the subject was laying on a table in a small meeting room to simulate a patient in the hospital environment, as in Fig. 4.3(a). The meeting room was an enclosed and quiet space without persons passing by. The subject was in a static posture and made natural breathing. In the sit-stand motion mode, the subject performed sequential movements of sitting down and standing up in a laboratory as shown in Fig. 4.3(b). The laboratory was less quiet than the meeting room with more objects surrounding the subject and occasional persons passing. In the walk mode, the subject walked in straight line in the same laboratory, as shown in Fig. 4.3(c). These two motion modes simulate the daily scenarios in offices and at home.

The measurement configuration is similar to the canonical measurement configuration presented in Chapter 3. Therefore, the channels are

(a) Sleep

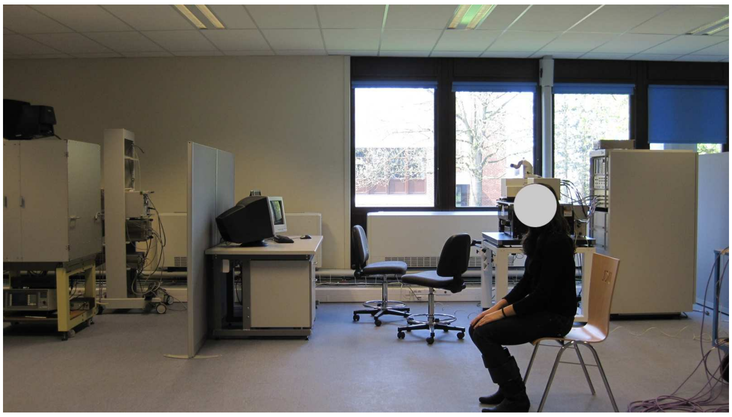

(b) Sit-stand

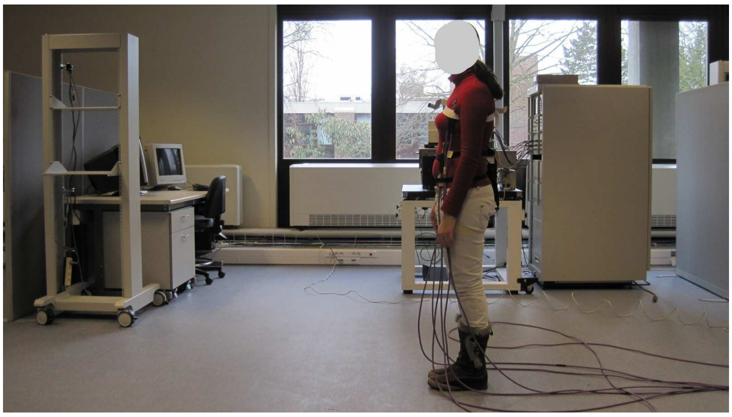

(c) Walk

Figure 4.3: Three motion modes investigated in scenario-based 2.47 GHz dual-link measurements

directly extracted from the measured S-parameters. Definitions on the pathloss, temporal fading, Doppler spectrum, and spatial channel correlation are then also similar to those in canonical measurements.

The interference by the antenna displacements was considered as a part of the channels. The average antenna return-loss, S_{11} is -9 dB in sleep, -10.2 dB in sit-stand, and -16.4 dB in walk mode, as shown in Fig. 4.4, which are sufficiently low values for the measurements.

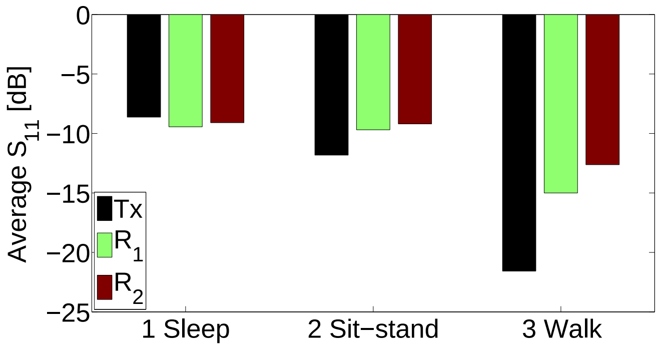

Figure 4.4: Average antenna return-loss in difference motion modes in dual-link measurements

4.1.2 Statistical characterization

4.1.2.1 Pathloss

There are both fixed-fixed and fixed-mobile on-body channels in the scenarios depicted in Fig. 4.2. Conventionally, the pathloss is defined given a deterministic propagation distance, which is not applicable to fixed-mobile on-body channels with time-varying propagation distances. However, under repetitive body motions like walking, the channel gains will vary around an average value. Therefore for fixed-mobile or mobile-mobile on-body channels, the average pathloss levels L can be estimated from the channels, and all temporal variation are covered by fading.

Fig. 4.5(a) presents the results of the pathloss in dB of both channels.

In general, we observed a weak relation between the pathloss levels and the propagation distance in the measurements. The antenna displacement, polarization mismatch, body shape variety, and off-body scattering will all increase the variation of the pathloss. Fig. 4.5(b) further compares the pathloss of the horizontal links in scenarios 3 to 5

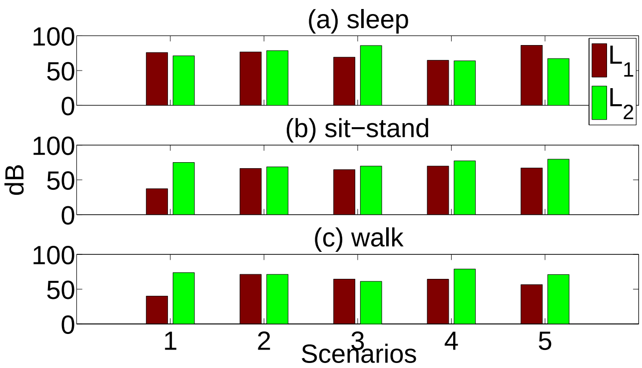

(a) Pathloss results

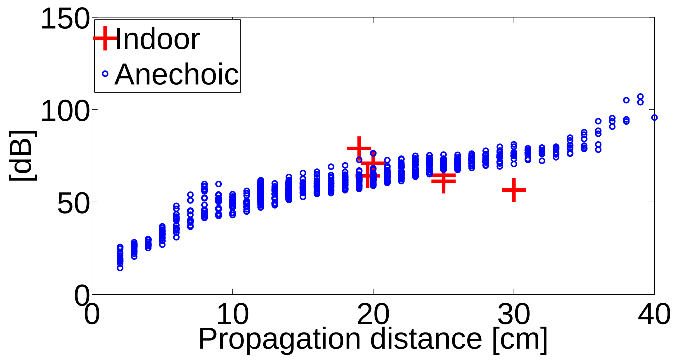

(b) Comparison between anechoic and indoor measurements in scenarios 3 to 5, walking mode

Figure 4.5: Pathloss in dB of dual-link measurements at 2.4 GHz

in Fig. 4.2, to the pathloss of corresponding links in anechoic measurements as presented in Chapter 3. A significant larger spatial variation of the pathloss in indoor environment is well observed in the figure.

The largest pathloss difference between the two links is 37.6 dB found in scenario 1, sit-stand mode. On the contrary, channels with close pathloss levels are found in scenarios 2 and 3, in sit-stand and walk modes. The pathloss changes significantly when the posture and motion mode change. An example can be found in the pathloss change of channel 1 in scenario 1 between the sleep and sit-stand modes. Table 4.2 presents a statistical summary on the mean and variation of the pathloss levels across various motion modes in each scenario.

Scenario	μ_{L_1}	σ_{L_1}	μ_{L_2}	σ_{L_2}
1	51.05	21.53	72.24	1.90
2	71.45	5.13	72.83	5.17
3	66.09	2.64	72.29	12.57
4	66.22	3.08	73.39	8.22
5	69.89	15.09	72.60	6.40

Table 4.2: Statistical summary of pathloss (dB) in each scenario across various motion modes in dual-link measurements

4.1.2.2 Temporal fading

The temporal channel fading results from the dynamic body scattering and the MPCs off the environment. We estimate the distribution of temporal fading amplitude on linear scale using the methods as we have applied in the canonical measurements. The following distribution models are evaluated: Lognormal, Gamma, Nakagami, Rayleigh, Normal, Weibull, and Exponential. Fig. 4.6(a) compares the average MSE of the estimation results in all scenarios. The Lognormal, Gamma, and Weibull distribution models have achieved low MSEs. An example of the Lognormal estimation of the fading distribution is given in Fig. 4.6(b), which matches well with the measurements. Therefore similarly to the canonical measurements, the temporal fading is modeled as following a Lognormal distribution, which is characterized by its STD in dB by Eq. 3.9.

Fig. 4.7(a) presents the results of σ_F in each scenario. The results show in general no geometric dependence and have larger spatial variation compared with the anechoic measurements presented in Chapter 2 under similar walk motion, as presented in Fig. 4.7(b). A small fading variance is observed in sleep mode, since the body was static and the environment was quiet. It is interesting to observe a larger fading variance in sit-stand mode than in walk mode. This is because the posture change from sit to stand is larger than the posture change in walk, therefore a larger dynamic variation of the body scattering is expected in the sit-stand mode. Moreover the different values of σ_F in different scenarios show the sensitivity of the dynamic body scattering to the link geometries. Table 4.3 summarizes the statistics of σ_F in each motion mode.

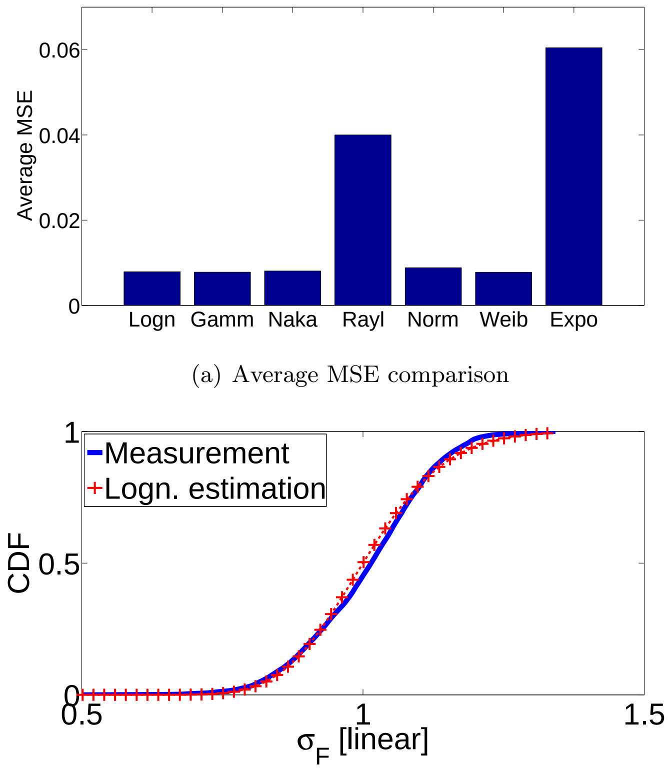

(b) An example of the Lognormal estimation for the fading distribution in scenario 3 to 5, walking mode

Figure 4.6: Temporal fading amplitude distribution on linear scale in dual-link measurements

4.1.2.3 Doppler spectrum

To evaluate the motion influences to the on-body fading, Fig. 4.8 compares the normalized average Doppler PSD of the channels in different motion modes. Similar to the canonical measurements, the Doppler PSDs are centered at $f_D = 0$ because of the local body movements. Moreover, the Doppler spreads are concentrated within 10 Hz, which correspond to the slow body motions.

The overall Doppler spreads are modeled by Eq. 3.11 using the parameter s_D, which is inversely proportional to the spreads. The estimation results are also presented in Fig. 4.8 with a single estimation to the mobile modes (sit-stand and walk modes) as presented in Fig. 4.8(b).

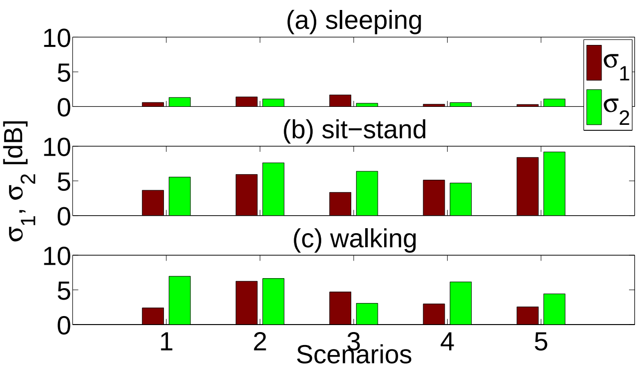

(a) Temporal fading results

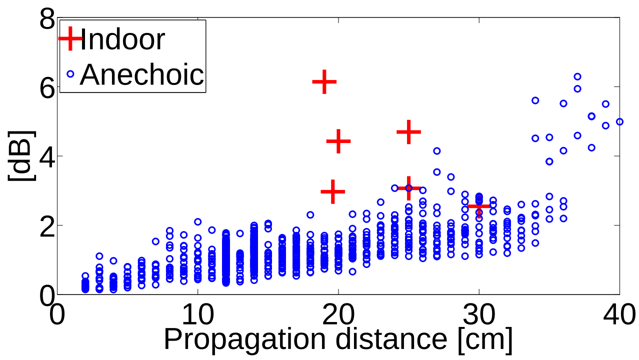

(b) Comparison between anechoic and indoor measurements in scenarios 3 to 5, walking mode

Figure 4.7: Temporal fading STD in dB in dual-link measurements

Motion modes	μ_{σ_F}	σ_{σ_F}
Sleep	0.88	0.49
Sit-stand	5.98	1.94
Walk	4.61	1.79

Table 4.3: Statistical summary of temporal fading STD in each motion mode in dual-link measurements

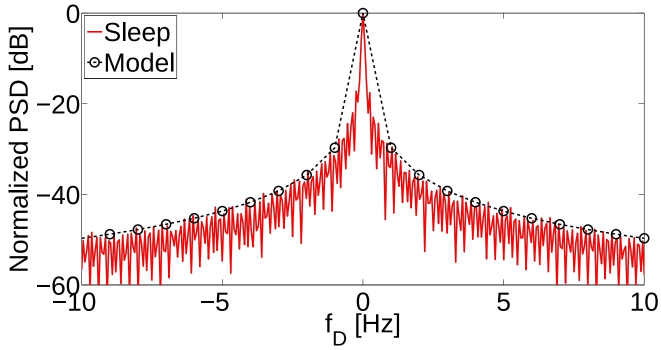

(a) Sleep, $\hat{s} = 937 W^{-1}Hz^{-2}$

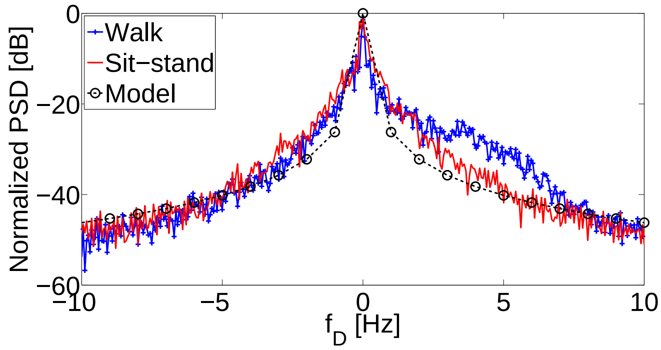

(b) Sit-stand and walk, $\hat{s} = 417 W^{-1}Hz^{-2}$

Figure 4.8: Normalized average Doppler PSD in different motion modes in dual-link measurements

The estimations show good matching to the measurements, where the estimated $\hat{s}_D$, is 937 $W^{-1}Hz^{-2}$ in sleep mode and 417 $W^{-1}Hz^{-2}$ in mobile modes. The motion effect is significant that measurements in sleep mode have much smaller Doppler spreads than in sit-stand and walk modes.

A strong PSD component is observed in the walking mode for the positive Doppler frequency shift, which is a result of a phase shift of the channels when walking. An example is shown in Fig. 4.9, selected from scenario 1, channel 2. A continuous increase of the phase is observed in Fig. 4.9(a), which cause a higher Doppler spectrum on the positive frequency shift, as shown in Fig. 4.9(b).

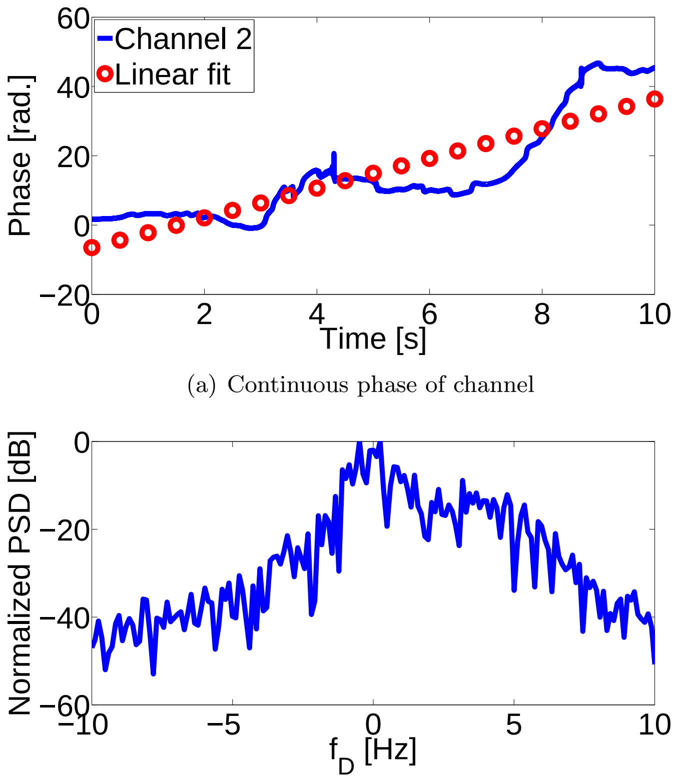

(a) Continuous phase of channel

(b) Normalized Doppler spectrum

Figure 4.9: Example of phase shift of channels in walk motion, measurement selected from scenario 1, channel 2

4.1.2.4 Spatial channel correlation

By the conclusion of Lognormally distributed fading, the spatial channel correlation in the dual-link measurements is again defined by Eq. 3.13, denoted as $\rho_{1,2}$. Fig. 4.10 presents the channel correlation in each scenario. The channels are generally uncorrelated in sit-stand and walk motion modes. It means a large spatial variation of the body scattering on different body parts.

The major observations from the results are:

- Channels in sleep mode are close to flat channels as illustrated in Fig. 4.7(a). Therefore the channel correlation in sleep mode is negligible.

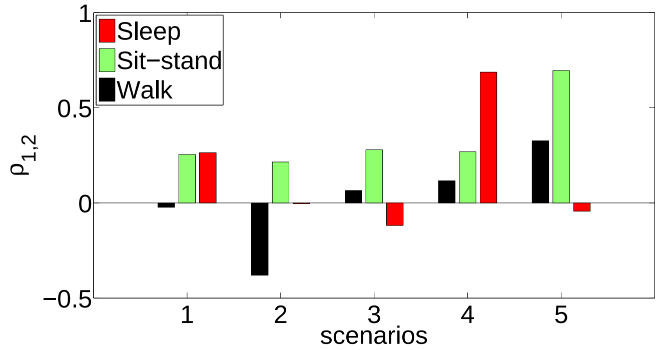

Figure 4.10: Spatial channel correlation in dual-link measurements

- A high channel correlation is found in scenario 5, sit-stand mode. In this scenario, the links have symmetric geometries on the trunk, therefore the significant posture change between sit and stand causes a synchronized dynamic fading to the channels.

- Anti-correlation, i.e. $\rho_{12} < 0$, is observed in scenario 2, walk mode. This is because that both Rxs are located on the right arm and right leg. During the walk people tends to alternate the movements of the leg and arm on the same side, which make the time-variation of the fading on the arm opposite to the fading on the leg. Similar observations were also found in [DO09].

4.2 4.2 GHz multi-link measurements

4.2.1 Measurement context

The measurements were conducted in a meeting room of approximately 5×10 meters, and were repeated on two male subjects with close sizes (180 cm) and weights (80 kg). Multi-link on-body channels were measured at 4.2 GHz in temporal domain. In the measurements, the subjects walked in the room to create dynamic body scattering.

We used the same Skycross UWB antennas as in Fig. 3.2. The subjects wore the antennas by fixing them on the clothes as in Fig. 4.11(a). The antenna-skin distances were kept as small as possible but the antennas return-loss is not addressed in the analysis. The measurements also take the antenna impacts as a part of the channels.

(a) Subject wearing antennas

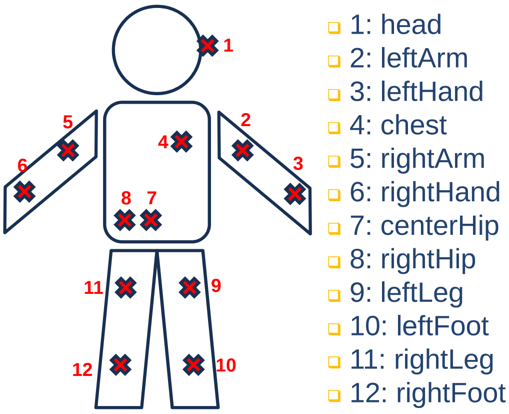

(b) Multi-link topology

Figure 4.11: Measurement context in scenario-based 4.2 GHz multi-link measurements

We measured the Channel Impulse Response (CIR) of the on-body channels by the Elektrobit channel sounder. The antennas were connected to the sounder through 6 meters coaxial cables. The Tx and Rx units of the sounder share a common clock to avoid synchronization problem. The sounder records the CIR over a bandwidth of 100 MHz. The on-body channels were estimated by trying to separate the CIRs of the on-body propagation (smaller delays) from the off-body reflection (larger delays). The final channel measurements are synthesized as narrowband on-body channels in temporal domain. Table 4.4 lists the detailed settings of the channel sounder.

Central frequency	4.2 GHz
Bandwidth	100 MHz
Input power	6 dBm
Channel sampling rate	169.7 Hz
Channel samplings/burst	4
Channel burst rate	20 Hz
Measurement length	35 s

Table 4.4: Sounder settings in scenario-based 4.2 GHz multi-link measurements

The multi-link on-body topology covers 12 positions as in Fig. 4.11(b). To meet the equipment limitation and to control the measurement complexity, in a single measurement, we only connected 8 nodes in the 12 positions to the sounder, with one node as the Tx and the rest as the Rxs.

Two channel polarizations were measured: antennas in tangential polarization to the skin in vertical direction, and antennas in normal polarization to the skin. The polarizations are described in the same z-polar coordinate system defined in the canonical measurements in Fig. 3.1(b).

4.2.2 Statistical characterization

4.2.2.1 Pathloss

The measurements contain fixed-fixed, fixed-mobile, and mobile-mobile channels. Therefore in general we estimate the average pathloss levels in the measurements. During the walk, the subjects made small local body movements, therefore the propagation distances of the fixed-mobile and mobile-mobile channels varied in a small range. We then relate the average pathloss levels to the average propagation distances to describe the general spatial dependence of the on-body pathloss. The average propagation distances were measured when the subjects were in a standing posture.

Fig. 4.12 and Fig. 4.13 present the on-body pathloss in tangential and in normal polarizations. Similar to the canonical measurements in Chapter 3, each point in the figures represents a single measurement given specific geometry, and such notation is applied to the rest of this chapter. Significant pathloss spatial variations are observed due to the complex body scattering and the antenna displacements. The measurements in tangential polarization are more sensitive to the above factors. Hence, the pathloss distribution in tangential polarization is close to a random distribution, which can be fitted as:

$$L_{dB} = 46.2 + 8.87W \tag{4.1}$$

On the contrary, pathloss levels in normal polarization in Fig. 4.13 show a clear increasing trend, which is proportional to the logarithm of the propagation distance. This is because the antennas in normal orientation to the skin are closer to LOS propagation condition.

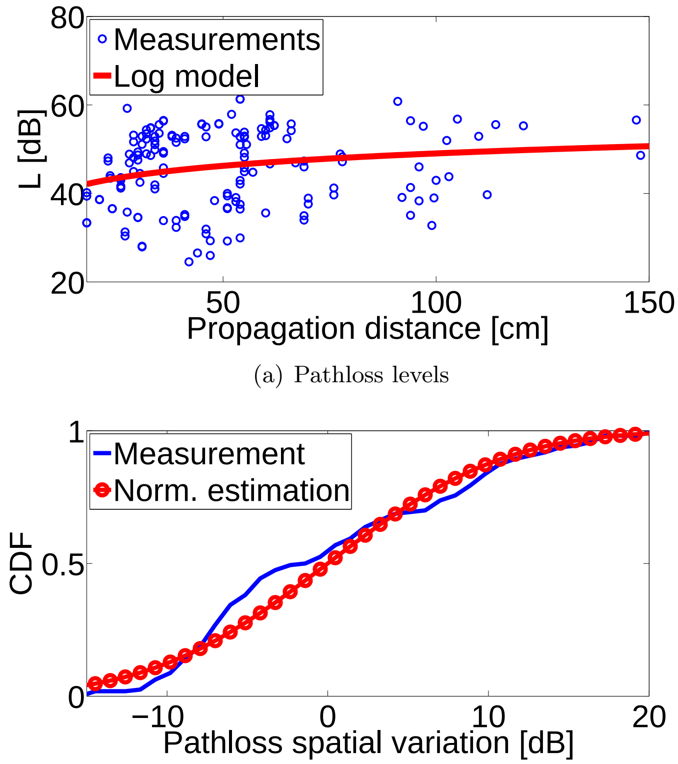

(a) Pathloss levels

(b) CDF of pathloss spatial variation

Figure 4.12: On-body pathloss in normal polarization in multi-link measurements

We therefore model the pathloss increasing rate and spatial variation as:

$$L_{dB} = L_0 + 10 n_L \lg \left(\frac{d}{d_0} \right) + \sigma_L W \quad (4.2)$$

where $d_0 = 18$ cm.

The estimation by the model in $\vec{z}$-polarization is:

$$L_{dB} = 42.11 + 9.31 \lg \left(\frac{d}{18} \right) + 8.67W \quad (4.3)$$

which has large spatial variation as in Fig. 4.12(a).

The estimation by the model in $\vec{\rho}$-polarization is:

$$L_{dB} = 23.36 + 14.68 \log \left(\frac{d}{18} \right) + 5.70W \quad (4.4)$$

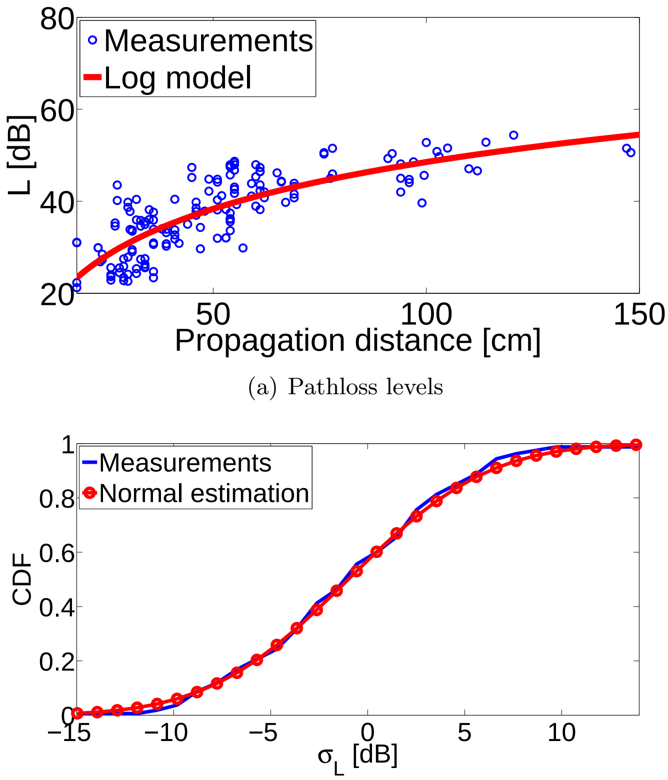

(a) Pathloss levels

(b) CDF of pathloss spatial variation

Figure 4.13: On-body pathloss in $\vec{\rho}$-polarization in multi-link measurements

which shows good fitting as in Fig. 4.13(a).

4.2.2.2 Temporal fading

We applied the same approaches as in dual-link measurements to investigate the temporal fading amplitude on linear scale. By comparing the average MSE of the estimation results as shown in Fig. 4.14, the temporal fading is again modeled as following a Lognormal distribution, characterized by its STD in dB, i.e. σ_F by Eq. 3.9. Examples of the Lognormal estimation to channels in different polarizations are given in Fig. 4.15, which pass the Kolmogorov-Smirnov test [Pap91] at significance level of 5% and match the measurements well.

Fig. 4.16 presents the results of σ_F in both polarizations. Increasing

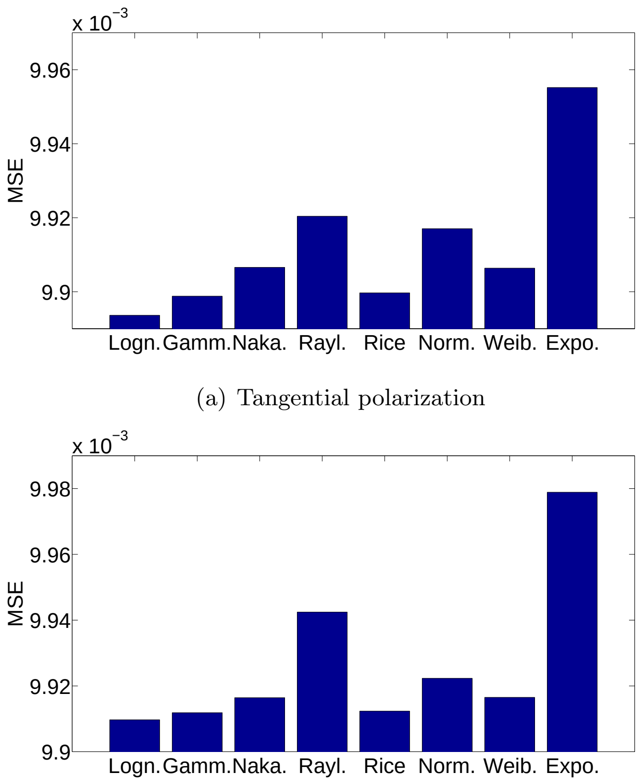

(a) Tangential polarization

(b) Normal polarization

Figure 4.14: Average MSE comparison of estimation results of fading amplitude distribution on linear scale in multi-link measurements

trends and significant spatial variation of σ_F are observed, which are modeled as:

$$\sigma_F = \sigma_{F0} + n_F \lg\left(\frac{d}{d_0}\right) + \sigma_{\sigma_F} W \tag{4.5}$$

where d is measured in centimeters and $d_0 = 18$ cm.

The estimation by the model in tangential polarization is:

$$\sigma_F = 4.06 + 2.53 \lg\left(\frac{d}{18}\right) + 1.43W, \tag{4.6}$$

and as for the normal polarization:

$$\sigma_F = 2.80 + 4.32 \lg\left(\frac{d}{18}\right) + 1.29W. \tag{4.7}$$

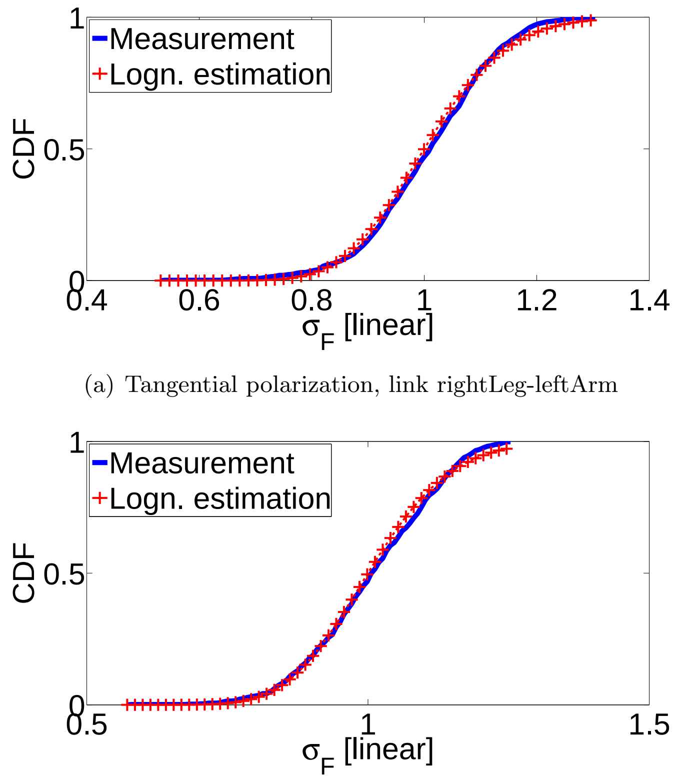

(a) Tangential polarization, link rightLeg-leftArm

(b) Normal polarization, link rightLeg-rightArm

Figure 4.15: Examples of Lognormal estimation of the fading distribution in different polarizations

The estimation results are depicted in Fig. 4.16. Again the model matches the measurements better in $\vec{\rho}$-polarizations due to LOS propagation.

4.2.2.3 Doppler spectrum

The normalized average Doppler PSDs of the overall, fixed-fixed, fixed-mobile, and mobile-mobile channel measurements are estimated respectively. Fig. 4.17 compares the results in two polarizations. The first observation is that the Doppler spreads increase as the mobility of the channel increases from fixed-fixed to mobile-mobile. The second observation is that peaks are found on the spectra at frequency harmonics, which correspond to the cycle of the walk (around 1.5 seconds).

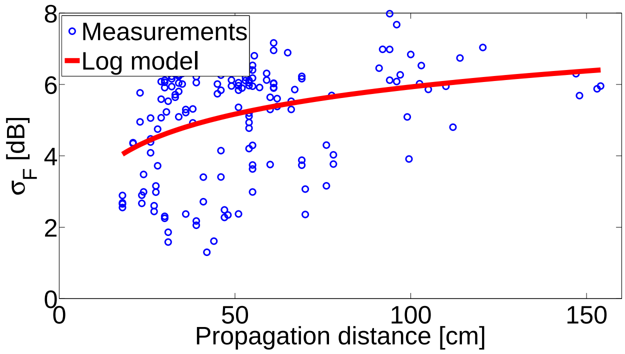

(a) Tangential polarization

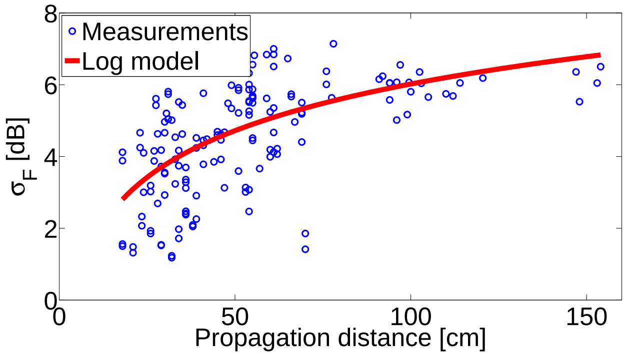

(b) Normal polarization

Figure 4.16: Temporal fading STD in dB in multi-link measurements

The Doppler model in Eq. 3.12 is not applied, because the measurements from the sounder contain significant noise and residual off-body scattering components.

4.2.2.4 Spatial channel correlation

The investigated channels are generally uncorrelated, hence there is weak relationship between the link geometries and the channel correlations. Fig. 4.18 presents the overall distribution of the channel correlation coefficients by Eq. 3.13 in two polarizations, which follow a truncated normal distribution. Table 4.5 summarizes the statistics of the channel correlation.

Correlated channels, as referred to channels having correlation coefficient larger than 0.5, are listed in Table 4.6 and Table 4.7 in both

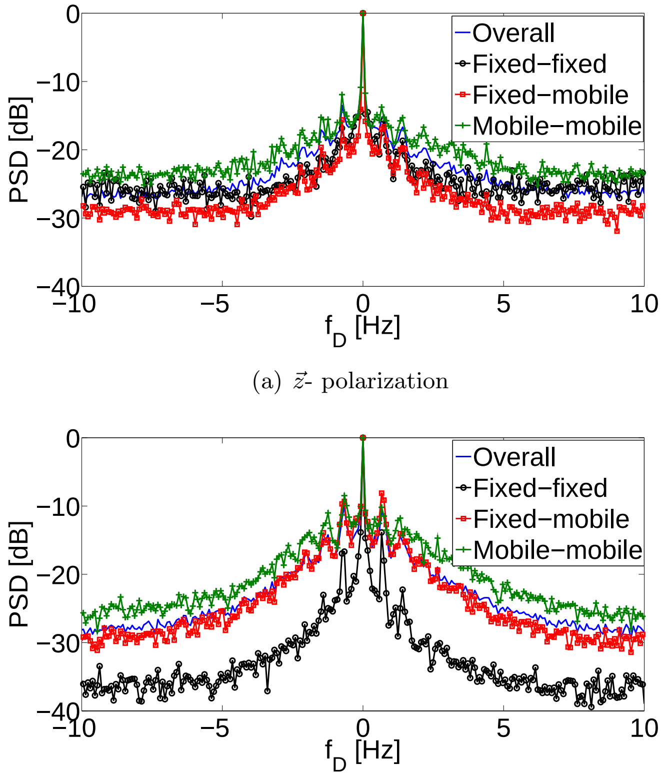

(a) $\vec{z}$- polarization

(b) $\vec{z}$- polarization

Figure 4.17: Comparisons of Doppler PSD in different link mobilities in multi-link measurements

polarizations. These correlations are found generally in two particular link configurations. The first one is when the Rx nodes are placed on the left arm and left hand respectively. The movement of the left arm during the walk will move both Rxs in the same direction, hence it generates synchronized fading. The second one is when the Rx nodes are placed on the center hip and right hip respectively. In the second configuration, both nodes are closely placed, therefore the channels will receive similar dynamic body scattering and exhibit similar temporal fading.

The correlation results are further compared to the dual-link measurements at 2.47 GHz. The channel correlation in scenario 1 of the dual-link measurements in Fig. 4.2 is selected, which is compared to the link correlation between link rightHip/centerHip-rightHand and link

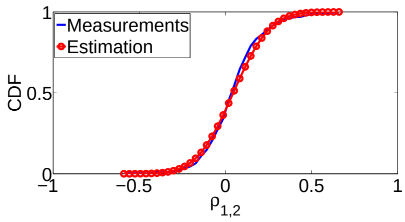

(a) $\vec{z}$ polarization

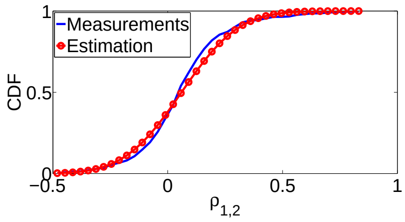

(b) $\vec{\rho}$ polarization

Figure 4.18: Distribution of spatial channel correlation in multi-link measurements

Scenario	$\mu_{\rho_{1,2}}$	$\sigma_{\rho_{1,2}}$
Tangential polarization	0.0456	0.1673
Normal polarization	0.06	0.1957

Table 4.5: Statistical summaries of spatial channels correlation in multi-link measurements

Tx	R_1	R_2	$\rho_{1,2}$
right leg	center hip	right hip	0.56
head	left arm	left hand	0.66
right hand	center hip	right hip	0.60
left arm	left hand	chest	0.62
right foot	center hip	right hip	0.53
right foot	right hip	right leg	0.50

Table 4.6: Correlated on-body channels observed in $\vec{z}$ polarization in multi-link measurements

Tx	R_1	R_2	$\rho_{1,2}$
right leg	left arm	left hand	0.59
left arm	center hip	right hip	0.79
left hand	center hip	right hip	0.55
chest	left arm	left hand	0.62
right hand	center hip	right hip	0.72
left hand	center hip	right hip	0.75

Table 4.7: Correlated channels observed in $\vec{\rho}$ polarization in multi-link measurements

rightHip/centerHip-chest at 4.2 GHz, as shown in Fig. 4.19. Under such link geometry, the links are in general uncorrelated at both frequencies. This means that the links do not receive either the common body scattering or synchronized node motion for their correlation.

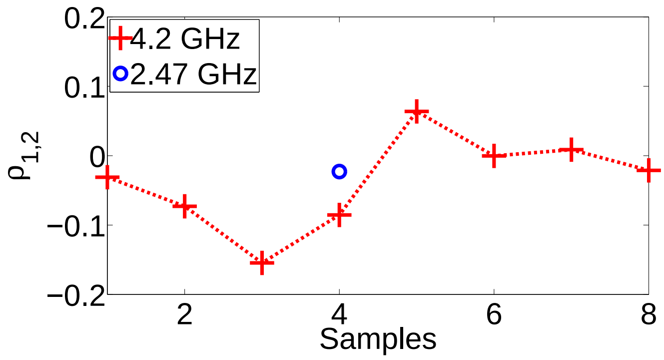

Figure 4.19: Comparison of channel correlation in tangential polarization at 4.2 GHz and 2.47 GHz

4.3 Conclusion of spatial channel correlation

Because of a large variation of link geometries, the on-body channels are generally uncorrelated in the scenario-based measurements. The correlated channels in the measurements are strongly related to the motion modes. Similar to the canonical measurements, fixed-fixed on-body channels are correlated because they receive common scattering from the body within a limited area. Mobile channels are formed by nodes that move along with the body, hence the channel correlation is explained by the pattern of the body motions. The two mechanisms explain most of the correlated on-body channels observed in the scenario-based measurements.

CHAPTER 5

Analytical on-body channel modeling

In Chapter 3 and Chapter 4, empirical models have been widely applied to describe the on-body channel statistics based on measurements, which are efficient to reflect the reality as also studied in [FDR+05, MCC+06, HAZ+06, LDDO09]. To further understand the physical mechanisms of on-body propagation, analytical modeling is presented in this chapter. Although sophisticated simulations such as Finite-Difference Time-Domain (FDTD) and ray-tracing [ZHAP06, RJV+07, ZSH+09] can provide high-resolution field description on static bodies, extending these simulations into dynamic scenarios is too costly. Analytical models, as studied in [FKC+10, GA08, MZ09], are usually developed on a simplified geometric description of the human body. It is a compromise between precision and efficiency to describe the essential properties of on-body channels in different domains. Analytical models are efficient to synthesize the channel statistics like the pathloss and spatial channel correlation. They also support canonical channel description to describe the spatial dependence of the channel properties, serving as essential knowledge in the design of BAN communications.

The analytical model developed in this chapter describes the dynamic body scattering based on a simplified body geometry consisting of multiple parts. It is an extension from earlier work in [FKC+10]. The model is validated by deterministic and statistical comparison with the canonical on-body channel measurements in Chapter 3.

5.1 Modeling principles

The analytical model consists of two parts: a full-wave closed-form static field solution of the body scattering in near-field, and a modeling of the body motions that extends the field solution into dynamic scenarios. A basic principle to obtain a closed-form field solution of the body scattering is to simplify the shapes of the body parts, e.g. the trunk, arms, and legs, into cylinders of infinite length, and to simplify the transmitting node as a line or point source. An explicit field solution can be derived at the interested position, which is treated as the channel between the nodes. To guarantee the validity the body modeling by infinite cylinders, the on-body channels should be located in the region away from the edges of the body, such as the shoulders and the hands.

The scenario should be specified in the model. We consider the scenarios in the canonical on-body channel measurements with the particular arm swing motion. The general field solution is developed based on these scenarios but is flexible to be extended to other link geometries and body motions.

5.2 Body and antenna modeling

With respect to the scenarios investigated in the canonical on-body channel measurement in Chapter 3, we consider a walking human with a natural posture as depicted in Fig. 5.1(a). The typical body motions during the walk include the footwork and the arm swing, both of which are rhythmic and quasi-periodic. In this scenario, the Tx and the Rx of an on-body channel are both located on the trunk, as marked in Fig. 5.1(b). It is assumed that on-body propagation on the trunk is less affected by the scattering from the legs, so that the dominant body scattering effects come from the trunk and arms. Both Tx and Rx are assumed to be small-sized sensors that are fixed on the trunk with invariant positions and constant distances to the skin. We then adopt the same z-polar coordinate system as in the measurements in Fig. 3.1(b) to describe the geometry of the scenario.

In the described scenario, we use three infinite, homogeneous, and lossy cylinders to model the trunk and the arms as in Fig. 5.2(a). Although the elliptic cylinder is closer to the actual shape of the trunk as studied in [MZ09], the complexity to solve the analytical fields of elliptic cylinder scattering will be dramatically high, yet the improvement brought to the model is limited. The cylinders are vertically placed and are allowed to have parallel movements on the azimuth plane. The conductivity of the cylinders is determined by the cole-cole model [HH06]. The cylinders are assumed to be composed by dry skin with respect to the subjects in the canonical measurements. The permeability, permittivity and wavenumber in free-space and in the cylinders are denoted by (μ_0, ϵ_0, k_0) and (μ_c, ϵ_c, k).

The Tx and Rx antennas are modeled by points. The Tx antenna is modeled by a polarized point source with constant electric current

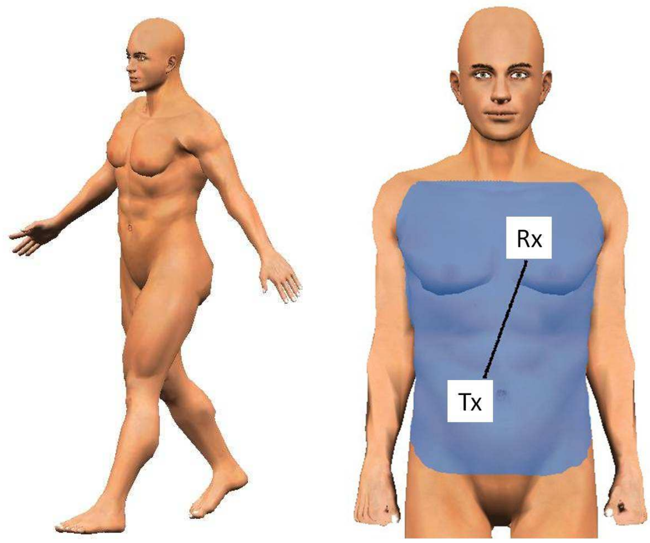

(a) A walking scenario in normal posture and movements (b) Channel distribution. The Tx and Rx are both located on the trunk surface

Figure 5.1: On-body propagation scenario on a walking human

intensity, I. The polarization of the point source is described in the z-polar coordinate, as in Fig. 5.2(b). Similarly, the Rx antenna is also modeled as a polarized point described in Fig. 5.2(b). In view of the regular geometry of the body, the source is fixed at height $z = 0$, and the fields is symmetric along the $\vec{z}$ direction.

The sizes and positions of the cylinders and the source in the azimuth plane are described in the global polar coordinate system as in Fig. 5.2(c). For simplicity, the trunk cylinder is located at the global origin.

The scenario can be generalized by a number of P cylinders vertically placed and a polarized point source located in the azimuth plane $z = 0$. The radii of different cylinders are denoted as r_p, p being the index of the cylinder. We attribute a local coordinate (ϕ_p, ρ_p) to each cylinder that the center of the cylinder is located at its local origin, denoted as O_p. The position of the source in azimuth is denoted as (ϕ_s, r_s) in the global coordinate system, and (ϕ_{ps}, r_{ps}) in each local coordinate systems. In the following, the field solution is derived based on the generalized scenario.

The essential symbols that will be used in the field solution are listed in Table 5.1,

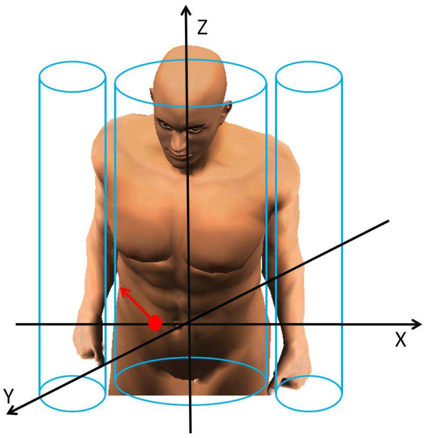

(a) Modeling of body and current source

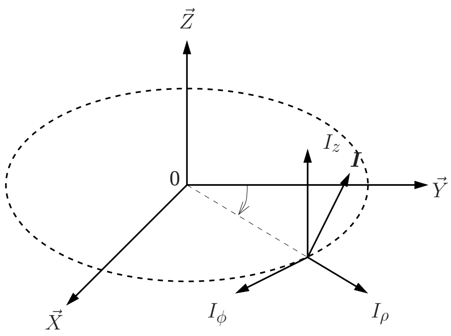

(b) Decomposition of source polarization in z-polar coordinate

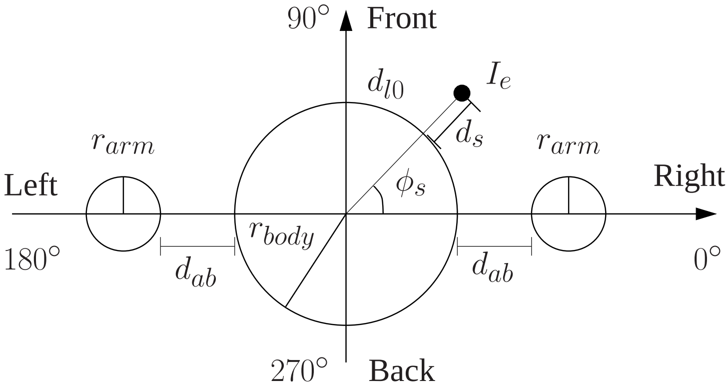

(c) Geometric quantization of the body and the source in azimuth plane. r_{body} is the trunk radius, r_{arm} is the arm radius, d_{ab} is the distance between the arm and the trunk, and d_s is the distance from the source to the trunk surface. The $d_{l0} = (r_{body} + d_s)\phi_s$ is the corresponding surface distance from the source to the trunk central.

Figure 5.2: Modeling of the human body and Tx by three lossy cylinders and one polarized point source

Number of cylinders	P
Index of cylinders	p
Cylinder radius	r_p
Source position (global)	(r_s, ϕ_s)
Source position (local)	(r_{ps}, ϕ_{ps})
Permittivity (free-space)	ϵ_0
Permeability (free-space)	μ_0
Permittivity (cylinder)	ϵ_c
Permeability (cylinder)	μ_c
Wavenumber (free-space)	$k_0 = \omega\sqrt{\epsilon_0\mu_0}$
Wavenumber (cylinder)	$k = \omega\sqrt{\epsilon_c\mu_c}$
Current intensity	I
Frequency	f
Rad	$\omega = 2\pi f$

Table 5.1: Symbols used in field solution of analytical on-body channel model

5.3 Static field solution

5.3.1 General structure

The scattering problem in the model contains two parts, the representation of point source field and the full-wave solution of multiple cylinder scattering.

In [FKC+10], an integration method was introduced to represent a point current source by inverse Fourier transform from line current source along the vertical spectral coordinate using this relationship:

$$\delta(z) = \frac{1}{2\pi}\int_{-\infty}^{\infty} e^{-jk_z z} dk_z \tag{5.1}$$

where $k_z = \sqrt{k^2 - k_\rho^2}$ is the wavenumber along the $\vec{z}$ direction, and k_ρ is the wavenumber along the $\vec{\rho}$ direction,.

Then the line source located at (r_s, ϕ_s, k_z) is expressed as:

$$\begin{aligned} \boldsymbol{J}_{line} &= \sum_{n=-\infty}^{\infty} \frac{Ie^{-jk_z z}}{\rho_s}\delta(\rho - r_s)\delta(\phi - \phi_s - n2\pi)\vec{z} \\ &= \frac{Ie^{-jk_z z}}{\rho_s}\delta(\rho - r_s)\sum_{m=-\infty}^{\infty} e^{jm\phi_s}\vec{z} \end{aligned} \tag{5.2}$$

By taking Eq. 5.2 into Eq. 5.1, the point current source is finally expressed as:

$$\boldsymbol{J} = \frac{I}{2\pi\rho_s}\delta(\rho - \rho_s)\int \sum_{m=-\infty}^{+\infty} e^{jm(\phi-\phi_s)}e^{-jk_z z}\boldsymbol{u}dk_z, \tag{5.3}$$

where $\boldsymbol{u}$ is the direction vector of the source polarization. The sum of complex exponentials in Eq. 5.3 denotes the decomposition of the line source into cylindrical current sheets.

According to Eq. 5.3, the point source scattering is equivalently expressed by the integration of line source scattering along k_z, as:

$$\begin{aligned}\boldsymbol{E}_{point}(\rho,\phi,z) &= \frac{1}{2\pi}\int_{-\infty}^{+\infty}\boldsymbol{E}_{line}(\rho,\phi,k_\rho)e^{-jk_z z}dk_z\\ \boldsymbol{H}_{point}(\rho,\phi,z) &= \frac{1}{2\pi}\int_{-\infty}^{+\infty}\boldsymbol{H}_{line}(\rho,\phi,k_\rho)e^{-jk_z z}dk_z.\end{aligned} \tag{5.4}$$

The singularity problem during in the integration is well described in [FKC+10]. In our solution, we use the following contour as the integration path of the k_z:

$$k_z = \begin{cases} a_k & |a_k| > k_0 \\ a_k + j\frac{\sqrt{k_0^2 - a_k^2}}{l_k} & |a_k| < k_0 \end{cases}, \tag{5.5}$$

where l_k is the scaling factor of the contour. With respect to the investigated scenario, we choose $l_k = 200$.

The multiple cylinder scattering has been investigated by earlier studies as in [Els94, Sch92] for plane wave propagation. We focused on the full-wave solution of a polarized line source with multiple-cylinder scattering. Conventionally, the total field is composed of the incident field from the line source and the scattered fields from the cylinders.

In principle, both the incident field of a line source and the scattered field of an infinite cylinder can be numerically decomposed into the summation of cylindrical harmonics [FKC+10]. In a z-polar coordinate system (z, ρ, ϕ) the decomposition of the fields at order m has a uniform expression along the z direction:

$$\begin{aligned}E_{m,z}(\rho,\phi) &= \begin{cases} X_m^e J_m(k_\rho\rho)e^{jm(\phi-\phi_s)} & \rho \le r \\ Y_m^e H_m^{(2)}(k_{\rho 0}\rho_p)e^{jm(\phi-\phi_s)} & \rho > r \end{cases}\\ H_{m,z}(\rho,\phi) &= \begin{cases} X_m^h J_m(k_\rho\rho)e^{jm(\phi-\phi_s)} & \rho \le r \\ Y_m^h H_m^{(2)}(k_{\rho 0}\rho)e^{jm(\phi-\phi_s)} & \rho > r \end{cases},\end{aligned} \tag{5.6}$$

where where J_m is the Bessel function of the first kind, and $H_m^{(2)}$ is the Hankel function of the second kind. X_m^e, Y_m^e, X_m^h, and Y_m^h are the parameters of the fields at order m.

The components along the ϕ and ρ can be derived from Eq. 5.6 by [FKC+10, Che95], expressed as:

$$E_{m,\phi} = \begin{cases} \frac{1}{k_1^2}(X_m^e \frac{mk_z}{\rho} J_m(k_1\rho) + j\omega\mu_1 k_1 X_m^h J_m'(k_1\rho))e^{jm(\phi-\phi_s)} & \rho \leq r \\ \frac{1}{k_2^2}(Y_m^e \frac{mk_z}{\rho} H_m^{(2)}(k_2\rho) + j\omega\mu_2 k_2 Y_m^h H_m'^{(2)}(k_2\rho))e^{jm(\phi-\phi_s)} & \rho > r \end{cases}$$
$$H_{m,\phi} = \begin{cases} \frac{1}{k_1^2}(X_m^h \frac{mk_z}{\rho} J_m(k_1\rho) - j\omega\epsilon_1 k_1 X_m^h J_m'(k_1\rho))e^{jm(\phi-\phi_s)} & \rho \leq r \\ \frac{1}{k_2^2}(Y_m^e \frac{mk_z}{\rho} H_m^{(2)}(k_2\rho) - j\omega\epsilon_2 k_2 Y_m^h H_m'^{(2)}(k_2\rho))e^{jm(\phi-\phi_s)} & \rho > r \end{cases}$$
$$E_{m,\rho} = \begin{cases} \frac{1}{k_1^2}(-jk_z k_1 X_m^e J_m'(k_1\rho) + \frac{\omega\mu_1 m}{\rho} X_m^h J_m(k_1\rho))e^{jm(\phi-\phi_s)} & \rho \leq r \\ \frac{1}{k_2^2}(-jk_z k_2 Y_m^e H_m'^{(2)}(k_2\rho) + \frac{\omega\mu_2 m}{\rho} k_2 Y_m^h H_m^{(2)}(k_2\rho))e^{jm(\phi-\phi_s)} & \rho > r \end{cases}$$
$$H_{m,\phi} = \begin{cases} \frac{1}{k_1^2}(-jk_z k_1 X_m^e J_m'(k_1\rho) - \frac{\omega\epsilon_1 m}{\rho} k_1 X_m^h J_m'(k_1\rho))e^{jm(\phi-\phi_s)} & \rho \leq r \\ \frac{1}{k_2^2}(-jk_z k_2 Y_m^e H_m^{(2)}(k_2\rho) - \frac{\omega\epsilon_2 m}{\rho} k_2 Y_m^h H_m'^{(2)}(k_2\rho))e^{jm(\phi-\phi_s)} & \rho > r \end{cases}, \tag{5.7}$$

where (k_1, μ_1, ϵ_1) and (k_2, μ_2, ϵ_2) represent the conductivity parameters inside and outside the boundary r. For the incident field, $r = r_s$ is the position of line source. For the scattered fields, $r = r_p$ is the surface of the cylinder. In Eq. 5.7, the $H_m'^{(2)}$ and J_m' are the derivatives of the Hankel and Bessel functions. The above field representation can be applied in both global coordinate and local coordinates.

In Eq. 5.3, the line source inherits the polarization of the point source. The source current is then decomposed into polarization components along $\vec{z}$, $\vec{\phi}$, and $\vec{\rho}$ directions, as in Fig. 5.2(b). The current intensities of the polarization components fulfill $I = \sqrt{|I_\rho|^2 + |I_\phi|^2 + |I_z|^2}$. The total incident field is then the summation of the incident field from each polarization component. With the principles in [FKC+10, Che95], the incident fields from each polarization component along each direction can be expressed as a summation of cylindrical harmonics over different orders m, as:

$$\begin{aligned} E_{m,\alpha}^i &= E_{m,\alpha}^{iz} + E_{m,\alpha}^{i\phi} + E_{m,\alpha}^{i\rho} \\ H_{m,\alpha}^i &= H_{m,\alpha}^{iz} + H_{m,\alpha}^{i\phi} + H_{m,\alpha}^{i\rho}, \end{aligned} \tag{5.8}$$

where $E_{m,\alpha}^{i\beta}$ and $H_{m,\alpha}^{i\beta}$, $\alpha = z/\phi/\rho$, $\beta = z/\phi/\rho$, denote the incident E and H fields from the $\vec{\beta}$ polarization component along the $\vec{\alpha}$ direction at order m. Eq. 5.8 provides a complete structure of the incident field of a current source in arbitrary direction of polarization.

The total scattered fields can be viewed as the summation of the individual scattered field from each cylinder. The individual scattered field from each cylinder is expressed at its local coordinate (ρ_p,ϕ_p), where the local coordinate of the line source is denoted as (ρ_{ps}, ϕ_{ps}). Normally, at order m, the scattered field from cylinder p along z direction is expressed as:

$$E^{s,p}_{m,z}(\rho_p, \phi_p) = \begin{cases} A^p_m J_m(k_\rho \rho_p) e^{jm(\phi_p - \phi_{ps})} & \rho_p \leq r_p \\ B^p_m H^{(2)}_m (k_{\rho 0}\rho_p) e^{jm(\phi_p - \phi_{ps})} & \rho_p > r_p \end{cases}$$
$$H^{s,p}_{m,z}(\rho_p, \phi_p) = \begin{cases} C^p_m J_m(k_\rho \rho_p) e^{jm(\phi_p - \phi_{ps})} & \rho_p \leq r_p \\ D^p_m H^{(2)}_m (k_{\rho 0}\rho_p) e^{jm(\phi_p - \phi_{ps})} & \rho_p > r_p \end{cases}, \qquad (5.9)$$

The scattered field along the other directions ϕ and ρ can be directly derived via Eq. 5.7.

The parameters (A^p_m, B^p_m, C^p_m, D^p_m) can be solved by satisfying the following boundary conditions on each cylinder surface.

$$E^{t,p}_{z1} = E^{t,p}_{z2} \quad E^{t,p}_{\phi 1} = E^{t,p}_{\phi 2} \quad \rho_p = r_p$$
$$H^{t,p}_{z1} = H^{t,p}_{z2} \quad H^{t,p}_{\phi 1} = H^{t,p}_{\phi 2} \quad \rho_p = r_p, \qquad (5.10)$$

where e.g. $E^{t,p}_{z1}$ and $E^{t,p}_{z2}$ represent the total E fields along the $\vec{z}$ direction just inside and outside the surface of cylinder p. The total fields outside cylinder p include the incident field from the line source expressed at local coordinate p and with a local decomposition of I_z, I_{ρ_p}, and I_{ϕ_p} by Eq. 5.8. In the presence of multiple cylinders, the total field outside cylinder p should also include the scattered fields from the other cylinders q, which are originally expressed in local coordinates q. As a result, the boundary condition $E^{t,p}_{z1} = E^{t,p}_{z2}$ in Eq. 5.10 is further expanded as:

$$\sum_{m=-\infty}^{+\infty} E^{s,p}_{m,z,1}(\rho_p, \phi_p) = \sum_{m=-\infty}^{+\infty} E^{i,p}_{m,z,2}(\rho_p, \phi_p) + \sum_{m=-\infty}^{+\infty}$$
$$E^{s,p}_{m,z}(\rho_p, \phi_p) + \sum_{q \neq p}^{P} \sum_{n=-\infty}^{+\infty} E^{s,q}_{n,z}(\rho_q, \phi_q) \quad \rho_p = r_p, \qquad (5.11)$$

where $E^{i,p}_{m,z}(\rho_p, \phi_p)$ is the local incident field at order m along z direction, and P is the total number of the cylinders. The same expansion should also be applied to the boundary condition $H^{t,p}_{z1} = H^{t,p}_{z2}$, while the other two in Eq. 5.10 can be derived through Eq. 5.7. This forms the basic structure of the multiple cylinder scattering.

5.3.2 Incident field

The incident field of a line source by Eq. 5.8 in a z-polar coordinate system can be expressed as a summation of cylindrical harmonics. The incident field at order m along z direction is expressed as:

$$\begin{aligned} E^i_{m,z}(\rho,\phi) &= \begin{cases} U^e_m J_m(k_\rho \rho) e^{jm(\phi-\phi_s)} & \rho \leq r_s \\ V^e_m H^{(2)}_m(k_{\rho 0}\rho_p) e^{jm(\phi-\phi_s)} & \rho > r_s \end{cases} \\ H^i_{m,z}(\rho,\phi) &= \begin{cases} U^h_m J_m(k_\rho \rho) e^{jm(\phi-\phi_s)} & \rho \leq r_s \\ V^h_m H^{(2)}_m(k_{\rho 0}\rho) e^{jm(\phi-\phi_s)} & \rho > r_s \end{cases} . \end{aligned} \tag{5.12}$$

The incident field component along ϕ and ρ direction can be derived by Eq. 5.7.

For I_z and I_ϕ polarization components, the parameters in Eq. 5.15 can be derived directly as in [FKC+10]. For I_ρ polarization component, an alternative solution of the incident field along ϕ and ρ directions is derived in [KC10].

Solution of the incident field of each polarization component is summarized in the following.

1. For $\vec{z}$ polarization [FKC+10]:

$$\begin{aligned} U^e_m &= -I_z \frac{k^2_{\rho 0}}{4\omega\epsilon_0 r} H^{(2)}_m(k_{\rho 0} r) \\ V^e_m &= -I_z \frac{k^2_{\rho 0}}{4\omega\epsilon_0 r} J_m(k_{\rho 0} r) \\ U^h_m &= 0 \\ V^h_m &= 0 \end{aligned} \tag{5.13}$$

2. For $\vec{\phi}$ polarization [FKC+10]:

$$
\begin{aligned}
U_m^e &= -I_\phi \frac{mk_z}{4\omega\epsilon_0 r} H_m^{(2)}(k_{\rho 0} r) \\
V_m^e &= -I_\phi \frac{mk_z}{4\omega\epsilon_0 r} J_m(k_{\rho 0} r) \\
U_m^h &= -I_\phi \frac{k_{\rho 0}}{4j} H_m'^{(2)}(k_{\rho 0} r) \\
V_m^h &= -I_\phi \frac{k_{\rho 0}}{4j} J_m'(k_{\rho 0} r)
\end{aligned}
\tag{5.14}
$$

3. For $\vec{\rho}$ polarization [KC10]:

   By taking $\boldsymbol{J} = I_\rho \vec{\rho}$ into Eq. 5.3, a modified addition theorem of Bessel functions should be used to produce a cylindrical wave decomposition of the incident field [KC10, FLK+09].

   The vector potential, $\boldsymbol{A}^{line}$, is calculated in a first instance, and the electric field is derived from it. For simplicity, we suppose that the source is located at $\phi_s = 0$, hence the $\vec{\rho}$ direction equals to the $\vec{x}$ direction. Knowing the normal polarized current source ($\boldsymbol{u} = \vec{\rho}$ in Eq. 5.3), the vector potential can then be written as in Eq. 5.15 [KC10].

$$
\boldsymbol{A}^{line} = \frac{\vec{x}}{4j} H_0^{(2)}(k_{\rho 0}|\rho - r_s|) e^{-jk_z z}, \tag{5.15}
$$

   where $\vec{x}$ is the x direction vector.

   After applying the addition theorem, the vector potential has the same ϕ-dependence as the current source, as in Eq. 5.16.

$$
\boldsymbol{A}^{line} = \frac{\vec{x}}{4j} \sum_{m=-\infty}^{+\infty} H_m^{(2)}(k_{\rho 0} r_s) J_m(k_{\rho 0} \rho) e^{j(m\phi - k_z z)}, \tag{5.16}
$$

   where the Hankel functions of the second kind has been used to represent outward-traveling waves from the line source.

   By projecting the $\boldsymbol{A}^{line}$ along $\vec{x}$ direction, its ρ and ϕ components can be obtained by:

$$
\begin{aligned}
A_\rho^{line} &= \frac{1}{8j} \sum_{m=-\infty}^{+\infty} H_m^{(2)}(k_{\rho_0} r_s) J_m(k_{\rho 0}\rho)(e^{j\phi} + e^{-j\phi}) e^{j(m\phi - k_z z)} \\
A_\phi^{line} &= \frac{-1}{8} \sum_{m=-\infty}^{+\infty} H_m^{(2)}(k_{\rho_0} r_s) J_m(k_{\rho 0}\rho)(e^{j\phi} - e^{-j\phi}) e^{j(m\phi - k_z z)}
\end{aligned}
\tag{5.17}
$$

The incident field of the source located at ϕ_s is given by replacing ϕ in Eq. 5.17 with $\phi - \phi_s$. The electric and magnetic incident fields are then derived from the vector potentials in Eq. 5.17, which are replaced in Eq. 5.8 to obtain the numerical expression of the incident field from the ρ polarization component.

The total incident field of an arbitrarily polarized source at order m is obtained through Eq. 5.8 given the field.

5.3.3 Scattered field

To find the explicit boundary condition of cylinder p at order m in Eq. 5.10, the representation of the scattered fields from cylinder q have to be transformed from local coordinate q to local coordinate p in Eq. 5.9. For the $E_z^{s,q}$ scattered field of cylinder q at the surface of cylinder p, the field is expressed as:

$$
E_z^{s,q} = \sum_{m=-\infty}^{\infty} B_m^p H_m^{(2)}(k_{\rho 0}\rho_q) e^{jm(\phi_q - \phi_{qs})} \tag{5.18}
$$

By Graf's addition theorem in [ASM64, G.N22], we have:

$$
H_m^{(2)}(k_0\rho_q) e^{jm(\phi_q - \phi_{pq})} = \sum_{n=-\infty}^{\infty} H_{m+n}^{(2)}(kd_{pq}) J_n(k\rho_p) e^{jn(\pi - \phi_p + \phi_{pq})}, \tag{5.19}
$$

where (d_{pq}, ϕ_{pq}) is the position of local origin O_p in local coordinate q.

By taking Eq. 5.19 into Eq. 5.18, we convert the scattered from local coordinate q to p. The same principle is also made on the $H_z^{s,q}$ scattered field in Eq. 5.9. Finally, the scattered fields of cylinder q at the surface of cylinder p is expressed as:

$$E_z^{s,q}(\rho_q,\phi_q) = \sum_{n=-\infty}^{+\infty} B_n^q H_n^{(2)}(k_{\rho 0}\rho_q) e^{jn(\phi_q-\phi_{qs})}$$
$$= \sum_{m,n=-\infty}^{+\infty} B_n^q H_{n-m}^{(2)}(k_{\rho 0} d_{pq}) J_m(k_{\rho 0}\rho_p)\Phi_{mp}^{nq} e^{jm(\phi_p-\phi_{ps})}, \tag{5.20}$$

$$H_z^{s,q}(\rho_q,\phi_q) = \sum_{n=-\infty}^{+\infty} D_n^q H_n^{(2)}(k_{\rho 0}\rho_q) e^{jn(\phi_q-\phi_{qs})}$$
$$= \sum_{m,n=-\infty}^{+\infty} D_n^q H_{n-m}^{(2)}(k_{\rho 0} d_{pq}) J_m(k_{\rho 0}\rho_p)\Phi_{mp}^{nq} e^{jm(\phi_p-\phi_{ps})}, \tag{5.21}$$

where $\Phi_{mp}^{nq} = e^{jm(\phi_{ps}-\phi_{pq})} e^{jn(\phi_{pq}-\phi_{qs})}$.

Replacing Eq. 5.11 by Eq. 5.21, solving the incident field at order m by Eq. 5.8, Eq. 5.13, Eq. 5.14, and Eq. 5.17, and deriving the boundary condition on the ϕ direction by Eq. 5.7, the final boundary condition on the surface of cylinder p is derived as:

$$\begin{bmatrix} J_m & -H_m^{(2)} & 0 & 0 \\ \frac{mk_z}{k_\rho^2 r_p} J_m & -\frac{mk_z}{k_{\rho 0}^2 \rho_p} H_m^{(2)} & \frac{j\omega\mu_c}{k_\rho} J'_m & -\frac{j\omega\mu_0}{k_{\rho 0}} H_m'^{(2)} \\ 0 & 0 & J_m & H_m^{(2)} \\ -\frac{j\omega\epsilon_c}{k_\rho} J'_m & \frac{j\omega\epsilon_0}{k_{\rho 0}} H_m'^{(2)} & \frac{mk_z}{k_\rho^2 \rho_p} J_m & -\frac{mk_z}{k_{\rho 0}^2 \rho_p} H_m^{(2)} \end{bmatrix} \begin{bmatrix} A_m^p \\ B_m^p \\ C_m^p \\ D_m^p \end{bmatrix} = \begin{bmatrix} E_{m,z}^{i,p}(r_p) \\ E_{m,\phi}^{i,p}(r_p) \\ H_{m,z}^{i,p}(r_p) \\ H_{m,\phi}^{i,p}(r_p) \end{bmatrix} +$$
$$\sum_{q\neq p}^{P} \sum_{n=-\infty}^{+\infty} \begin{bmatrix} 0 & H_{n-m}^{(2)} J_m \Phi_{mp}^{nq} & 0 & 0 \\ 0 & \frac{mk_z}{k_{\rho 0}^2 r_p} H_{n-m}^{(2)} J_m \Phi_{mp}^{nq} & 0 & \frac{j\omega\mu_0}{k_{\rho 0}} H_{n-m}^{(2)} J'_m \Phi_{mp}^{nq} \\ 0 & 0 & 0 & H_{n-m}^{(2)} J_m \Phi_{mp}^{nq} \\ 0 & -\frac{j\omega\epsilon_0}{k_{\rho 0}} H_{n-m}^{(2)} J'_m \Phi_{mp}^{nq} & 0 & \frac{mk_z}{k_{\rho 0}^2 r_p} H_{n-m}^{(2)} J_m \Phi_{mp}^{nq} \end{bmatrix} \begin{bmatrix} A_n^q \\ B_n^q \\ C_n^q \\ D_n^q \end{bmatrix}. \tag{5.22}$$

We use the notations in Eq. 5.23 to simplify Eq. 5.22:

$$\begin{aligned} J_m &= J_m(k_\rho r_p) \\ H_m^{(2)} &= H_m^{(2)}(k_{\rho_0} r_p) \\ H_{n-m}^{(2)} &= H_{n-m}^{(2)}(k_{\rho_0} d_{pq}) \end{aligned} \tag{5.23}$$

And the notations $E^{i,p}_{m,z}(r_p)$, $E^{i,p}_{m,\phi}(r_p)$, and $H^{i,p}_{m,z}(r_p)$ in Eq. 5.22 represent the total incident fields of the source on the surface of cylinder p at the local coordinate p.

5.3.4 Solution of boundary conditions

Eq. 5.22 describes an iterative scattering process among the multiple cylinders. We structure Eq. 5.22 by the following expression:

$$\mathbf{\Lambda}_{m,p}\mathbf{\Gamma}_{m,p} = \boldsymbol{G}_{m,p} + \sum_{q\neq p}^{P}\sum_{n=-\infty}^{+\infty} \boldsymbol{F}^{nq}_{mp}\mathbf{\Gamma}_{n,q} \tag{5.24}$$

$$\mathbf{\Gamma}_{m,p} = \mathbf{\Lambda}^{-1}_{m,p}\boldsymbol{G}_{m,p} + \sum_{q\neq p}^{P}\sum_{n=-\infty}^{+\infty} \mathbf{\Lambda}^{-1}_{m,p}\boldsymbol{F}^{nq}_{mp}\mathbf{\Gamma}_{n,q}, \tag{5.25}$$

The symbols in Eq. 5.25 correspond to the elements in Eq. 5.22 as:

$$\mathbf{\Lambda}_{m,p} = \begin{bmatrix} J_m & -H^{(2)}_m & 0 & 0 \\ \frac{mk_z}{k_\rho^2 r_p}J_m & -\frac{mk_z}{k_{\rho 0}^2 \rho_p}H^{(2)}_m & \frac{j\omega\mu_c}{k_\rho}J'_m & -\frac{j\omega\mu_0}{k_{\rho 0}}H'^{(2)}_m \\ 0 & 0 & J_m & H^{(2)}_m \\ -\frac{j\omega\epsilon_c}{k_\rho}J'_m & \frac{j\omega\epsilon_0}{k_{\rho 0}}H'^{(2)}_m & \frac{mk_z}{k_\rho^2\rho_p}J_m & -\frac{mk_z}{k_{\rho 0}^2\rho_p}H^{(2)}_m \end{bmatrix}$$

$$\mathbf{\Gamma}_{m,p} = \begin{bmatrix} A^p_m \\ B^p_m \\ C^p_m \\ D^p_m \end{bmatrix} \qquad \boldsymbol{G}_{m,p} = \begin{bmatrix} E^{i,p}_{m,z}(r_p) \\ E^{i,p}_{m,\phi}(r_p) \\ H^{i,p}_{m,z}(r_p) \\ H^{i,p}_{m,\phi}(r_p) \end{bmatrix}$$

$$\boldsymbol{F}^{nq}_{mp} = \begin{bmatrix} 0 & H^{(2)}_{n-m}J_m\Phi^{nq}_{mp} & 0 & 0 \\ 0 & \frac{mk_z}{k_{\rho 0}^2 r_p}H^{(2)}_{n-m}J_m\Phi^{nq}_{mp} & 0 & \frac{j\omega\mu_0}{k_{\rho 0}}H^{(2)}_{n-m}J'_m\Phi^{nq}_{mp} \\ 0 & 0 & 0 & H^{(2)}_{n-m}J_m\Phi^{nq}_{mp} \\ 0 & -\frac{j\omega\epsilon_0}{k_{\rho 0}}H^{(2)}_{n-m}J'_m\Phi^{nq}_{mp} & 0 & \frac{mk_z}{k_{\rho 0}^2 r_p}H^{(2)}_{n-m}J_m\Phi^{nq}_{mp} \end{bmatrix}. \tag{5.26}$$

In Eq. 5.25, $\mathbf{\Lambda}_{m,p}$ is the scattering matrix of cylinder p at order m, $\mathbf{\Gamma}_{m,p}$ is the scattered field parameter vector of cylinder p at order m, $G_{m,p}$ is the incident field vector in local coordinate p at order m, and $\boldsymbol{F}^{nq}_{mp}$ is the mutual scattering matrix of cylinder q at order n to the scattered field of cylinder p at order m.

Eq. 5.25 describes two mechanisms resulting the scattered field of cylinder p: $\mathbf{\Lambda}^{-1}_{m,p}\boldsymbol{G}_{m,p}$ is the scattered field of the first order directly excited by the incident field from the source; $\sum_{q\neq p}^{P}\sum_{n=-\infty}^{+\infty}\mathbf{\Lambda}^{-1}_{m,p}\boldsymbol{F}^{nq}_{mp}\mathbf{\Gamma}_{n,q}$

is the summation of the scattered fields of higher orders excited by the scattered fields from the other cylinders. This mutual scattering process can be understood as that in addition to the response to the direct incident field, the scattered field of one cylinder also reacts to the scattered fields from the other cylinders, which leads to a re-excitation of higher order scattered fields. Such mutual scattering is expected to reach a convergence when the order of the re-scattered fields increases. Therefore, we propose an iterative algorithm to approximate the final scattered fields based on the mutual scattering:

1. Let $\mathbf{\Gamma}_m^{p|(i)}$ be the parameters of the scattered field at iteration i, $i = 0, 1, 2, ...$ At the initialization stage ($i = 0$), all scattered fields are 0.

2. At iteration i, the scattered fields are updated following Eq. 5.25 until it reaches convergence.

$$\mathbf{\Gamma}_m^{p|(i)} = \mathbf{\Lambda}_{mp}^{-1}\boldsymbol{G}_{mp} + \sum_{q\neq p}^{P}\sum_{n=-\infty}^{+\infty}\mathbf{\Lambda}_{mp}^{-1}\boldsymbol{F}_{mp}^{nq}\mathbf{\Gamma}_n^{q|(i-1)} \tag{5.27}$$

This algorithm provides a consistent structure of the scattered fields over iterations, expressed as:

$$\mathbf{\Gamma}_m^{p|(i)} = \mathbf{\Lambda}_{mp}^{-1}\boldsymbol{G}_{mp} + \sum_{u=1}^{i}\mathbf{\Theta}_u \tag{5.28}$$

$$\mathbf{\Theta}_u = \sum_{1}\mathbf{\Lambda}_{mp}^{-1}\boldsymbol{F}_{mp}^{nq}\cdots\sum_{i}\mathbf{\Lambda}_{n_{u-2}q_{u-2}}^{-1}\boldsymbol{F}_{n_{u-2}q_{u-2}}^{n_{u-1}q_{u-1}}\mathbf{\Gamma}_n^{q|(1)}$$

$$\text{and:}\quad \sum_{u} = \sum_{n_{u-1}=-\infty}^{\infty}\ \sum_{q_{u-1}\neq q_{u-2}}^{P}. \tag{5.29}$$

The convergence of the iterative algorithm is validated in a simulation example at 2.45 GHz, considering a z-polarized line source with $k_z = 0$, $I_z = 1\times10^{-10}A$, $\rho_s = 15cm$, $\phi_s = 90°$, located on the trunk ($r_{body} = 14.5cm$, $r_{arm} = 3.8cm$, $d_{ab} = 3cm$). The convergence of the total field power in dB at the observation point, $\phi_s = 270°$, $\rho = 15cm$, is presented in Fig. 5.3, which reaches a stable level after 15 iterations. In practice, the number of iterations should be sufficiently large (≥ 10) so that all the interested fields can converge to a stable level.

An example of the iterative field solution on the horizontal plane of a line source given $k_z = 0$, 2.45 GHz, is presented in Fig. 5.3.4. The

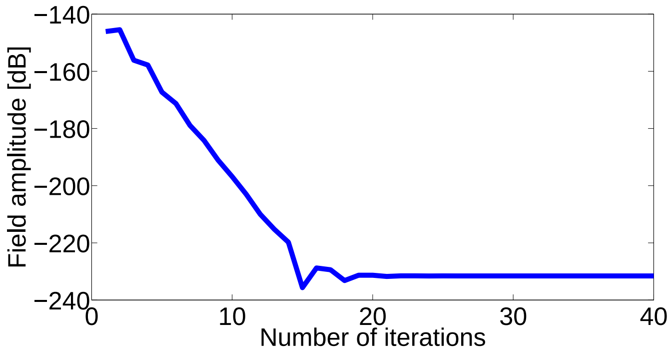

Figure 5.3: Convergence of the iterative approximation of line source in z polarization with $k_z = 0$, $I_z = 1 \times 10^{-10}A$ at 2.45 GHz, the source position: $\rho_s = 15cm$, $\phi_s = 90°$, and the observation position: $\rho = 15cm$, $\phi = 270°$)

simulation results show two resaonable impacts from the body scattering, the trunk shadowing and the extra arm shadowing at the back of the body, and the interference from the arm scattering.

Fig. 5.5 further compares the final field solutions in the azimuth plane around the trunk in single cylinder (only trunk) and multiple cylinder scattering (with arms pending down along the sides of the trunk as in Fig. 5.2(a)) in $\vec{z}$- and $\vec{\rho}$-polarizations respectively. The results show that for on-body channels on the trunk, the primary part of the total field is determined by the incident field from the source and the scattering from the trunk, while the arm scattering causes a fluctuation of the fields. Such fluctuation varies with respect to different positions of the arms, allowing a dynamic description of the arm scattering by the model, which will be discussed later. The field difference between the two polarizations is clear: on-body channels receive lower pathloss in $\vec{\rho}$ than in $\vec{z}$ polarization because of the existence of creeping waves. Such observation is similar as found in the canonical measurements in Chapter 3.

5.4 Dynamic field solution

The dynamic field solution is easily obtained as an extension of the above static field solution by incorporating a time evolution of the positions of the cylinders on the azimuth plane to simulate the arm swing during

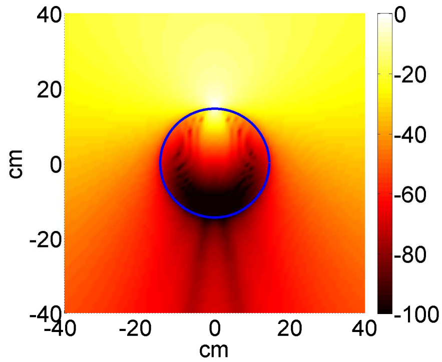

(a) Single trunk scattering

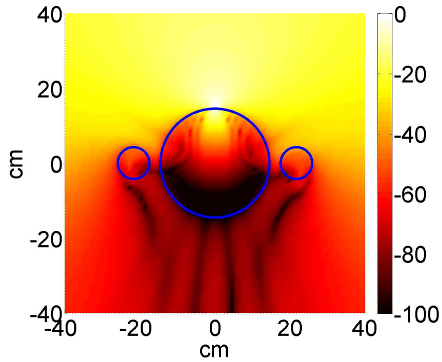

(b) Multiple cylinder scattering

Figure 5.4: Simulations of single and multiple cylinder scattering by line source in tangential polarization on the horizontal plane, 2.45 GHz, source placed in front of the trunk ($\phi_s = 90°$), antenna-skin distance $d_s = 0.5$ cm, normalized field

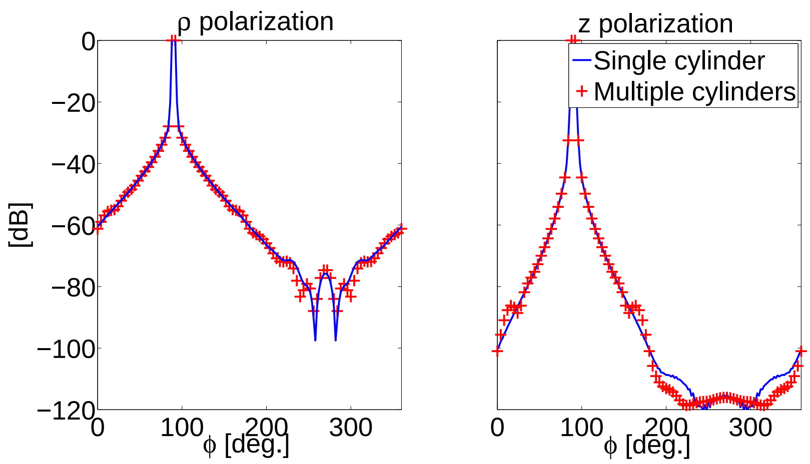

Figure 5.5: Simulations of single and multiple cylinder scattering by point source in $\vec{z}$ and $\vec{\rho}$ polarizations around the trunk, 2.45 GHz, $I = 10^{-10}A$, body geometry: ($r_{body} = 15.4cm$, $r_{arm} = 3.5cm$, $d_{ab} = 3.5cm$, $d_s = 1cm$), source placed at $\rho_s = 15cm$, $\phi_s = 90°$, fields computed at $\rho = 15cm$, $\phi = [0 - 360]°$

walking. We consider simple periodic trace functions $T_l(t)$ and $T_r(t)$ along the $\vec{y}$ direction to describe the swinging of the left and right arms. The positions of the arm cylinders are described on xy plane as:

$$[x_l(t), y_l(t)] = [-(r_{arm} + r_{body} + d_{ab}) \quad T_l(t)]$$
$$[x_r(t), y_r(t)] = [(r_{arm} + r_{body} + d_{ab}) \quad T_r(t)], \tag{5.30}$$

where $[x_l, y_l]$ and $[x_r, y_r]$ are the centers of the left and right arms.

In our study, $T_l(t)$ and $T_r(t)$ are sampled by tracing a marker attached on the swinging arms of a male subject as in Fig. 5.6(a). A digital camera recorded the arm swing at 30 frames per second. The averaged arm trace over one cycle is normalized into 1 s. Selecting proper trace measurements is critical to obtain the desired time-variation the channels. The simulations by the model use the trace measurements as shown in Fig. 5.6(b). Usually, the synthesized time-variant fields have to be synchronized with realistic measurement observations so that the local peaks along the time-variation of the fields are matched with the corresponding local peaks in measurements.

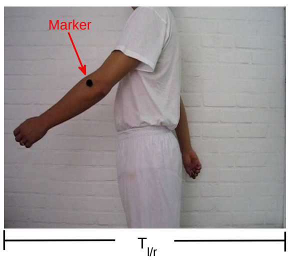

(a) Arm swing recording scenario by tracing a black marker on the arms

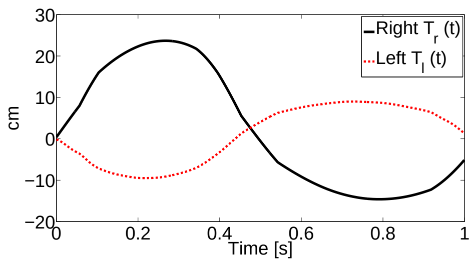

(b) Normalized trace functions over one cycle

Figure 5.6: Modeling of arm swing

5.5 Model validation

The model is evaluated by comparing the simulation results with the canonical on-body channel measurement conducted in anechoic environment. Simulations repeat the scenarios in the measurements described in Sec. 3.2, in both $\vec{z}$- and $\vec{\rho}$-polarizations, and in horizontal and vertical directions. Table 5.2 gives the settings of the parameters in the simulations.

Frequency	2.45 GHz
Tissue composition	Dry skin
ϵ_c	$3.37 \times 10^{-10} - 9.5 \times 10^{-11}j$
I	1e-10 A
Max. harmonic order	80
Max. k_z	$4k_0$
Integration step of k_z	$0.02k_0$
Scaling factor η in Eq. 5.5	200
Number of iteration in Eq. 5.27	10

Table 5.2: Simuation setup in the validation of analytical model of on-body propagation

The simulated channels are calculated by normalizing the field solution as:

$$S_{xy} = E^t(r_x, \phi_x)/E^t(r_y, \phi_y), \tag{5.31}$$

where $E^t(r_x, \phi_x)$ is the total E-field at the Rx and $E^t(r_y, \phi_y)$ is the total E-field at a position quite close to the source.

The deterministic and statistical comparisons are made in $\vec{z} - H$, $\vec{\rho} - H$, and $\vec{\rho} - V$ scenarios. Measurements in $\vec{z} - V$ scenario are limited and contain large displacements of the antenna, therefore we skip the model validation in this scenario.

5.5.1 $\vec{z} - H$ scenario

A deterministic comparison is made on the time-variation of the on-body channel. An example of channel S_{21} in the measurement identified by $d_{12} - d_{10} - d_{23} = 14 - 19 - 23$ [cm] is compared with the corresponding simulation in Fig. 5.7(a). The simulation successfully matches the local peaks of the fading amplitude in one cycle and maintains a small MSE of 1.21 dB with respect to the measurement. Both measurement and simulation show a symmetric waveform in the first and in the second half period, which is consistent with the regular arm swing. The simulation has a larger dynamic variance. A possible explanation is that, given the elliptical shape of the trunk in actual measurements, simulations based on cylinders underestimate the invariant part of the channel from the combination of the incident field and the trunk scattering. Therefore the dynamic range of the channel resulting from arm scattering is relatively increased in dB in the simulation. Such increase impacts both the amplitude and the phase of the channel. As a result, the Doppler PSD in the simulation shows higher levels at the frequency harmonics as in Fig. 5.7(b), while the relative power distributions among the frequency harmonics are close between the measurements and the simulations. The PSD of the amplitude in the simulation is much closer to the measurement, which is consistent to the matching of the time-variation of fading amplitude shown in Fig. 5.7(a).

On-body fading statistics extracted from simulations and measurements are compared. Since the simulations also cover different channel positions, spatial variation on the channel statistics is repeated in the simulations. For clarity, we only plot the local means of the channel statistics in the simulations. Because of the limited number of scenarios repeated in the simulations, the simulated local means are irregular curves along the propagation distance, as similarly observed in the measurements.

Fig. 5.8 compares the pathloss levels L in dB. The model well predicts the increasing rate of the pathloss as by the linear empirical model in Fig. 3.10(a)

Fig. 5.9 compares the temporal fading STD in dB (σ_F). The simulation results also successfully predict the increasing rate of σ_F as observed in the measurements when the propagation distance is smaller than 15 cm. The σ_F in the simulations increases faster in a larger propagation distance, which is again explained by the trunk shape mismatch in the simulations to overestimate the interference from the arm scattering.

The spatial channel correlation between S_{21} and S_{31} is compared in Fig. 5.10 on two examples of measurement results with d_{12}=12 cm and d_{12}=14 cm respectively. The simulation results predicts a close decreasing trend of the $\rho_{21,31}$ along the d_{23}, as experimentally observed.

5.5.2 $\vec{\rho} - H$ scenario

The time-variations of the arm scattering to the on-body channels in $\vec{\rho}$-polarized scenarios are expected to deviate from the simulations because of two reasons. First, the dipole antennas applied in $\vec{\rho}$-polarized scenarios contain current distribution along the normal direction as shown in Fig. 3.6. The size of the antennas impacts the channels in a more complicated way, which cannot be well matched by a point source scattering assumption. Second, the vertical on-body propagations are closer to the edges of the body (head and hands) which will violate the infinite cylinder modeling of the body. Therefore, in both $\vec{\rho} - H$ and $\vec{\rho} - V$ scenarios, we only compares the statistics of the channels.

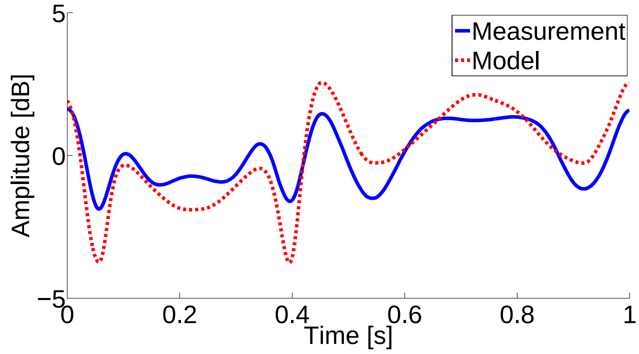

(a) Time-variation in one cycle

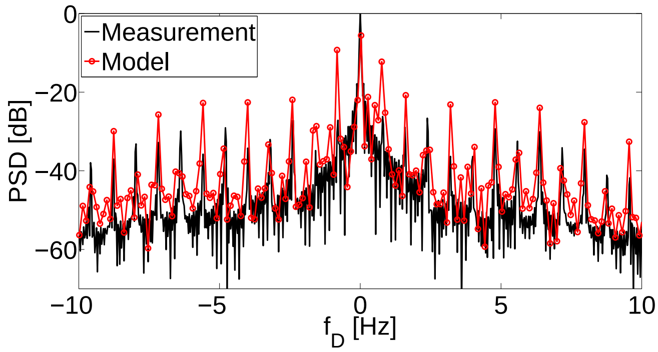

(b) Doppler PSD in one cycle

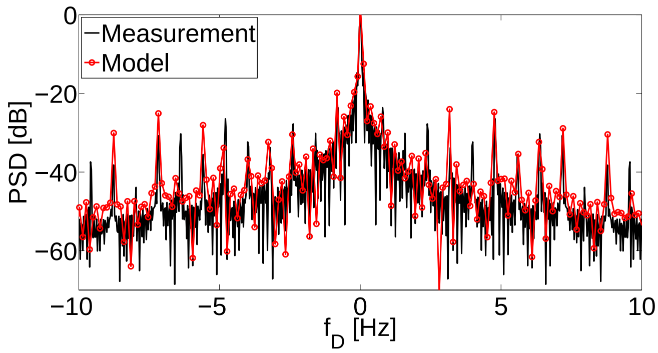

(c) PSD of channel amplitude in one cycle

Figure 5.7: Comparison of deterministic time-variation of an on-body channel in one cycle and its Doppler PSD in $\vec{z} - H$ scenario, channel sample selected from S_{12} in a measurement identified by $d_{12} - d_{10} - d_{23} = 14 - 19 - 23$

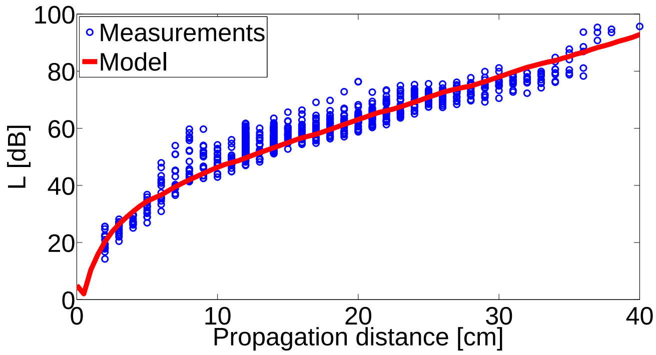

Figure 5.8: Comparisons of on-body pathloss (dB) for $\vec{z} - H$ scenario

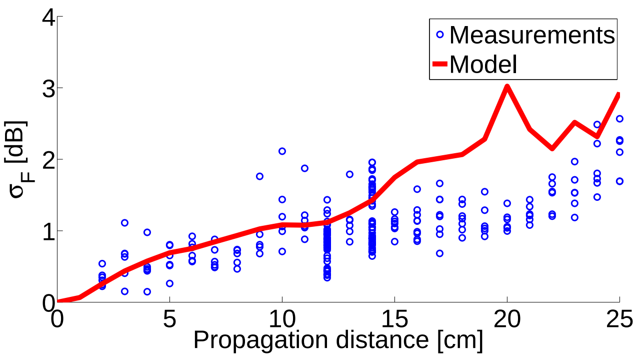

Figure 5.9: Comparison of temporal fading STD (dB) for $\vec{z} - H$ scenario

Fig. 5.11 compares the pathloss levels in dB. The increasing rate of the pathloss in the measurement results is well predicted by the simulations.

Fig. 5.12 compares the temporal fading STD in dB. The measurements with link geometries d_{12}=12 cm are selected. The corresponding simulations show close increasing rate along the propagation distance as observed in measurements.

The pathloss differences in Fig. 5.8 and Fig. 5.11, and the temporal fading STD differences in Fig. 5.9 and Fig. 5.12, highlight the impact of different polarizations on the fading statistics.

The spatial channel correlation between S_{21} and S_{31} is compared in Fig. 5.13 between the measurements with link geometries $d_{12} - d_{10} - d_{23} = 7 - 12 - d_{23}$ [cm], and the corresponding simulations. The compar-

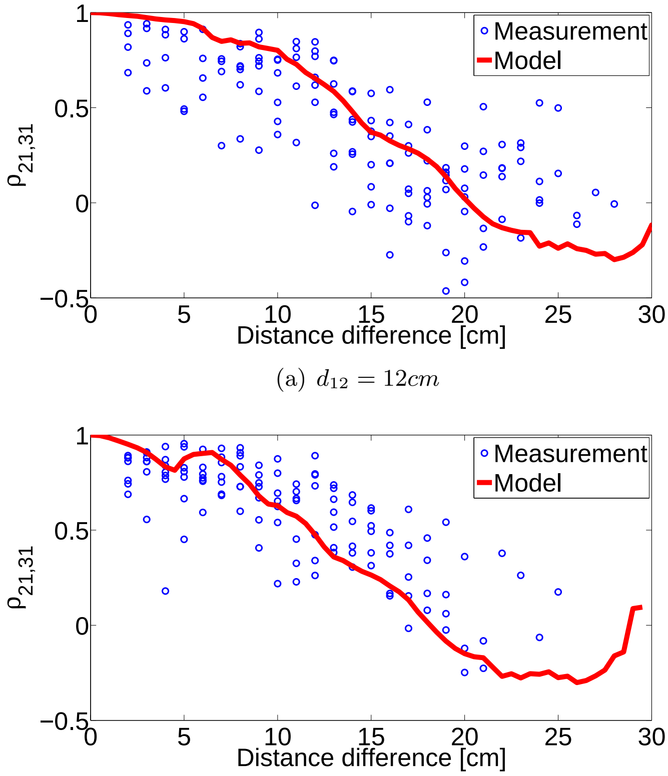

(a) $d_{12} = 12cm$

(b) $d_{12} = 14cm$

Figure 5.10: Comparison of spatial channel correlation for $\vec{z}-H$ scenario

ison shows a consistent decreasing trend of $\rho_{21,31}$ along d_{23}. The results in Fig. 5.10 and Fig. 5.13 validate the model's performance on describing the scattering similarity of horizontal on-body channels in both $\vec{z}$ and $\vec{\rho}$ polarizations.

5.5.3 $\vec{\rho} - V$ scenario

Fig. 5.5.3 compares the pathloss levels in dB. Again, the simulations predict well the increasing rate of the pathloss in the $\vec{\rho} - V$ scenario.

Fig. 5.15 compares the STD of the temporal channel fading in dB. The measurements are selected with link geometries $d_{10} = 12$ cm and $d_{20} = 4$ cm. The overall levels of σ_F in the measurements is higher than the σ_F levels in the simulations when the propagation distance is above 20 cm. Considering the actual arm swing is a rotation of the arms, the

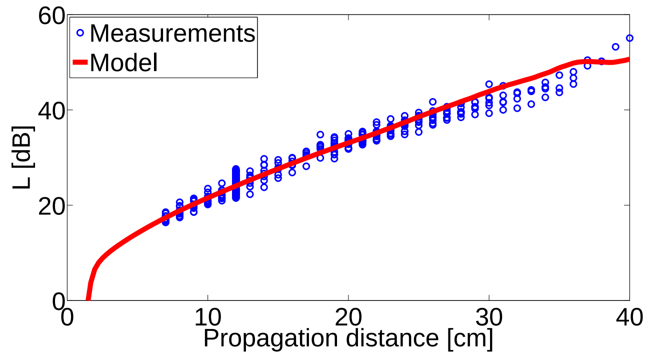

Figure 5.11: Comparison of on-body pathloss (dB) for $\vec{\rho} - H$ scenario

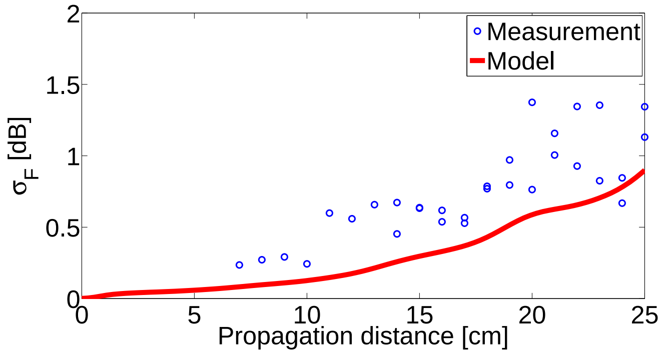

Figure 5.12: Comparison of temporal fading STD (dB) for $\vec{\rho} - H$ scenario

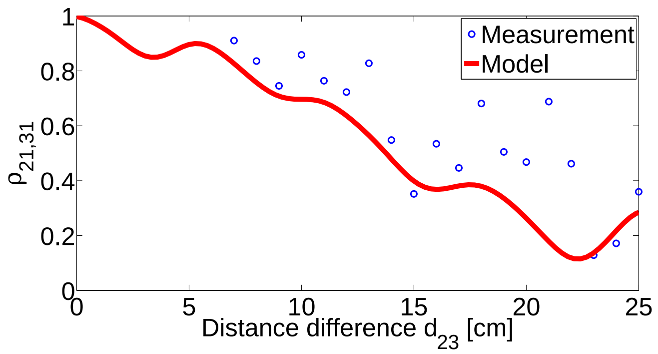

Figure 5.13: Comparisons of spatial channel correlation for $\vec{\rho} - H$ scenario, d_{10}=12 cm and d_{12}= 7 cm

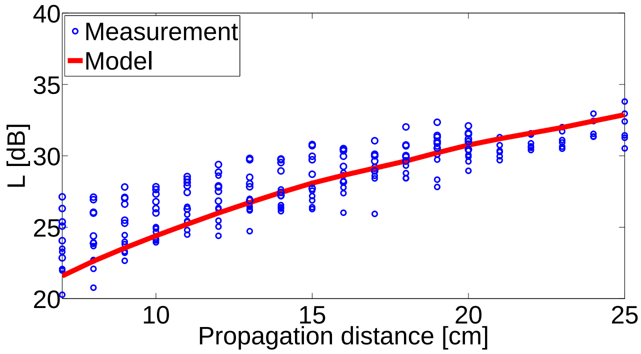

Figure 5.14: Comparison of on-body pathloss (dB) for $\vec{\rho} - V$ scenario

vertical channels in the measurements then receive a larger scattering interference than in the simulation by assuming horizontal movements of the arms. Yet, the agreement is better when the propagation distance is below 20 cm.

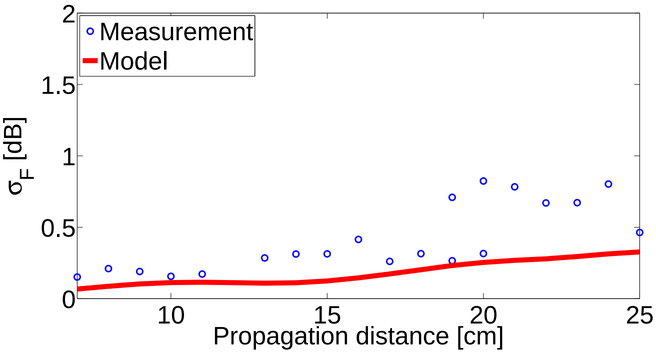

Figure 5.15: Comparison of temporal fading STD (dB) for $\vec{\rho} - V$ scenario

The comparison of the channel correlation is not made since the measured range along the vertical direction is too limited to obtain relevant results.

5.6 Model application on antenna radiation pattern

In this section, the analytical model is applied to describe the modification of on-body antenna radiation pattern in off-body communications. As described in Chapter 2, off-body channels can be described in far-field propagation by the conventional plane-wave assumption as:

$$h(t,\tau) = \int\int a(t,\tau,\boldsymbol{\Omega}_{\mathrm{Tx}},\boldsymbol{\Omega}_{\mathrm{Rx}})\boldsymbol{s}_{\mathrm{Tx}}(\boldsymbol{\Omega}_{\mathrm{Tx}})\boldsymbol{s}_{\mathrm{Rx}}(\boldsymbol{\Omega}_{\mathrm{Rx}})d\boldsymbol{\Omega}_{\mathrm{Tx}}\boldsymbol{\Omega}_{\mathrm{Rx}}, \quad (5.32)$$

where h is the complex CIR, a is the complex MPC, $\boldsymbol{s}_{\mathrm{Tx/Rx}}$ are the radiation patterns of the Tx and Rx, τ is the delay, $\boldsymbol{\Omega}_{\mathrm{Tx}}$ is the Direction-of-Departure (DoD), and $\boldsymbol{\Omega}_{\mathrm{Rx}}$ is the Direction-of-Arrival (DoA).

In conventional networks, the antenna radiation pattern is usually a deterministic parameter described in free-space. The knowledge on the antenna radiation pattern allows the systems to distinguish physical channels from the antenna impacts. The on-body node in an off-body communications receive strong body scattering effects, which means that the on-body antenna radiation pattern will be altered when viewed from off-body node. Such modification should be included in Eq. 5.32.

Describing the modification of on-body antenna radiation pattern is an abstraction of the body scattering effects in off-body communications. Without considering multiple interactions (reflections, diffractions, etc.) between the body and the environment, the environmental scattering and the body scattering are usually independently described. This approach can also help to describe the off-body scattering effect to on-body channels in realistic environments.

A comparative study was then made by both measurements and the analytical model. The results are compared to evaluate and explain the physical impacts of body scattering to the on-body antenna radiation pattern.

5.6.1 Measurement context

We conducted measurements in anechoic environment to measure the horizontal directivity of an azimuth-omnidirectional antenna close to a static human body. A SkyCross antenna in Fig. 3.2(a) was taken as the test antenna placed at the Rx side as shown in Fig. 5.16(a). A double ridged broadband horn antenna BBHA9120D was used as the reference antenna at the Tx side. The Tx and Rx were fixed at a height of 122 cm. A male subject was standing in a static posture facing the Rx at a certain distance, denoted as d_s, as shown in Fig. 5.16(b). Both the subject and the Rx were fixed on a turning table allowing a step-controlled rotation to the Tx. The Rx was located at the center of the table, and the subject stood aside as described in Fig. 5.16(b). The distance between the Rx and Tx was fixed at 3.42 m.

The transmission S-parameter between the two antennas was measured from 2 GHz to 10 GHz by the VNA. The directivity of the test antenna is calculated as:

$$D(\phi) = \frac{|S_{12}^{\text{body}}|^2}{|S_{12}^{\text{free space}}|^2} \tag{5.33}$$

where $S_{12}^{\text{free space}}$ is the measurement without the body, and S_{12}^{body} is the measurement with the body.

The antenna directivity was measured at different d_s to evaluate the effect of the body-antenna distance. At each distance, two body postures were measured, arms raising up and arms pending down, as shown in Fig. 5.6.1. Comparing between the two measurement results will show the interference from the arm scattering to the antenna directivity. Because of horizontal propagation, the body geometry is described analogue to the body geometry described in the canonical horizontal on-body measurements in Chapter 3. Table 5.3 gives the information of the subject.

Heigh/Weight	187 cm/86 kg
Trunk perimeter	93 cm
Arm perimeter	23.8 cm
Arm-trunk space	3.2 cm
Antenna height	122 cm

Table 5.3: Geometry description of the subject investigated in the measurements of on-body antenna directivity

5.6.2 Analytical modeling

The azimuth propagation between between the tested antenna and the reference antenna can be approximated by the simplified field solution of a line source given $k_z = 0$, because the fields incited by the small tested antenna along the vertical direction are symmetric and are canceled

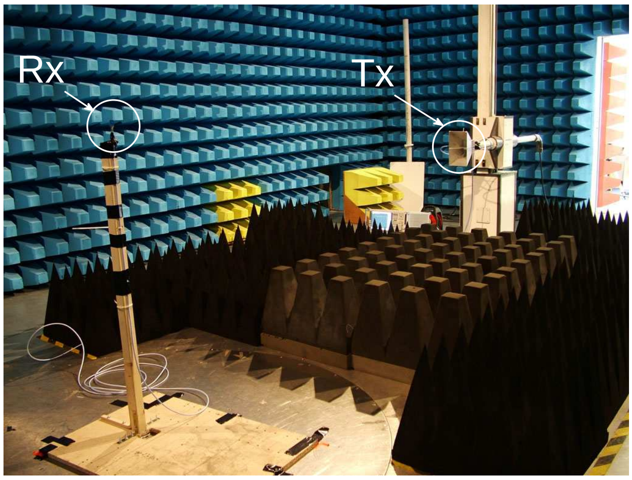

(a) Anechoic environment

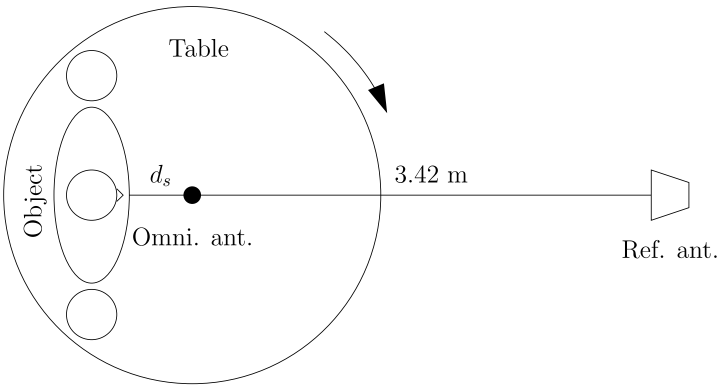

(b) Measurement scenarios

Figure 5.16: Measurement context of on-body antenna directivity

at $z = 0$. Simulations were then made based on the body geometry described in Table 5.3. Examples of the simulations can be found in Fig. 5.3.4, where the trunk shadowing at the back of the body is significant and the arm scattering increases the shadowing region when in presence. Such body scattering effect is also expected in the measurements at different frequencies.

Based on the field solution given by the model, the modified direc-

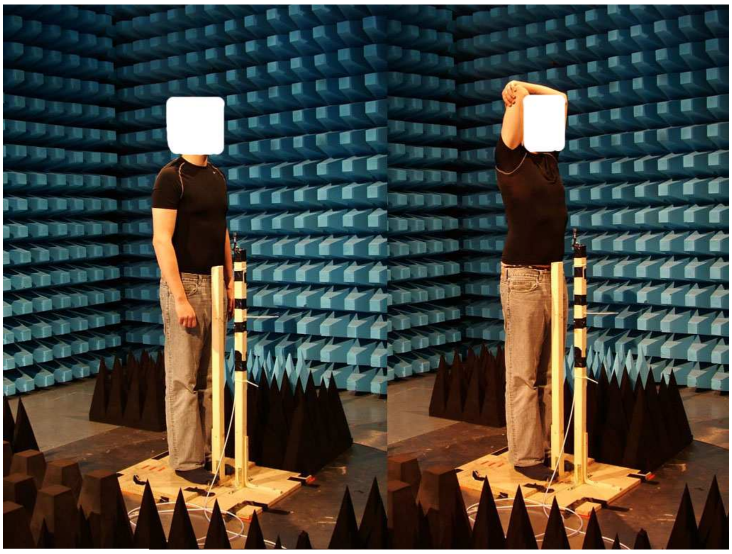

Figure 5.17: Two postures investigated in the measurements: arms raising up and arms pending down

tivity of the omni-directional line source is computed as:

$$D(\phi) = \frac{|E^t(\phi)|^2}{|E^i(\phi)|^2}, \quad (5.34)$$

where E^t and E^i are the total and incident field at the observation point.

5.6.3 Evaluation results

The simulation settings are given in Table 5.4.

Frequency	3 & 5 GHz
Tissue composition	Dry skin
ϵ_c (3 GHz)	$3.32 \times 10^{-10} - 9.23 \times 10^{-11}j$
ϵ_c (5 GHz)	$3.17 \times 10^{-10} - 9.74 \times 10^{-11}j$
I	1e-10 A
Max. harmonic order	120
Number of iteration in Eq. 5.27	10

Table 5.4: Simuation settings of on-body antenna directivity in UWB

Fig. 5.18 and Fig. 5.19 present the measurement results at 3 GHz and 5 GHz, when d_s=5 cm and d_s=15 cm respectively. The results show

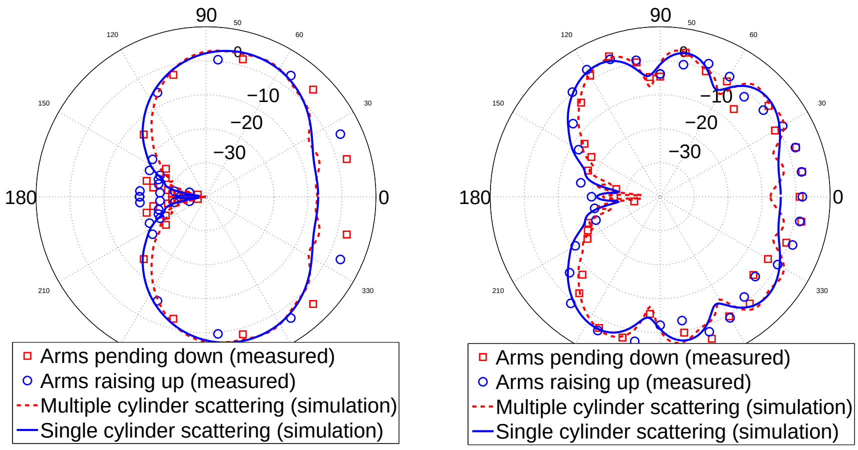

(a) (b)

Figure 5.18: Comparison of on-body antenna directivity between measurement results and simulations at 3 GHz. (a) d_s=5 cm, and (b) d_s=15 cm

a clear shadowing effect at the back side of the body, which matches the corresponding simulations. On the contrary, larger mismatches of the model are found on the front side of the trunk, which is due to the shape mismatch between the actual trunk and the cylinder in the model.

Comparison in Fig. 5.18(a) misses the front central of the body, i.e. $\phi = 0$, but it shows a general mismatch between the simulations and measurements on the front side of the body. Comparing Fig. 5.18(a) and Fig. 5.18(b), we found that increasing the antenna-body distance will alleviate the model mismatch in the front side, meaning that the effect of shape mismatch decrease. Similar observation is also found at 5 GHz in Fig. 5.19.

Also, in Fig. 5.18(b) and Fig. 5.19(b), the comparison between the single trunk scattering and the joint trunk-arm scattering shows a significant descrease of the antenna directivity by the arm scattering at the back side of the body from azimuth 120° to 240°, which are consistent with the simulation results. The results in Fig. 5.18(b) show a maximum 5 dB increase of the body shadowing in this region at 3 GHz because of the arm scattering. The maximum increase of the body shadowing at 5 GHz in Fig. 5.19(b) is 8 dB. The observations validate the analytical model on describing the on-body radiation pattern in the

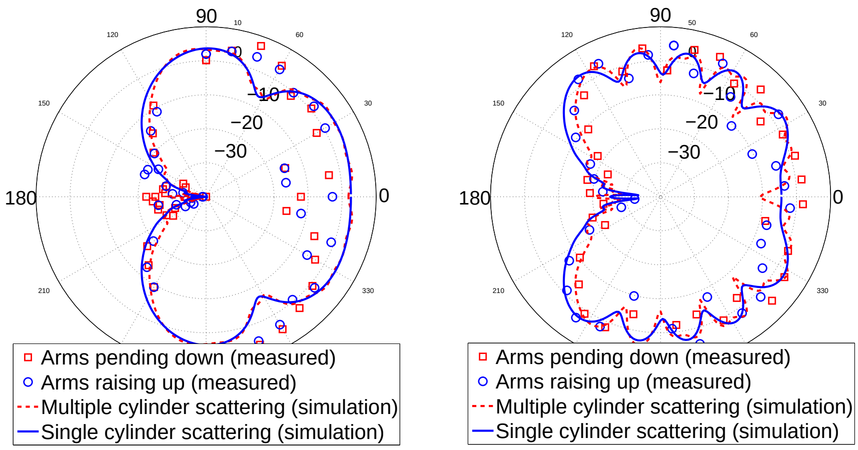

(a) (b)

Figure 5.19: Comparison of on-body antenna directivity between measurement results and simulations at 5 GHz. (a) d_s=5 cm, (b) d_s=15 cm

off-body propagation.

5.7 Conclusions

In this chapter, we have developed a dynamic closed-form analytical model of on-body channels and have validated the model in the canonical measurements. The body is modeled by multiple cylinders of infinitive length, while the antennas are modeled by polarized points. The full-wave field solution is derived regarding to the multiple cylinder scattering by point source. An efficient iterative approximation of the field solution has been proposed. The dynamic body scattering is modeled by a simple description of the arm swing during walk as investigated in the canonical measurements. By comparison between the measurements and model simulations at 2.47 GHz, the model has successfully predicted the deterministic and stochastic aspects of the dynamic fading behaviors in $\vec{z} - H$ channels. Statistical comparisons have been carried out in the $\vec{\rho}$-polarized scenarios. For the vertical on-body channels in $\vec{\rho}$ polarizaion, validation of the model is limited to propagation distances below 20 cm, owing to the infinite cylinder assumption. These comparisons show statistical consistency of the model to the measurement results. Particularly, the good predictions on the pathloss increasing rates in the scenarios confirm the assumption that the attenuation of on-body propagation on the trunk can be described on the surface of simple shapes like cylinders. The deviations on the other statistics show the geometry modeling mismatch of the body.

The results highlight the importance of a proper description of the arm motion, and the significant impact of the antenna polarization. The performance of the model is restricted by the infinite cylinder approximation, and a small scale of the arm swinging to keep the parallel motion assumption in the azimuth plane. Moreover, the antennas should be small enough to be well approximated by a point source. The model was also validated at other frequencies in [LVRDDO09, VLODD09].

The analytical model is latter applied to characterize the on-body antenna radiation pattern in off-body communications. By comparative studies between anechoic-chamber measurements and model simulations, we have evaluated the horizontal directivity of an azimuth-omnidirectional antenna placed close to the body in UWB frequencies. The analytical model has predicted close shadowing and interference effects of the body to the on-body antenna directivity observed in different directions.

Showing the valid of the model to describe the antenna radiation pattern on static body, a further extension can be made by applying the dynamic model to describe the antenna radiation pattern on moving bodies. It will then offer a statistical description of the antenna influence in dynamic scenarios, as demonstrated in [OC10].

The on-body antenna radiation pattern is an important knowledge to correctly characterize the physical off-body propagation from the measurements. It allows an independent description of the physical BAN channels compatible to different antenna systems. The model has also been applied in [VLODD09] to improve the precision of MPC estimation in on-body MIMO systems.

CHAPTER 6

Cooperative body area communication analysis

In this chapter, we analyze and evaluate simple cooperative protocols based on our on-body channel measurements in realistic environments. Using reasonable assumptions, performance of the cooperative protocols are evaluated through the capacity and diversity gains. Since on-body channels are generally uncorrelated as observed in the measurements, we focus on the effects of channel pathloss levels and fading variances to the cooperation performance.

6.1 System structure

In Ch. 3 and Ch. 4, we have presented the canonical and scenario-based on-body channel measurements conducted in a common topology formed by a single transmitter and multiple receivers. By the reciprocity theorem [R.02], such topology can correspond to either distributed Single-Input Multi-Output (SIMO) or Multi-Input Single-Output (MISO) systems. Therefore, based on the link topologies, we evaluate three simple cooperative protocols as shown in Fig. 6.1: single-relay, two-hop multi-relay, and distributed MISO.

For simplicity, we consider single antenna units at each node in the multi-links in Fig. 6.1. To limit the protocol complexity in Fig. 6.1, the design and evaluation of the protocol are based on a dual-link transmission. We then select the scenario-based 2.47 GHz dual-link on-body channel measurements presented in Sec. 4.1, as realizations of on-body channels in realistic applications.

6.2 Single-relay networks

A single-relay network consists of three nodes depicted in Fig. 6.2, the source node S, the destination node D, and the relay node R. We consider Decode-and-Forward (DF) working mode for node R, which means that node R decodes the incoming signals from node S, re-encodes and forwards it to node D. We further assume half-duplex working

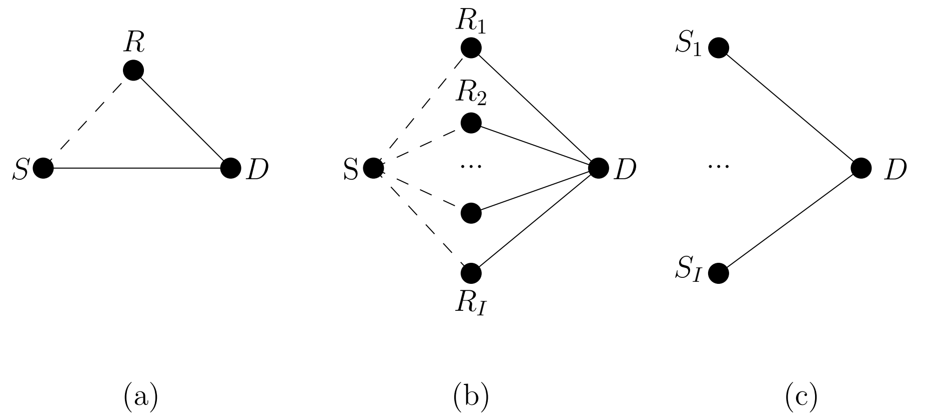

Figure 6.1: Cooperative protocols: (a) single-relay (b) two-hop multi-relay (c) distributed MISO

mode of all the nodes, i.e. they can either transmit or receive at the same time slot. There are three radio channels in the relay network: the source-relay channel h_{SR}, the source-destination channel h_{SD}, and the relay-destination channel h_{RD}. By the above configurations, we consider the relay strategy proposed by Nabar in [NBK04, dCI05] to maximize the capacity performance of the relay network. The strategy is stated as follows:

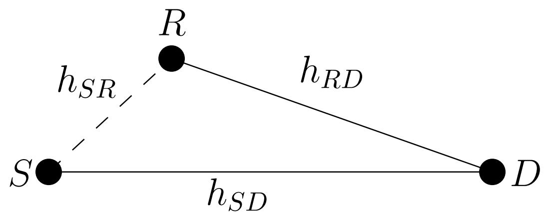

Figure 6.2: Topology of single-relay network

1. The transmission is divided into two time slots, each one having a duration of t_i. We assume equal time allocation in the two slots, therefore, $t_1 = t_2 = t$.

2. We assume that the channels in the relay network stay invariant between the two time slots.

3. In the first time slot, S transmits signal s_1 to R and D. We assume that the source-relay channel h_{SR} is good enough so that R always correctly decodes signal s_1.

4. In the second time slot, S transmits another signal s_2 to D, while R re-encodes the signal s_1 and relays it to D.

5. The total transmit power for nodes S and R should be maintained below $2E_s$ in the two time slots, where E_s is the maximum transmit power of the network. Since we presume that the gain of h_{SR} is always above h_{SD} and h_{RD}, equal power allocation is suggested to nodes S and R. By the above relay scheme, the transmit power of S and R are both $2/3E_s$.

The signal model is expressed as:

$$\begin{bmatrix} y_1 \\ y_2 \end{bmatrix} = \sqrt{\frac{2}{3}E_s} \begin{bmatrix} h_{SD} & 0 \\ h_{RD} & h_{SD} \end{bmatrix} \begin{bmatrix} s_1 \\ s_2 \end{bmatrix} + \begin{bmatrix} n_1 \\ n_2 \end{bmatrix}, \tag{6.1}$$

where y_1 and y_2 are the received signals at the first and second time slots, n_1 and n_2 are the independent and identically distributed (iid) white Gaussian noises.

We denote the effective channel as:

$$\mathbf{H} = \begin{bmatrix} h_{SD} & 0 \\ h_{RD} & h_{SD} \end{bmatrix}$$

which represents the channel matrix of the relay network. The capacity is then calculated as [NBK04]:

$$\begin{aligned} C &= \log_2 \left(\det|\mathbf{I} + \frac{2}{3}\gamma \mathbf{H}\mathbf{H}^H| \right) /2 \\ &= \sum_{i=1}^{2} \log_2(1 + \frac{2}{3}\gamma\Lambda_i)/2, \end{aligned} \tag{6.2}$$

where $\mathbf{I}$ is the identity matrix, $\det|\bullet|$ is the matrix determinant operator, Λ_i is the eigenvalues of $\mathbf{H}\mathbf{H}^H$, $\bullet^H$ being the Hermitian transpose, and γ is the transmit SNR of the network $\gamma = E_s/N_0$. The division by 2 in Eq. 6.2 is because that the relay occupies two time slots.

For a fading channel whose $\mathbf{H}$ is a random matrix, the ergodic (mean) channel capacity is computed by [CH01]:

$$C_{erg} = E[C]. \tag{6.3}$$

And the outage channel capacity is computed by [CH01]:

$$Pr(C < C_{out}) = P_{out}, \tag{6.4}$$

where P_{out} is the pre-defined outage probability, which is set to be 10% in our evaluation.

The performance of a single-relay network is evaluated by comparing it to the direct source-destination communication, i.e. in both time slots only the node S transmit signals to node D with transmit power of E_s. The capacity of direct source-destination transmission is computed by:

$$C = \log_2(1 + \gamma h_{SD}^2), \tag{6.5}$$

while the ergodic and outage capacity are computed by Eq. 6.3 and Eq. 6.4 as well, given $P_{out} = 10\%$.

The capacity is compared based on the effective receiving SNR in the direct source-destination communication, i.e. $\gamma_{\text{Rx}} = \gamma |h_{SD}|^2$.

There are four possible conditions for channels h_{SD} and h_{RD} in on-body communications.

1. **h_{SD} is inferior than h_{RD}**

   In the case where the pathloss level of h_{SD} is much lower than the pathloss level of h_{RD}, adding the relay node R will increase the end-to-end channel capacity. An example is given in Fig. 6.3(a), where the channels are selected from scenario 4, sit-stand mode. It shows that both the ergodic and outage capacity is increased at low SNRs when the relay node is added.

2. **h_{SD} is superior than h_{RD}**

   In the case where the pathloss level of h_{SD} is much higher than the pathloss level of h_{RD}, the power allocated to the relay node R will be wasted, therefore the end-to-end channel capacity decreases. We take the same example in Fig. 6.3 by exchanging the representations of h_{SD} and h_{RD}. The result is shown in Fig. 6.4

3. **h_{SD} and h_{RD} have close pathloss levels and small fading variances**

   In the case when h_{SD} and h_{RD} have close pathloss levels and small fading variances, the relaying will not bring significant improvement of the end-to-end channel capacity. The performance is then close to the direct source-destination communication. An

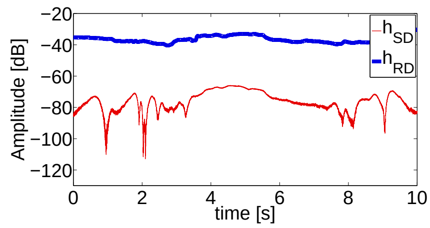

(a) channels

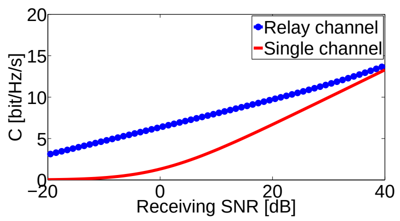

(b) Ergodic capacity

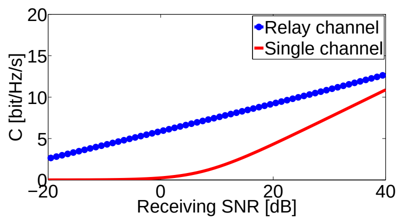

(c) Outage capacity, P_{out}=10%

Figure 6.3: Channel capacity evaluation of single-relay network when h_{SD} is inferior than h_{RD}, channels selected from dual-link measurements, scenario 4, sit-stand mode

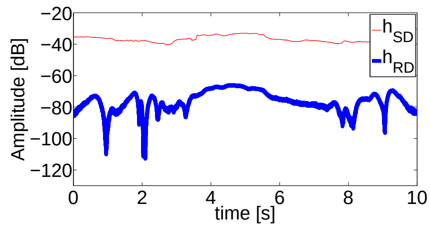

(a) channels

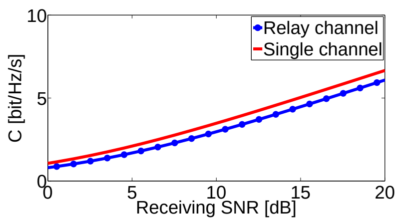

(b) Ergodic capacity

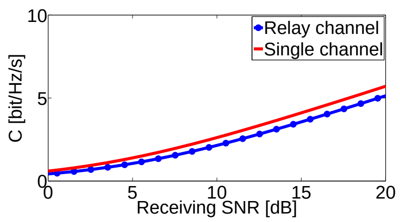

(c) Outage capacity, P_{out}=10%

Figure 6.4: Channel capacity evaluation of channel capacity in a single-relay network when h_{SD} is superior than h_{RD}, channels selected from dual-link measurement, scenario 4, sit-stand mode

example is given in Fig. 6.5, from scenario 4 in sleep mode. The selected channels show flat fading over time, hence the relay will not improve neither the ergodic nor outage capacity.

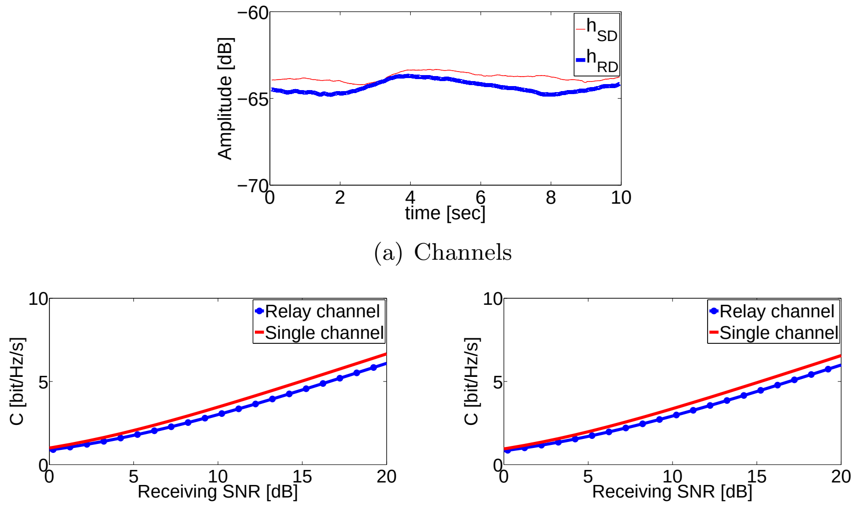

(a) Channels

(b) Ergodic capacity

(c) Outage capacity, P_{out}=10%

Figure 6.5: Channel capacity evaluation of a single-relay network when h_{SD} and h_{RD} have close pathloss levels and small fading variances, channels selected from dual-link scenario 4, sleep mode

4. **h_{SD} and h_{RD} have close pathloss levels and large fading variances**

   In the case when h_{SD} and h_{RD} have close pathloss levels and large fading variances, the cooperation between the source and the relay nodes will mitigate the end-to-end fading effect. Since h_{SD} and h_{RD} have close pathloss levels, the ergodic channel capacity will not get improved. However, the mitigation on the end-to-end fading variance will increase the outage channel capacity at small SNR. An example is given in Fig. 6.6(a), from scenario 2 in walk mode. Because of the channel fading, the outage capacity is generally worse than the outage capacity in the flat channels as in Fig. 6.5. The comparison in Fig. 6.6(c) shows an improvement of the end-to-end outage capacity at small SNR in the relay channel. This shows that the uncorrelation and significant fading variances of h_{SD} and h_{RD} are the two prerequisites to increase the outage channel capacity by cooperative relaying.

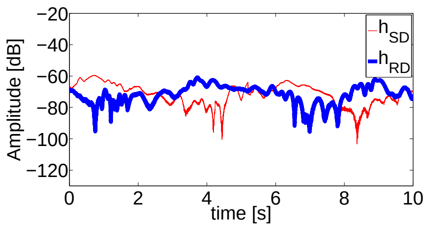

(a) channels

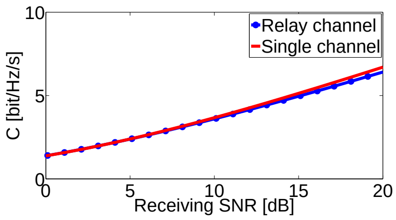

(b) Ergodic capacity

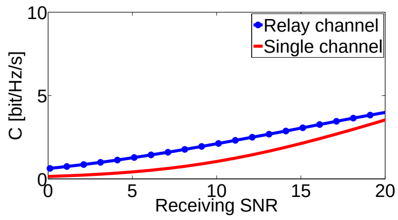

(c) Outage capacity, P_{out}=10%

Figure 6.6: Channel capacity evaluation of single-relay network when h_{SD} and h_{RD} have close pathloss levels and large fading variances, channels selected from dual-link measurements, scenario 2, walk mode

6.3 Two-hop multi-relay network

A two-hop multi-relay network is composed of one source node S, one destination node D, and multiple relay nodes R_i as illustrated in Fig. 6.3. Regarding the dual-link measurements, we consider only two relay nodes in the topology. Similarly to single-relay network, we assume DF relay nodes and half-duplex working modes in all nodes. To simplify the evaluation of multi-relay cooperation, we consider a simple opportunistic relaying strategy by [BKRL06] as described in the following:

1. The relay uses two time slots with equal duration of t
2. In the first time slot, the source node S transmits signal s to all relay nodes R_i. We assume all source-relay channels are good enough so that the relay nodes always correctly decode the signal. We further assume that the source-destination channel has a high pathloss levels so that the destination node D fails to receive the signal during the first time slot. The destination node D then broadcasts a certain message that all the relay nodes listen and estimate the Channel State Information (CSI) of their relay-

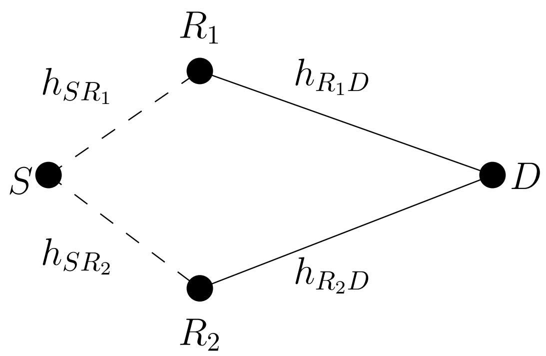

Figure 6.7: Topology of two-hop multi-relay network

destination channels h_{R_iD}.

3. In the second time slot, the relay nodes weight quality of their own relay-destination channels. The one with the largest channel gain re-encodes the signal and transmit to the destination node first, while the rest waits following the principles in [BKRL06].

The principle of opportunistic relaying is to try to transmit the signal on the best relay-destination channels. We ignore the cost on the listening and coordination among the nodes, therefore the effective relay channel is defined as:

$$h_{RD,opt} = \max\{h_{R_iD}\} \tag{6.6}$$

The channel capacity of the opportunistic multi-relay network is expressed as:

$$C = \min\{C_{SR}, C_{RD,opt}\}/2, \tag{6.7}$$

which means that the end-to-end capacity in a two-hop relay is bounded by the smallest channel capacity of the hops. The division 2 is again due to the reason that the strategy occupies two time slots. The capacity in each hop is calculated by Eq. 6.5.

By assuming that the source-relay channel is always better than the relay-destination channels, Eq. 6.8 is given as:

$$C = C_{RD,opt}/2, \tag{6.8}$$

The performance of opportunistic multi-relaying is compared with single relay, where the capacity in a single relay-destination link is computed as:

$$C = \log_2(1 + \gamma h^2_{R_{1/2}D})/2. \tag{6.9}$$

The ergodic and outage capacities over fading channels follow Eq. 6.3 and Eq. 6.4, given $P_{out} = 10\%$.

We consider three conditions of h_{R_1D} and h_{R_2D}:

1. **h_{R_1D} and h_{R_2D} have different pathloss levels**

   In this case, by Eq. 6.6, the opportunistic relaying will always select the one lower pathloss level to transmit the signal, which turns the transmission into two-hop single relaying.

2. **h_{R_1D} and h_{R_2D} have close pathloss levels and small fading variances**

   When h_{R_1D} and h_{R_2D} have close pathloss levels but flat fading, the opportunistic relaying will not bring to any gains on the channel capacity. Instead, extra cost on the coordination between the relay nodes is wasted.

3. **h_{R_1D} and h_{R_2D} have close pathloss levels and large fading variances**

   In this case, the effective relay channel by Eq. 6.6 will have better link quality than h_1 and h_2. An example is selected from scenario 2, walk mode as in Fig. 6.6. The capacities of the opportunistic relaying are compared with the capacities of the single-relay based on the receiving SNR in the single relay-destination channels. The results in Fig. 6.8(b) and Fig. 6.8(c) show that the opportunistic relaying raises the channel gain and decreases the effective fading variance, which in return increases the end-to-end channel ergodic and outage capacities.

6.4 Distributed dual-link MISO

Cooperative multi-link communication is an effective technique to mitigate the significant dynamic on-body fading as studied in [GGV$^+$09, CTea09]. Similarly to collocated MIMO systems, the spatial diversity in a distributed MIMO system can be achieved through the Space Time Block Coding (STBC). In this section, we consider a distributed dual-link MISO configuration as in Fig. 6.4, which consists of two source

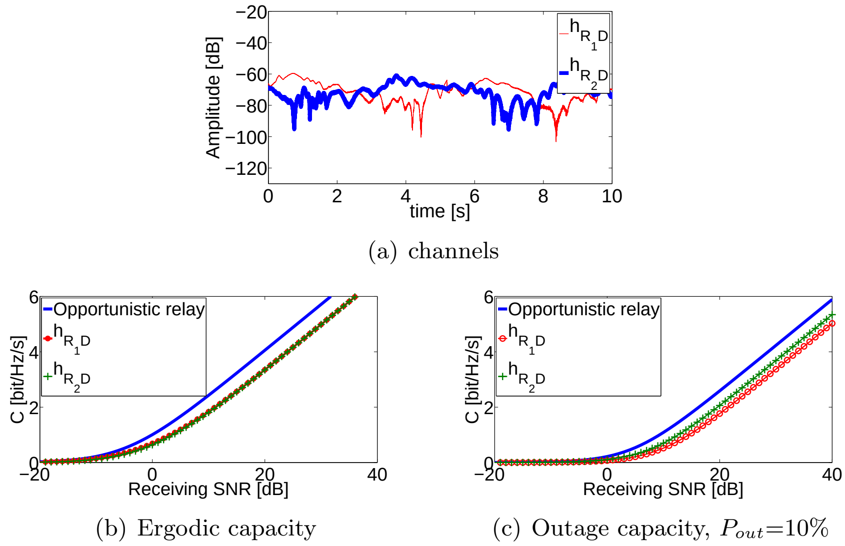

Figure 6.8: Channel capacity evaluation of opportunistic multi-relay network when h_{SD} and h_{RD} have close pathloss levels and large fading variance, channels selected from dual-link measurements, scenario 2, walk mode

nodes S_1, S_2, and one destination node D. We apply the Alamouti code as described in [Ala98]. The cooperation scheme is described as follows:

1. The Alamouti coding for a 2×1 MISO consists of two time slots (t_1, t_2) with equal duration. We assume that the channels between the source and the destination nodes are invariant during the two time slots.

2. The coding matrix is expressed in Table 6.1:

	t_1	t_2
S_1	s_1	$-s_2^*$
S_2	s_2	s_1^*

Table 6.1: Alamouti code in 2×1 MISO

3. By [Ala98], the estimation of the received s_1 and s_2 is expressed

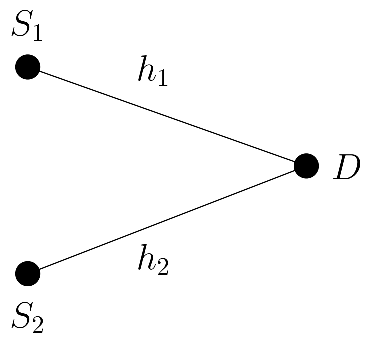

Figure 6.9: Topology of distributed dual-link MISO

as:

$$\hat{s}_1 = (|h_1|^2 + |h_2|^2)\sqrt{E_{s1}}s_1 + h_1^* n_1 + h_2 n_2^*$$
$$\hat{s}_2 = (|h_1|^2 + |h_2|^2)\sqrt{E_{s2}}s_2 - h_1 n_2^* + h_2^* n_1 \qquad (6.10)$$

where E_{s1} and E_{s2} are the transmit power of the signals. We consider an equal-power allocation scheme, which is realistic for most power-limited sensor communications.

The diversity gain of the dual-link MISO is compared with the diversity gain of single link on-body communication. By [CH01], we define the diversity gain as:

$$g_{\text{div}} = \lim_{\gamma \to \infty} \frac{\log(err_{\text{MISO}})}{\log(err_{\text{SISO}})} \qquad (6.11)$$

where err_{MISO} and err_{SISO} are the Bit Error Rate (BER) of the MISO and Single-Input Single-Output (SISO) system when the SNR is sufficiently high.

The BER of Alamouti STBC is synthesized through Monte-Carlo simulations. We consider a Quadrature Phase Shift Keying (QPSK) modulation scheme as adopted in the ZigBee standard. The BER achieved in the dual-link is compared with the BER achieved in the single-links, which is based on the effective receiving SNR in channel h_1. The evaluation is made in three different link conditions.

1. **h_1 and h_2 have different pathloss levels**

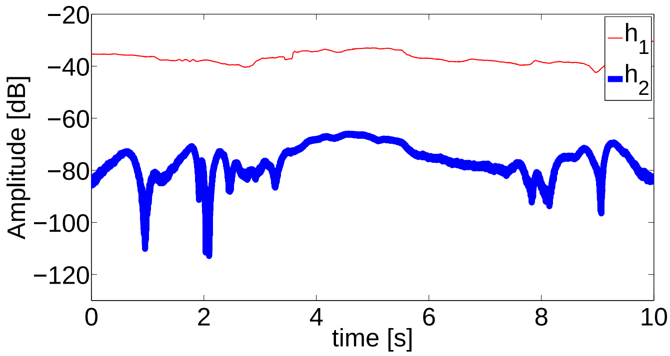

(a) channels

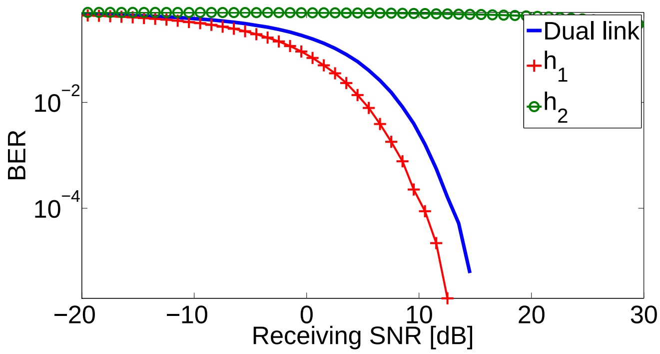

(b) BER comparison

Figure 6.10: BER comparison of Alamouti coding in dual-links with different pathloss levels, channels selected from dual-link measurements scenario 1, sit-stand mode

In this case, allocating equal power to each link will actually waste 50% of the power on the link with higher pathloss level. Consequently, the diversity gain by the Alamouti coding is -3 dB compared with the single link. One example is given in Fig. 6.10, which clearly shows a deterioration of the BER in the dual-link communication.

2. **h_1 and h_2 have close pathloss levels and small fading variances**

   Similarly to previous discussion on opportunistic relaying, cooperation between links having close pathloss levels and small fading variances will not bring significant BER improvement. One exam-

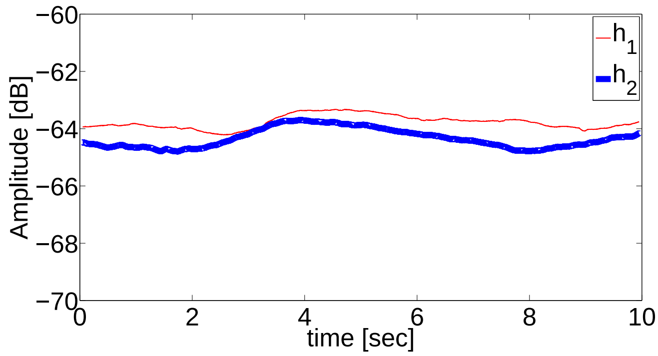

(a) channels

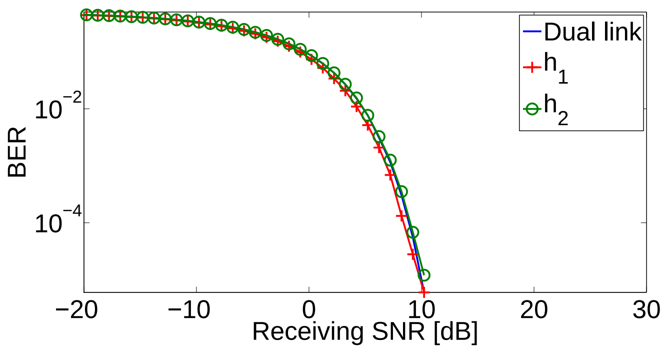

(b) BER comparison

Figure 6.11: BER comparison of Alamouti coding in dual-link with close pathloss levels and small fading variance, channels selected from dual-link measurement, scenario 4, sleep mode

ple is given in Fig. 6.11, where the BER in the dual-link is close to the BER in each single link.

3. **h_1 and h_2 have close pathloss levels and large fading variances**

   Cooperation between links having close pathloss levels and large fading variances can achieve significant spatial diversity. An example is given in Fig. 6.12, where a significant improvement of the BER in cooperative dual-link is observed. The Alamouti code then brings a typical diversity gain of 2 (3 dB) to the communication. In addition to equal power allocation, we also investigate an opportunistic power allocation scheme by the principles similar to

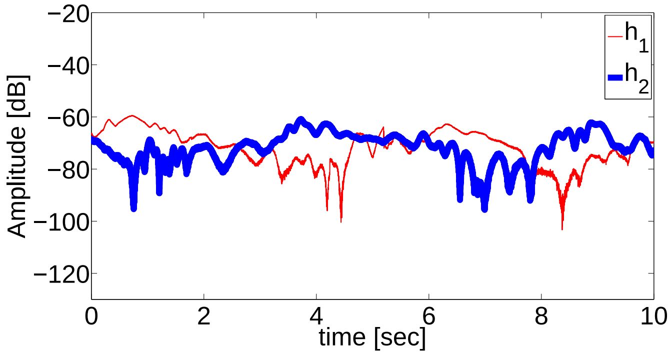

(a) channels

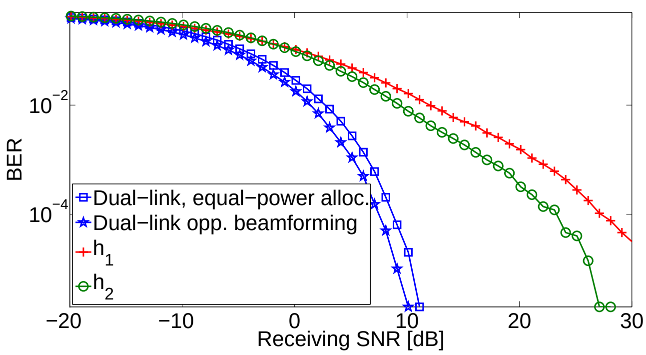

(b) BER comparison

Figure 6.12: BER comparison of Alamouti coding in dual-links with close pathloss levels and large fading variance, channels selected from dual-link measurements, scenario 2, walk mode

the opportunistic relaying in Sec. 6.3. As explained in Sec. 6.3, opportunistic power allocation scheme actually raises the effective receiving SNR, thereby a slight improvement of the BER is made, as also shown in the figure.

6.5 Conclusions

The channels play an important role to determine the on-body link quality at low SNRs. Using cooperative protocols in BAN can mitigate the fading effect and enhance the link connection due to the spatial diversity of the on-body channels. Particularly, when on-body multi-link channels have close pathloss levels and large fading variances, both the relaying and multi-link cooperation significantly improve the system end-to-end capacity and/or diversity gains. Simple cooperative protocols in low SNR are sensitive to the channel conditions. In realistic applications, large fluctuation of the on-body channels can happen during changes of postures and motions. This implies that simple cooperative protocols will not always work properly due to the failure of predicting the channel states.

Part II

Cooperative channels in cellular mobile networks

CHAPTER 7
Introduction to MIMO channel modeling

7.1 MIMO channel modeling

Reference channel modeling is an important framework in the design and evaluation of MIMO systems. As new wireless applications are becoming more and more complex, the needs for a more accurate channel modeling are increasing accordingly. For instance, in the planning of conventional GSM networks, simple path loss models were sufficient for sensible coverage prediction, whereas nowadays, the channel models needed in the development of MIMO systems have to represent the signal dispersion in the angular, delay, and Doppler domain simultaneously. Moreover, the emergence of distributed MIMO, multi-user MIMO, and cooperative techniques in the developments for future communication systems, also calls for a more advanced channel modeling across multiple links.

MIMO channels are modeled by numerous methods. Deterministic channels models use sophisticated simulations such as FDTD and ray-tracing to describe the exact radio propagation given a deterministic environment. Statistical channels describe the channel statistics in different domains by a limited number of parameters.

Modeling the channel statistics is therefore more efficient and realistic to cover the variety of the environments. In this respect, there are two major statistical modeling approaches. On the one hand, analytical (non-physical) models characterize the MIMO channel matrix, by mathematical descriptions. Examples include the 802.11n tapped angular-delay line model, the correlation-based Kronecker model, as well as the eigenspace-based Weichselberger model [CH01]. On the other hand, physical models characterize the physical scatterers by their delay, DoD, DoA, and complex path weight for different polarizations. Physical models are antenna-independent and can be directly combined with antenna array responses to synthesize the MIMO channel matrix. Among physical modeling approaches, the Geometry-based Stochastic Channel Models (GSCMs) constitute a group of advanced MIMO channel models which further characterize the properties of the scatterers through an explicit geometry description of the scatterers.

The COST 2100 MIMO channel model is a GSCM that has been built upon the framework of the earlier COST 207, COST 231, COST 259, and COST 273 models [Cor06]. The COST 207 and COST 231 channel models [Cor99] were successfully applied to GSM and UMTS networks, respectively. The COST 259 channel model [MAH+06, AGM+06] was the first GSCM considering multi-antenna base stations, and full MIMO systems were targeted by the COST 273 model. The COST 2100 channel model extends the COST 273 model to cover MIMO systems at large, including multi-user, multi-cell and cooperative aspects, and this, without requiring a fundamental shift in the original modeling philosophy.

7.2 GSCM methods

The principle of GSCMs is to model the wireless channel by statistically describing scattering from interacting objects (or scatterers) in a simulation environment. The stochastic properties of the wireless channel, with respect to the delay and double-directional domains, are described by the geometric distribution of the scatterers. Some of the widely known GSCMs include the 3GPP Spatial Channel Model (SCM) [3GP03], the WINNER II model [ea07], and the COST family of channel models.

The overall channel results from the superposition of many different MPCs. The scattering mechanisms may consist of a single interaction, i.e. with one object (single-bounce), or of a number of consecutive interactions with multiple objects (multiple-bounce). In addition, most GSCMs adopt a double-directional channel description, where the MPCs generated by either of the two scattering mechanisms are represented in three domains (delay, DoD, and DoA) through a geometric description. Finally, in an effort to reduce the number of model parameters, MPC with similar delays and directions are sometimes grouped into so-called clusters.

An important criterion to evaluate the performance of GSCMs is that the synthesized Large Scale Parameters (LSPs) from the models, such as the shadowing or the global delay and angular spreads, are statistically reliable and consistent with experimental observations. There are two main approaches for GSCMs, a system-level approach and a cluster-level based approach.

7.2.1 System-level GSCMs

The 802.11 3GPP SCM and WINNER II models [3GP03, ea07] are typical system-level based GSCMs. In these two models, the propagation environment is specified for each realization of all radio links between the Base Stations (BSs) and the Mobile Stations (MSs). In a given realization, the model first fixes the LSPs following specified distributions, and then generates a geometric distribution of MPCs accordingly. The advantage of system-level based GSCMs is that the LSP statistics in a specific scenario are always guaranteed in each realization of the model. However, the independent initialization of the propagation environment in each of these realizations prohibits connecting different realizations with intervals larger than the auto-correlation distance, hence hampering the simulation of larger motions of the MSs. Also, forcing the consistency of LSPs with measured properties at system level makes the model quite rigid. Typically, when the analysis requires to add new LSPs, such as the channel correlation in multi-link communication scenarios, the entire initialization of the propagation environment must be re-defined, hindering a straightforward extension of the model.

7.2.2 Cluster-level GSCMs

Cluster-level based GSCMs, such as the COST 2100 model, are designed in an alternative way. In cluster-level based models it is assumed that the LSP statistics in an environment can be attained if the clusters in the environment are characterized with adequate statistics, both in geometry and in physics. This allows for a single initialization of the propagation environment, which is independent of the MS locations and the channel instances. While naturally accounting for a movement of the MS, a cluster-level based structure is more flexible as it enables to include new LSPs (e.g. correlation properties of multi-link channels) with less modifications. Obviously, a cluster-level based GSCM can result in a larger deviation with respect to the LSPs statistics than the system-level based GSCMs in a single realization, but the average LSP statistics can typically be consistent with measurements.

7.3 Multi-link MIMO channel modeling

Multi-link MIMO channel modeling are advanced spatial MIMO channel description in cooperative multi-link communications. The conventional

GSCMs are developed in a BS-centric framework. This means that the propagation environment is modeled with respect to a single BS, which can not cover the inter-cell properties like spatial channel correlation. To describe multi-link MIMO channels, the BS-centric framework should be converted as environment-centric to cover multiple BSs. As stated, introducing the inter-link properties to system-level based GSCMs will likely change their fundamental structures. For cluster-level based GSCMs, the multi-link extension can be realized on the clusters. The multi-link LSPs will be then synthesized.

Note that for both kinds of GSCMs, a multi-link extension means more complex channel modeling and estimation, as well as extensive measurements for validation and parameterization of the models.

CHAPTER 8

Single-link COST 2100 channel model

The single-link COST 2100 MIMO channel model inherits most of the concepts from the COST 273 model. This chapter presents the structure and essential concepts of the COST 2100 model with concrete interpretation and parameterization methods. Two advanced single-link parameters, the polarization and Dense Multipath Component (DMC), are introduced at the end of this chapter.

8.1 General image of single-link COST 2100 model

The single-link COST 2100 model describes the radio channel between a single static multi-antenna BS and a single multi-antenna MS. The channel consists of a number of MPCs described in delay-angular domains, i.e. by their delay, Azimuth-of-Departure (AoD), Elevation-of-Departure (EoD), Azimuth-of-Arrival (AoA), and Elevation-of-Arrival (EoA). The MPCs result from interactions between the signal waves and the specular scatterers distributed in the environment. In most cases, MPCs are mapped to scatterers with explicit geometric relationships. The clusters are obtained by grouping the scatterers that generate MPCs in similar delays and angles. The clusters describe the common properties of MPCs resulting from a common object like the walls, buildings, etc. This clustering of MPCs largely reduces the number of parameters to describe the channel.

Fig. 8.1 describes the general structure of the COST 2100 model. There are three different clusters in the model.

- **Local clusters** are located around MS or BS, describing a single interaction of the signal waves with the local scatterers at MS or BS.
- **Far/remote clusters** are located remotely throughout the environment. Far clusters are further divided into two kinds:
  - **Single-bounce clusters** describe the single interactions between the signal waves and the remote environment.

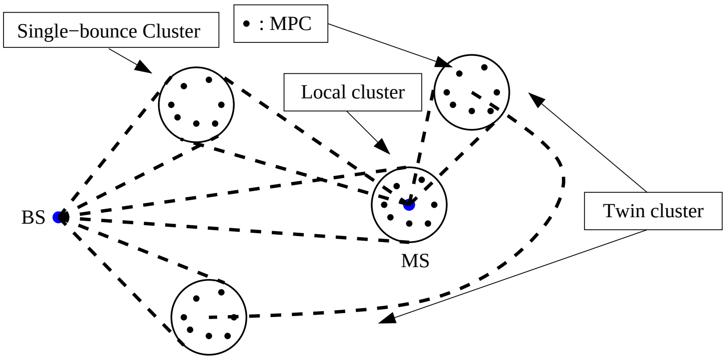

Figure 8.1: General structure of COST 2100 MIMO channel model: the model contains three kinds of clusters, i.e. local clusters, single-bounce clusters and twin clusters.

– **Multiple-bounce clusters** describe the multiple interactions between the signal waves and the remote environment.

By the COST 2100 model, the ratio of the number of multiple-bounce clusters to the number of single-bounce clusters in the environment is controlled by the selection factor, denoted as K_{sel}.

In geometry, local clusters and single-bounce clusters are composed of single-interaction MPCs, therefore they can be explicitly described by a single representation at one position in the environment by matching the delay, DoD, and DoA jointly, as in Fig. 8.1. On the contrary, the MPCs in a multiple-bounce cluster undergo multiple interactions with the scatterers, therefore the delay, DoD, and DoA cannot be matched with a single geometric representation. Instead, a multiple-bounce cluster is described by two representations as viewed from the MS and from the BS. A multiple-bounce cluster is also called a *twin cluster*, because it is described by two identical representations viewed from the BS and MS to guarantee the consistency of its statistics, as shown in Fig. 8.1. This is a straightforward extension of the double-directional radio channel to clusters.

Given the spatial distribution of the remote clusters, the LSPs of a MS-BS link are controlled by the number of clusters that contribute to the link, which follows a Poisson distribution. To maintain the statistical consistency of the LSPs when the MS is located at different positions, the occurrence (or visibility) of a remote cluster to the MS-BS link has to be limited. The model uses the concept of Visibility

Region (VR) [MAH+06, Cor06] from the COST 273 model to restrict the area where a remote cluster is visible to the BS. Hence, the MS in a certain position will only receive a limited number of MPCs from the visible remote clusters. In this sense, local clusters are either visible or invisible throughout the simulation area determined by the specific environment.

By introducing the concept of cluster visibility, the COST 2100 model calculates the time-varying CIR in delay-angular domains as:

$$h(t,\tau,\boldsymbol{\Omega}^{\mathrm{BS}},\boldsymbol{\Omega}^{\mathrm{MS}}) = \sum_{n\in\mathscr{C}}\sum_{p=1}^{P} a_{n,p}(t,\tau_{n,p},\boldsymbol{\Omega}_{n,p}^{\mathrm{BS}},\boldsymbol{\Omega}_{n,p}^{\mathrm{MS}})\delta(\tau-\tau_{n,p})\delta(\boldsymbol{\Omega}^{\mathrm{BS}}-\boldsymbol{\Omega}_{n,p}^{\mathrm{BS}})\delta(\boldsymbol{\Omega}^{\mathrm{MS}}-\boldsymbol{\Omega}_{n,p}^{\mathrm{MS}}), \quad (8.1)$$

where $\mathscr{C}$ is the set of visible clusters depending on the position of MS, $a_{n,p}$ is the complex MPC in the nth visible cluster, P is total number of the MPC in a cluster, t is the time, τ is the delay, $\boldsymbol{\Omega}^{\mathrm{BS}}$ is the DoD including the AoD and EoD, $\boldsymbol{\Omega}^{\mathrm{MS}}$ is the DoA including the AoA and EoA, and δ is the Dirac function.

For a MIMO system using V and U multiple antennas arrays at BS and MS, we may express the $U\times V$ MIMO channel matrix $\mathrm{H}(t,\tau)$, under the plane wave and balanced narrowband array assumptions, as:

$$\begin{aligned}\mathrm{H}(t,\tau) &= \int\int h(t,\tau_n,\boldsymbol{\Omega}^{\mathrm{BS}},\boldsymbol{\Omega}^{\mathrm{MS}})\boldsymbol{s}_{\mathrm{BS}}(\boldsymbol{\Omega}^{\mathrm{BS}})\boldsymbol{s}_{\mathrm{MS}}(\boldsymbol{\Omega}^{\mathrm{MS}})d\boldsymbol{\Omega}^{\mathrm{BS}}d\boldsymbol{\Omega}^{\mathrm{MS}}\\ &= \sum_{n\in\mathscr{C}}\sum_{p=1}^{P} a_{n,p}(t,\tau_n,\boldsymbol{\Omega}_{n,p}^{\mathrm{BS}},\boldsymbol{\Omega}_{n,p}^{\mathrm{MS}})\boldsymbol{s}_{\mathrm{BS}}(\boldsymbol{\Omega}_{n,p}^{\mathrm{BS}})\boldsymbol{s}_{\mathrm{MS}}(\boldsymbol{\Omega}_{n,p}^{\mathrm{MS}})\delta(\tau-\tau_{n,p})\end{aligned} \quad (8.2)$$

where $\boldsymbol{s}_{\mathrm{BS}}(\boldsymbol{\Omega}_{n,p}^{\mathrm{BS}})$ and $\boldsymbol{s}_{\mathrm{MS}}(\boldsymbol{\Omega}_{n,p}^{\mathrm{MS}})$ are the antenna array steering vectors at BS and MS sides [PG03, OC07].

8.2 Essential modeling concepts and their interpretation

The essential modeling concepts of the COST channel model have been introduced and generally described in [Cor06]. This section clarifies and proposes concrete interpretation, parameterization, and implementation of the concepts.

8.2.1 Visibility region

A VR is a circular area with a fixed radius. It determines the visibility gain of only one cluster, denoted as A_{VR}. The visibility gain of the cluster in the link smoothly increases when the MS is approaching the center of the related VR, expressed as:

$$A_{\mathrm{VR}}(d) = \frac{1}{2} - \frac{1}{\pi} \arctan\left(\frac{2\sqrt{2}(L_C + d)}{\sqrt{\lambda L_C}} \right), \tag{8.3}$$

where d is the distance between the MS and the VR center, R_C is the radius of the VR, L_C is the width of the transit region in the VR. Fig. 8.2(a) depicts the A_{VR} in the macrocell environment. The change of the cluster visibility based on the MS-VR distance, is an important feature of the COST 2100 model to describe the time-variation of the channels by updating the cluster visibility as a result of the MS movement.

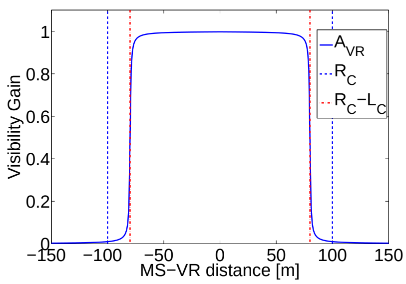

(a) A_{VR}

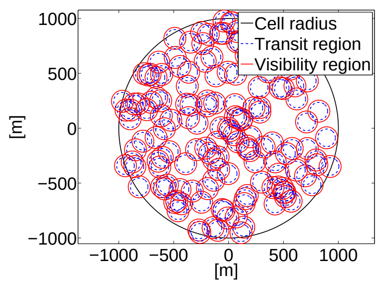

(b) Uniform distribution of VR

Figure 8.2: Modeling example of VR in macrocell by COST 2100 model

The VRs are uniformly distributed in the simulation area, as illustrated in Fig. 8.2(b). The density of the VRs, denoted as ρ_C, should corresponds to the average number of visible remote clusters, given the relationship:

$$\rho_C = \frac{N_C}{\pi(R_C - L_C)^2} \left[m^{-2} \right], \tag{8.4}$$

where N_C is the average number of remote clusters, following a Poisson distribution.

The overlapping of different VRs allow the MS to receive multiple remote clusters when it is in the overlapped region.

8.2.2 Cluster

A cluster is formed by the grouping of MPCs with certain spatial spread to correspond to the delay and angle spreads in the channel. A cluster is modeled as an ellipsoid in space as described in Fig. 8.2.2. The axes of the clusters along different directions, correspond to the maximum cluster delay spread (CDS), denoted as δ_C, and the cluster angular spread (CAS), denoted as $\phi_{C,BS}$ and $\phi_{C,MS}$ in the azimuth plane, and as $\theta_{C,BS}$ and $\theta_{C,MS}$ in the elevation plane. In general, the position and spread of the cluster are specified at both the BS and MS sides. For local and single-bounce clusters, such specification is identical at both sides since they only need one representation in space. For twin clusters, the specification should be treated respectively at both sides. Before detailing the characteristics of clusters, we introduce the following notations related to the quantities used in Fig.8.2.2.

1. Δ_C, $\phi_{C,BS}$, $\phi_{C,MS}$, $\theta_{C,BS}$, and $\theta_{C,MS}$ are the delay, AoD, AoA, EoD, and EoA spreads of the cluster.
2. a_C, b_C, and h_C are the corresponding extents of the cluster in space that lead to the delay, azimuth spreads (AoD and AoA), and elevation spreads (EoD and EoA) of the cluster.
3. $d_{C,BS}$ and $d_{C,MS}$ are the cluster-BS and cluster-MS distances.

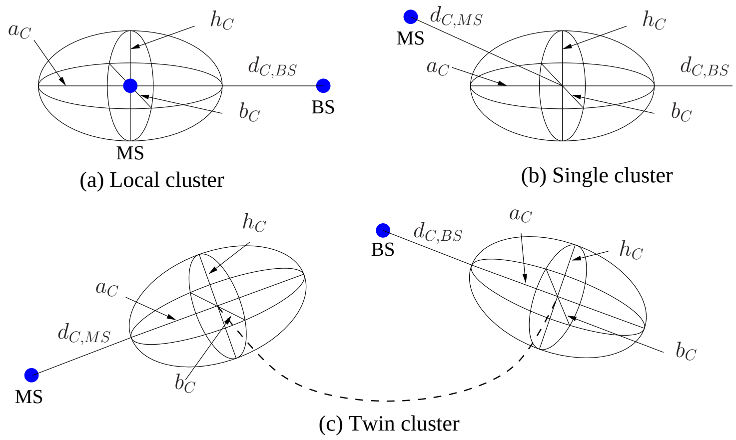

Figure 8.3: Modeling of three different kinds of clusters in COST 2100 model

8.2.2.1 Local cluster

Local clusters contain only single-bounce MPCs and have uniform spread in azimuth. Therefore the spatial spreads of the clusters are only determined by their delay spreads and elevation spreads with the following geometry relationship [Cor06]:

$$a_C = \frac{1}{2}\Delta_C c_0, \quad b_C = a_C, \quad h_C = d_{C,BS} \tan\theta_{C,BS}, \tag{8.5}$$

where c_0 is the free-space wave speed.

In the COST 2100 model, we determine the angular spreads of both MS-local and BS-local clusters from the BS side.

8.2.2.2 Single-bounce cluster

A single-bounce cluster has independent delay and azimuth spreads. Consequently, it is depicted as an ellipsoid rotated toward the BS, so that its spatial spread adequately fits the delay and angular spreads along different axes as viewed from the BS. The geometry relation is expressed as:

$$a_C = \frac{1}{2}\Delta_C c_0, \quad b_C = d_{C,BS} \tan\phi_{C,BS}, \quad h_C = d_{C,BS} \tan\theta_{C,BS}, \tag{8.6}$$

A single-bounce cluster is always distributed relative to the BS and its VR as shown in Fig. 8.2.2.2. The position of a single-bounce cluster is determined by a random vector drawn from the BS. The length of this random vector follows certain non-negative distribution, e.g. exponential distribution in macrocell, floored by a minimum distance r_{min}. The vector is rotated by a random angle $\Psi_{C,BS}$ relative to the imaginary line between the BS and the VR center. $\Psi_{C,BS}$ is modeled as following a normal distribution, i.e. $\Psi_C \sim \mathcal{N}(\mu_{\Psi_C}, \sigma_{\Psi_C})$.

8.2.2.3 Twin cluster

The COST 273 model describes very generally a twin cluster as two identical ellipsoids at BS and MS sides. The detailed modeling principles of twin clusters are missing in COST 273 model. For the implementation of COST 2100 model, we specify two important parameters of the twin cluster: the cluster distribution at both sides and the cluster delay mismatch.

Since a far cluster is visible only when the MS is inside its VR, the two ellipsoids of a twin cluster are defined to be rotated toward the

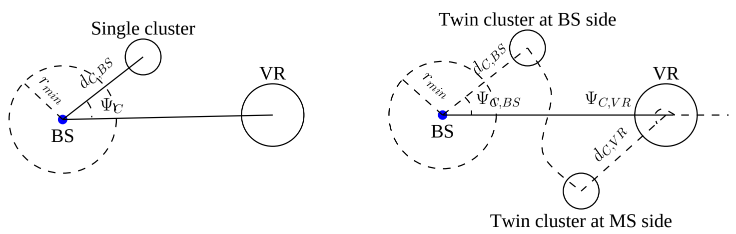

Figure 8.4: Distribution of single-bounce clusters and twin clusters in COST 2100 model

BS and the VR center respectively. This guarantees that when MS is inside the VR of a twin cluster, the cluster's delay and angular spreads is generally matched at both sides.

To determine the position of a twin cluster, the method applied to the single-bounce cluster is performed twice: first by a random vector from the BS, then by another random vector from the VR center, as depicted in Fig. 8.2.2.2. Both random vectors are modeled in the same way as in single-bounce cluster distribution. The distance between the cluster at MS side and the VR should be computed through:

$$d_{C,BS} \tan \phi_{C,BS} = d_{C,VR} \tan \phi_{C,MS}, \tag{8.7}$$

in order to match the angular spreads viewed from BS and MS sides.

To compensate for the mismatch between the delay and the angles of a twin cluster, an extra cluster link-delay, $\tau_{C,link}$ is introduced in the COST 273 model [Cor06]. The $\tau_{C,link}$ describes the multiple bounce process inside a twin cluster. In COST 2100 model, the cluster link-delay is implemented by a non-negative random variable with a minimum delay when single bounce between the centers of the twin cluster occurs. Local and single-bounce clusters are then treated as special twin clusters where $\tau_{C,link} = 0$. Therefore, the total delay of a cluster is determined by:

$$\tau_C = (d_{C,BS} + d_{C,MS})/c_0 + \tau_{C,link}. \tag{8.8}$$

The cluster-link delay is a large-scale property that is applied to all the MPCs belonging to the corresponding cluster.

8.2.2.4 Cluster parameterization

A cluster describes LSPs of the grouped MPCs, including the position, delay spread, angular spread, visibility gain, cluster-link delay, shadowing, and the cluster power attenuation. The shadowing of the cluster is a random variable following Guassian distribution in dB, i.e. $SF \sim \mathcal{N}(0, \sigma_{SF_C})$. The delay spread, angular spread, and the shadowing of a cluster are correlated random variables. The actual correlation coefficient matrix of them depends on the scenarios, some of which are tabulated in [Cor06].

The cluster power attenuation, denoted as A_C, is the relative attenuation to the pathloss. A_C is assumed to exponentially decay when the difference between the cluster delay τ_C and the LOS delay τ_0 increases:

$$A_C = \max(\exp[-k_\tau(\tau_C - \tau_0)], \exp[-k_\tau(\tau_B - \tau_0)]), \tag{8.9}$$

where k_τ is the decaying factor, and τ_B is the cut-off delay to avoid an extremely low cluster power in the channel.

8.2.3 Line-Of-Sight

A LOS is the direct propagation path between the MS and BS. The COST 2100 model represents LOS as a special cluster containing a single MPC. The VR of the LOS is modeled by its own size and is confined within a cut-off distance from the BS. The power of the LOS is determined by a Lognormal distributed power factor ζ over the sum of the power from the other visible clusters [Cor06] as:

$$A_{LOS} = \frac{1}{\sqrt{L}} \zeta \sum_{n \in \mathscr{C}} A_{n,VR} A_{n,C} e^{-j\pi d_{MS,BS} f_c}, \tag{8.10}$$

where L is the pathloss calculated based on the MS-BS distance $d_{MS,BS}$, and f_c is the carrier frequency.

8.2.4 Multi-Path Components

For modeling simplicity, the COST 2100 model assumes an identical number of MPC in both local clusters and far clusters. The scatterers constituting a remote cluster have a Gaussian distribution in space (angle) within the cluster, whereas the local scatterers are uniformly distributed within the local cluster. Scatterers in a twin cluster have identical local distributions in space in the clusters at BS and MS sides to maintain a consistent spatial spread from both sides. Each scatterer results in one MPC, whose delay and angles are calculated geometrically.

Finally, the delay of the pth MPC in the nth visible cluster is calculated by:

$$\tau_{n,p} = (d_{MPC_{n,p},BS} + d_{MPC_{n,p},MS})/c_0 + \tau_{n,C,link}, \tag{8.11}$$

where $d_{MPC_{n,p},BS}$ and $d_{MPC_{n,p},MS}$ are the actual distances from the MPC to the BS and MS, which are calculated according to the instant positions of the BS and MS.

Accounting for the large-scale parameters from the clusters and the small-scale parameters from the MPCs, the complex amplitude of a MPC is finally expressed as:

$$a_{n,p} = \frac{1}{\sqrt{L}} A_{VR,n} A_{MPC,n,p} \sqrt{SF_n A_{C,n}} e^{-2j\pi\tau_{n,p}f_c}, \tag{8.12}$$

where $A_{MPC,n,p}$ is the complex fading of the MPC.

8.2.5 Time evolution

The COST 2100 model describes the propagation environment by a single realization as long as the environment remains static. The VRs and the clusters are then generated independent by the position of the MS. Under this assumption, all MPCs, except the ones in the local cluster at MS side, maintain flat fading and deterministic positions throughout one simulation instance. The time-variation of a channel is therefore formed by the movements of the MS when it enters and leaves different VRs. The first consequence by the MS movement is the visibility changes of far clusters, resulting the lifetimes of far clusters in the link. The movement of MS also changes the delay, DoD, and attenuation of the remote clusters, which should be re-calculated at each time instance.

The second consequence is the moving of the MS-local cluster. As the MS-local cluster is updated to a new position regarding to the MS movement, some local MPCs which are defined at the old positions will drop out the range of the new MS-local cluster. The dropped-out MPCs are then re-filled in the updated local cluster at randomly generated positions and are kept identical intra-cluster MPC fading, as explained in Fig. 8.2.5.

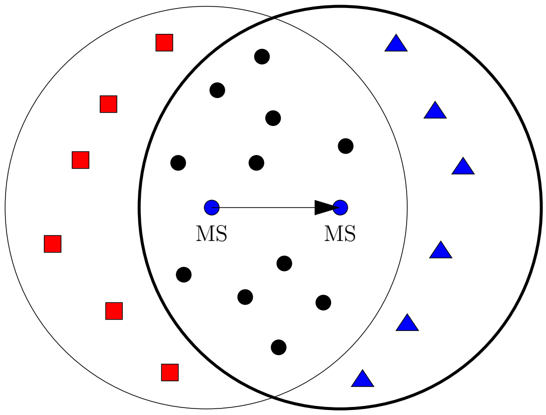

Figure 8.5: Update of MS-local cluster when MS moves. The old MPCs (squares) that are outside the range of the new local cluster are re-filled into the local cluster (triangles), keeping their fading properties.

8.3 Advanced parameters

Two advanced parameters are introduced in the COST 2100 model, the cluster-based polarization and DMC modeling.

8.3.1 Polarization

The COST 2100 model characterizes the channel polarization on cluster level and MPCs. Based on the work in [QOHDD10], a MPC consists of four polarization components, which are projected on the Tx and Rx antenna systems to form sub-polarization channels according to the polarization characteristics.

The four-channel polarization matrix of MPC p in cluster n is defined as:

$$\boldsymbol{G}_{n,p} = \begin{bmatrix} e^{j\varphi_{11,n,p}} & \frac{1}{\sqrt{\mathrm{CPR}_{n,p}\cdot\mathrm{XPD}_{\mathrm{H},n,p}}} e^{j\varphi_{12,n,p}} \\ \frac{1}{\sqrt{\mathrm{XPD}_{\mathrm{V},n,p}}} e^{j\varphi_{21,n,p}} & \frac{1}{\sqrt{\mathrm{CPR}_{n,p}}} e^{j\varphi_{22,n,p}} \end{bmatrix}, \qquad (8.13)$$

where $\mathrm{XPD_V}$, $\mathrm{XPD_H}$ and CPR are the cross-polarization power ratios of the VV to the HV channel, the HH to the VH channel and VV channel to the HH channel. These power ratios are characterized in each MPC. The phases of the four polarization channels in a MPC is defined as an iid uniformly distributed random variable between 0 and

2π. The matrix is then normalized by:

$$\boldsymbol{G}_{n,p} = \boldsymbol{G}_{n,p} / \left\| \boldsymbol{G}_{m,p} \right\|, \tag{8.14}$$

and multiplied by the complex amplitude of the MPC, $a_{n,p}$, in Eq. 8.12.

The cross-polarization power ratios in Eq. 8.13 are defined per MPC and per cluster. They are log-normally distributed in a cluster, with a mean μ_{XPD_n} and a STD σ_{XPD_n} defined. The μ_{XPD_n} and σ_{XPD_n} are also log-normally distributed, with parameters $(\mu_{n,\mu_{\mathrm{XPD}}}, \sigma_{n,\mu_{\mathrm{XPD}}})$ and $(\mu_{n,\sigma_{\mathrm{XPD}}}, \sigma_{n,\sigma_{\mathrm{XPD}}})$ respectively.

8.3.2 Dense multi-path components

In previous sections, the COST 2100 model was built upon the assumption of specular scattering. This simplification assumes that the interaction between a scatterer and the signal wave generates a single propagation path. In reality, scattering mechanisms are usually complicated and cannot be fully described by a few specular paths with corresponding explicit geometry as modeled above. Rough surface reflection, corner diffraction, and reflections from different layers of a scatterer can all contribute to a large amount of diffuse scattering. Hence, diffuse scattering will form a significant channel component in both delay and angular domains, which the specular MPC fail to capture.

There are two approaches to model the diffuse scattering:

1. The propagation paths are extended with a continuous dispersion over delay and angular domains to include diffuse scattering characteristics, as studied in [DE01].

2. The diffuse scattering can also be modeled by the superposition of a large number of specular paths with modified delays, angles, and amplitudes, called the DMCs [PSH+10, PSH+11].

The first method relies on the quality of the modeling of the path dispersion, while a model mismatch might create a significant amount of artifacts. The second method, on the other hand, increases the total number of parameters but provides the best capture of the residual channel spectrum as long as the number of the DMCs is sufficiently large. Based on the work in [PSH+10, PSH+11], the COST2100 model considers the second approach as a direct extension of the MPC concept [PTH+10].

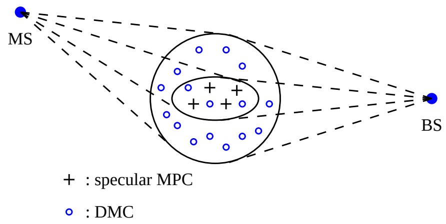

(a) Clustering of DMCs

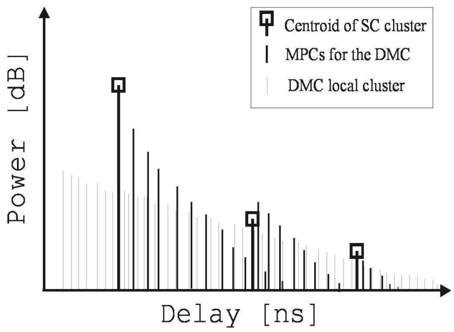

(b) Power decaying of DMC

Figure 8.6: Cluster-based modeling of DMC in COST 2100 model

In principle, a DMC is a modified MPC that is described by its own delay, angles, fading, and power attenuation. The DMC is the result of multiple intra-cluster interactions. Therefore the DMC is characterized by a weaker geometry relation between its spatial distribution and its delays and angles. Hence, a DMC needs more parameters to describe its geometric inconsistency.

The modeling complexity of the DMC is controlled by a cluster-level characterization. A clustering of DMC is modeled to each cluster, locating at the same position as shown in Fig. 8.6. The clustering of the DMCs is defined by its own spatial spread to satisfy the delay and angular spread of the residual channel spectrum besides the spectrum of the specular MPCs.

Each MPC in the cluster is further expanded by a sub-clustering of DMCs. The power of DMCs in the sub-clustering is modeled to decay relatively to the power of corresponding MPC, when the delay difference between the DMC and MPC increases, as illustrated in Fig. 8.6(b). Such decaying is characterized by the decaying factor, denoted as κ_{DMC}. The DMCs share the large-scale properties of the cluster, such as the visibility, shadowing, and cluster power attenuation.

8.4 Parameterization

The parameterization of the COST 2100 model in various scenarios represents a huge effort, which has been performed by several research groups with COST 2100 Action. In addition to previous parameterizations carried out for marcro-, micro-, and pico-cellular [Cor06], outdoor rural environments at 400 MHz band and indoor pico-cellular scenarios at 3.6 [QOHDD10] and 5.3 GHz [PHL+11, Pou11] bands have been covered. A complete list of parameters and recommended distributions is presented in [Ver11]. The overall availability of the parameters is broad, though it must be noted that advanced parameters for DMC and multi-link aspects are still not sufficiently supported by measurements.

In general, the parameters are divided into external and stochastic parameters. Table 8.1 lists the parameters in the single-link COST 2100 model is given.

The modeling of non-negative parameters, including the cluster delay and angular spread, cluster shadowing, cluster link-delay, LOS power factor, and DMC spatial spread, is based on the following equation:

$$X = \mu_X 10^{\sigma_X W/10}, \tag{8.15}$$

where μ_X is the mean of parameter X on linear scale, σ_X is the STD of X in dB, and $W \sim \mathcal{N}(0,1)$. Defining μ_X on linear scale make it with physical meaning. The random generation of the variable in dB in Eq. 8.15 guarantees that the variable is always positive.

External parameters	
Cell radius	r_{cell}[m]
Central frequency	f_c[Hz]
Bandwidth	B[Hz]
Misc. parameters for pathloss	...
Stochastic parameters	
VR size	R_C [m]
TR width	L_C [m]
Cluster power decaying factor	k_τ [dB/μs]
Cluster power decaying cut-off factor	τ_b [s]
LOS cut-off distance	$d_{b,LOS}$ [m]
LOS VR size	R_{LOS} [m]
LOS TR width	L_{LOS} [m]
LOS power factor ζ distribution	μ_k [linear]/σ_k [dB]
Local cluster at BS	true/false
Local cluster at MS	true/false
Average number of remote cluster	$\mu_{num,C}$
K-selection factor	K_{sel}
Number of MPC per cluster	N_{MPC}
Cluster: delay spread mean/std	μ_τ [s]/σ_τ [dB]
Cluster: AoD spread mean/std	$\mu_{\phi,BS}$ [s]/$\sigma_{\phi,BS}$ [dB]
Cluster: EoD spread mean/std	$\mu_{\theta,BS}$ [s]/$\sigma_{\theta,BS}$ [dB]
Cluster: AoA spread mean/std	$\mu_{\phi,MS}$ [s]/$\sigma_{\phi,MS}$ [dB]
Cluster: EoA spread mean/std	$\mu_{\theta,MS}$ [s]/$\sigma_{\theta,MS}$ [dB]
Cluster: shadow fading STD	σ_{SF}
Cluster: correlation matrix	$\boldsymbol{\rho}$
Cluster: distribution Φ_C, mean/std	μ_{Φ_C} [deg.]/σ_{Φ_C} [deg.]
Cluster: distribution Θ_C, mean/std	μ_{Θ_C} [deg.]/σ_{Θ_C} [deg.]
Cluster: Min. cluster-BS distance	r_C [m]
Cluster link-delay, mean/std	$\mu_{\tau_{C,link}}$ [s]/$\sigma_{\tau_{C,link}}$ [dB]
Polarization: XPD mean/std	μ_{XPD}/σ_{XPD}
Polarization: CPR mean/std	μ_{CPR}/σ_{CPR}
DMC: spatial spread mean/std	$\mu_{DMC}[m]/\sigma_{DMC}$ [dB]
DMC: decaying factor	k_{DMC} [dB/μs]

Table 8.1: Essential parameter list of single-link COST 2100 channel model

CHAPTER 9

Multi-link COST 2100 channel model

9.1 Overview of multi-link modeling approaches

Measurements have shown that different links can be correlated even if the BSs or MSs are well separated [KHea10]. The large-scale link correlation is defined as the correlation of two channels separated at the BS side or the MS side in a distance larger than the coherence distance. For the cluster-based GSCMs, one possible explanation is the existence of correlated clustering, i.e. clusters in different links exhibit correlation on the cluster shadowing or intra-cluster MPC fading, as investigated in [CBY07]. Using correlated clusters contradicts the uncorrelated-clustering assumption adopted in the COST 2100 model, hence requiring substantial modifications of the modeling approach. Another explanation is to consider that some clusters are simultaneously visible in different links so that links share the cluster shadowing and intra-cluster MPC fading, which is described as the cluster's link-commonness. The latter possibility only requires to model the cluster visibility in multiple links, and maintaining the physical descriptions of the clusters, e.g. the spatial spread and the fading.

In this chapter, we model the cluster link-commonness at both BS and MS sides. A backward compatible multi-link extension of the single-link COST 2100 model is described with modeling principles and implementation methods.

9.2 Clusters link-commonness

The COST 2100 model uses the concept of VR to describe the visibility of the clusters in a single-link. In single-link scenarios, a cluster is connected to a single VR and a single BS. This is can be viewed as a special case of the cluster link-commonness in a single-BS single-MS link. In a multi-BS multi-MS link, a cluster can be simultaneously connected to multiple stations, therefore different links share the shadowing and intra-cluster MPC fading from the cluster. Generally, the cluster link-commonness contains both BS-commonness and MS-commonness.

9.2.1 BS-commonness

The cluster BS-commonness describes the connection of a cluster to multiple BSs, whose visibility is determined also in a VR as defined in the single-link scenarios. When a MS enters the VR, link connections between the MS and multiple BSs are established through the corresponding cluster. The maximum cluster BS-commonness depends on the number of BSs in the environment.

9.2.2 MS-commonness

The cluster MS-commonness describes the connections of a cluster to multiple MSs. The multiple MS connections are defined by two conditions: 1), connections to different MSs distributed in an area larger than a single VR; 2), discontinuous lifetime of the cluster in a single link during a large movement of the MS, i.e. in a virtual single-BS multi-MS communication. The cluster MS-commonness is modeled by connecting multiple VRs to the cluster, therefore the cluster can be visible for well separated MSs. The VRs connected to a cluster are defined as a VR group of the cluster. Measurements in [PHL$^+$10] characterizes cluster MS-commonness in virtual single-BS multi-MS scenarios, where the number of VR in the VR group can be estimated as:

$$n_{\mathrm{VR}} = \frac{t_{\mathrm{total}}}{t_{\mathrm{VR}}}, \tag{9.1}$$

where t_{total} is the total lifetime of the cluster and t_{VR} is the lifetime of the cluster in single VR. In statistics, n_{VR} is modeled as a Poisson distributed random variable.

The grouping of VRs to one cluster does not change the size and distribution of the VRs. Overlapping VRs in the group form a larger continuous area of the cluster link visibility as observed in [PHL$^+$10]. The visibility gain in the overlapped region should take the maximum gain of the overlapped VRs.

9.2.3 General link-commonness

We model the cluster BS-commonness and MS-commonness as independent properties of a far cluster. In a multi-BS multi-MS scenarios, a far cluster can be connected to multiple BSs and multiple VRs. Each VR in the VR group of a far cluster determines the cluster's BS-connection independently. An typical example is shown in Fig. 9.1 of a far cluster connected with two BSs and three VRs. In each VR, the cluster BS-connections are determined differently. This will finally result in different link-commonness when the MSs are located in different VRs.

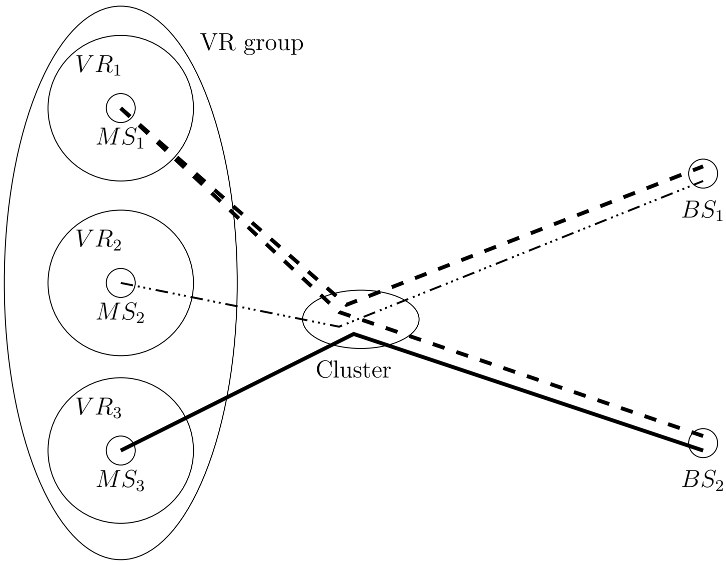

Figure 9.1: An example of cluster link-commonness in multi-BS multi-MS communications. Lines represent different link connections.

The link-commonness of far clusters are modeled independently to the cluster physical properties such as the delay and angular spread, shadowing, etc. The cluster modeling approaches applied in the single-link model should also be applied to the clusters in the multi-link scenarios.

9.3 Parameterization of cluster link-commonness

The cluster link-commonness is characterized based on the physical clusters and VRs in the environment. Their projections on each BS-MS link form the logical propagation environment to determine the single-link channel statistics. When parameterizing a multi-link scenario, the channel statistics in individual links should be consistent with the single-link

COST 2100 model as presented in Ch. 8.

9.3.1 Cluster link-commonness ratio

Cluster link-commonness ratio includes the ratio of cluster BS-commonness and the ratio of cluster MS-commonness.

9.3.1.1 BS-commonness ratio

The cluster BS-commonness ratio is the possibility for a MS to observe a number of m BSs when it is in a certain VR in the environment. As a VR is always connected to only one cluster, this ratio is equivalent to the ratio of the number of VRs which are connected to m BSs to the total number of VRs in the environment as:

$$\eta_m = \frac{L_m}{\sum_{m'=1}^{M} L_{m'}}, \tag{9.2}$$

where L_m is the number of VRs connected to m BSs.

The ratio η_m is related to the number and distributions of BSs. Future measurements are needed to fully characterize the geometric dependence of η_m. In a 2-BS 1-MS dual-link scenario as measured in [PHS$^+$10], only η_2 is characterized as a constant value regardless of the BSs distribution.

To maintain an equal average number of visible far clusters and VR density in each link, the projection of the physical VRs to each BS should be equal to the VR density modeled in the single-link scenarios. Since a VR connected to m BSs will be projected m times, a simple relationship between the number of physical VRs and the number of VR projections to each BS is expressed as:

$$MQ = \sum_{m=1}^{M} (mL_m), \tag{9.3}$$

where Q corresponds to the VR density to each BS defined in the single-link scenarios.

9.3.1.2 MS-commonness ratio

The cluster MS-commonness ratio is the number of VRs connected to a far cluster, which follows a Poisson distribution. The grouping of VRs only increases the possibility of different MSs to observe the same cluster, therefore it has no impact to maintain the single-link consistency.

9.3.2 Cluster distribution

For a far cluster connected with multiple BSs and VRs, a reference BS and a reference VR should be selected to determine the cluster distribution based on the approach in single-link scenarios. A simple selection scheme is proposed based on the number of link connections enabled by the VRs and BSs, as shown in Fig. 9.2

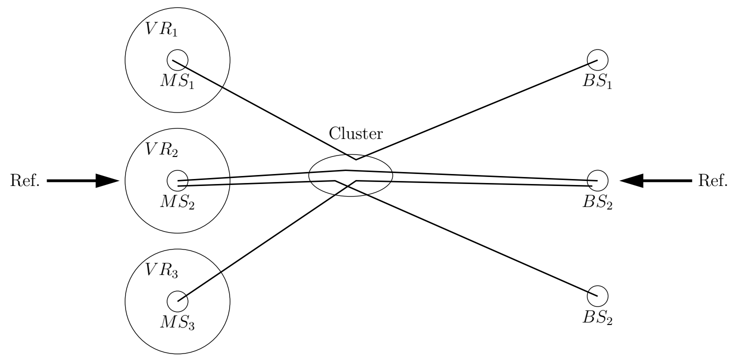

Figure 9.2: Reference BS and VR selection for the distribution of a link-common cluster, lines representing link connections

9.3.3 K-selection factor

In multi-link scenarios, parameter K_{sel} is applied to the physical clusters to determine the ratio of the twin clusters to the single-bounce clusters. Although the K_{sel} in each single-link will vary because of the multiple projections of the cluster onto the single-links, the average value of K_{sel} remains constant for all links.

9.4 VR assignment table

To statistically characterize the cluster link-commonness in an environment, we introduce a VR assignment table. Fig. 9.3 provides a simple example of cluster link-commonness in a multi-link scenario. With respect to Fig. 9.3, an example of the corresponding VR assignment table is generated in Table 9.1.

The VR assignment table is a two-dimensional table. Its rows represent the index of the BSs and its columns represent the index of the VRs. Each entry in the table represent the link connection between a BS and

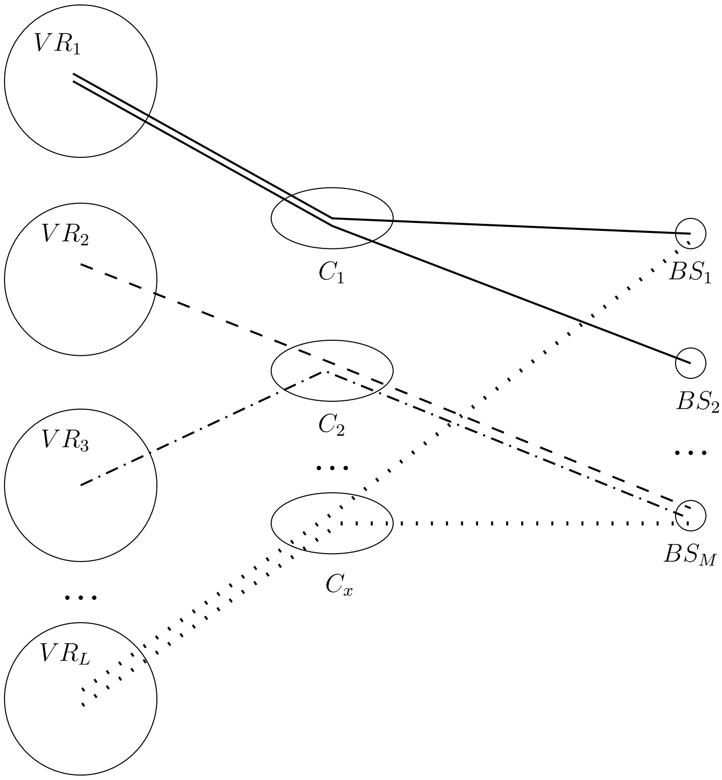

Figure 9.3: An example of link-common clusters in multi-link scenario in COST 2100 channel model

	VR_1	VR_2	VR_3	...	VR_L
BS_1	1, C_1	0, /	0, /	...	1, C_x
BS_2	1, C_1	0, /	0, /	...	0, /
...	...	...	...	...	...
BS_M	0, /	1, C_2	1, C_2	...	1, C_x

Table 9.1: Realization of VR assignment table corresponding to the link-common clusters in Fig. 9.3. 1/0 describes if a VR is linked to the BS or not, C_x represents the index of the cluster that the VR is linked to

a VR. The entry contains two values: the first value (1/0) represents whether there is a connection between the BS and the VR; the second value is the index of the cluster that connects the BS and the VR.

The VR assignment table should fulfill the following rules to correctly reflect the cluster link-commonness.

1. Each VR should be related to only one cluster and at least one BS. It means each column in the table should contain at least one "1" for the first value and should have the same cluster indices C_x for the second element.

2. In reverse, a cluster should be connected with at least one VR and one BS.

3. The VR density to each BS should be identical by keeping the sum of the first elements in each row equal. The cluster link-commonness ratio should also be reflected in the table.

9.5 Scalability of multi-link channel modeling

The scalability of the multi-link COST 2100 channel model includes two aspects, the change of the number of BSs and the change of the number of MSs. The latter aspect can be fully satisfied by the current model, since the multi-link modeling is independent of the number and distributions of MSs. The former includes two possibilities: the number of BSs decreases or the number of BSs increases.

In BS-centric channel modeling, when a BS is turned off, scatterers with respect to this BS disappear from the communications. In a multi-link scenario, when a BS is removed from the communication, all link connections to this BS via the clusters in the environment will be lost. Therefore, if a cluster is only linked to this BS, it will be removed from the environment as well.

By contrast, if new BSs are added to the multi-link communication, the environment will response to the new radio sources. Therefore link connections to the new BSs will be created from the existing clusters and new clusters.

In both cases when the number of BSs increases and decreases, the modeling consistency should be carefully treated on the multi-link parameters.

9.6 Model validation

The validity of the multi-link COST 2100 channel model has been widely discussed in various metrics on the properties such as the angular and delay spreads, parameter distributions, and inter-link correlation. In general, the comparison between the measured LSPs and synthesized LSPs from the model depends on the qualities of channel estimation and model parameterization. In the following, we focus on one metric representative of multi-link scenarios.

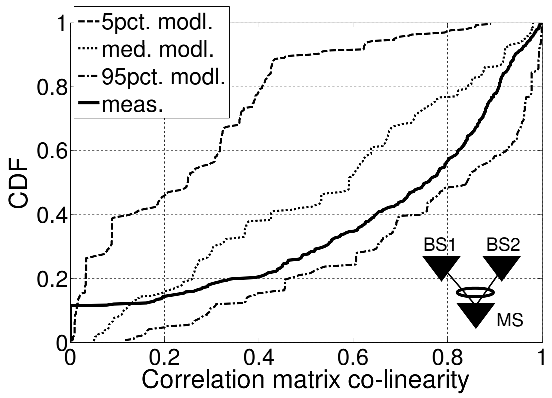

Figure 9.4: Comparison of CMCs from measurements and channel model outputs. The curve from measurements falls within the range of 5% and 95% curves of the channel model outputs, revealing the validity of the channel model to re-create measured channel characteristics.

Fig. 9.4 presents a comparison between measurements and corresponding model simulations on the inter-link correlation in a dual-BS single-MS communication scenario [HPT+11]. The measurements were performed in an indoor corridor environment at 5.3 GHz [Pou11]. Vertically polarized planar dipole antenna arrays were considered at the BSs and MS. Detailed settings of the measurements and the simulations can be found in [HPT+11]. Because of the dominant waveguiding propagation in the corridor, the measurements show significant inter-link correlation between two BSs located at different wings of the same building. Such inter-link correlation is measured by the Correlation Matrix Co-linearity (CMC) between the correlation matrices of the two BS-MS links [HPT+11]. The CMC is a distance between the correlation matrices, giving 1 when the matrices are linearly dependent and yielding 0 if they are orthogonal. In Fig. 9.4, three CMC curves, representing 5, 50, and 95 %, are derived from the model simulations. The measured curve, as shown in the figure, remains below the range of simulations, demonstrating that the model is capable to predict the inter-link correlation as observed in the measurements.

9.7 Conclusions

In this chapter, we have shown a promising capability of a multi-link extension of from the single-link COST 2100 model thanks to its cluster level structure. The cluster link-commonness is introduced to describe the multiple cluster link-visibility based on VR. Compatibility issues between the multi-link modeling and the single-link modeling are addressed, and the model consistency is maintained. More measurements are expected to support the model, to validate the extension in various scales, and as well as to complete the parameterization in different environments.

CHAPTER 10

Implementation of COST 2100 channel model

In this section, we will describe the details of the implementation of the time-varying COST 2100 channel model in mobile scenarios. An single-link implementation example is also presented at the end of this chapter.

10.1 Additional parameters

An implementation of the multi-link COST 2100 channel requires the external and internal parameters of the COST 2100 channel model in Table. 8.1 and the multi-link parameters described in Chapter 9. To implement the model in dynamic scenarios, additional parameters are needed as follows:

1. Positions of MSs and BSs, described in cartesian coordinate.

2. Velocity vector of MSs, described in cartesian coordinate.

3. Pathloss model, e.g. the Cost231-Walfisch-Ikegami model in macrocell [Cor99] , the indoor pathloss model in [MB00].

4. Channel sampling rate.

5. Length of time observation of the channels.

6. Antenna array steering vectors at the MSs and BSs.

7. Over-sampling rate when synthesizing the CIR.

10.2 Flowchart

The implementation consists of two stages, the environment initialization and the CIR synthesis. The initialization stage include the initialization of the VR assignment table, and the initialization of the environment (clusters, MPCs). With the help of the VR assignment table, each

MS-BS link is synthesized as an independent link, therefore the synthesizing process is simplified. A complete flowchart of the implementation is given in Fig. 10.2.

10.3 Algorithms

10.3.1 Initialization of VR assignment table

Although the cluster link-commonness is expected to be related with the link geometries, current measurements are insufficient to support such characterization. The VR assignment table is then generated randomly, therefore the statistics of the cluster link-commonness is equally described in the environment.

The implementation of the VR assignment table for a multi-link scenario with M BSs is stated below.

1. Generate essential stochastic parameters, including: average number of remote cluster, twin cluster ratio, BS-common cluster ratio (1, 2, ... M), average number of grouped VRs of a remote cluster.

2. Create an empty VR assignment table with M rows and MQ columns.

3. Assign the BS link-commonness of VRs, for $m = M : -1 : 2$

   (a) Determine L_m, i.e. the number of VRs connected to m BSs, by the cluster BS-commonness ratio η_m.

   (b) In the table, sequentially select L_m VRs and randomly connect m BSs to each VR.

   (c) If a BS has reached its VR density, it should be skipped in the VR assignment. If the total number of available BSs is less than m, jump to the next $m-1$ BS common VR assignment.

4. Generate the non-common VRs for each BS until each BS has reach its VR density.

5. Withdraw the VRs in the table that have not been assigned to any BS.

6. Generate the VR groups, for $q = 1 : \sum_{m=1}^{M} L_m$

   (a) Select VR_q if it is not grouped.

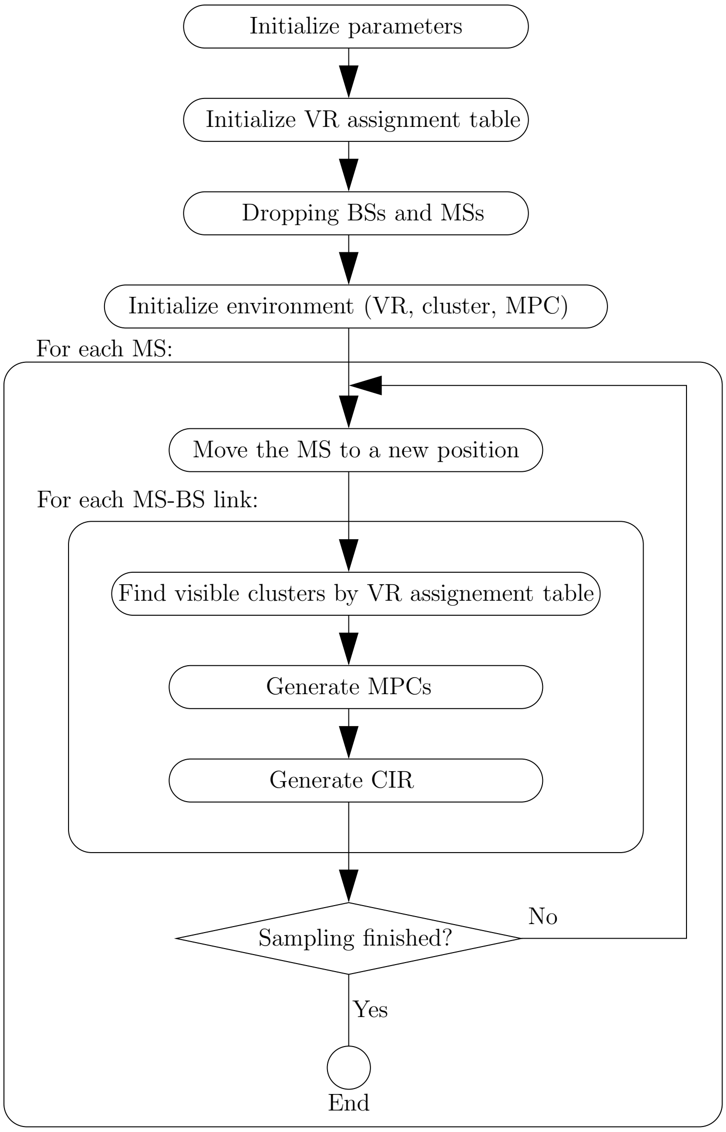

Figure 10.1: Implementation flowchart of the time-varying mutli-link COST 2100 channel model

(b) Generate the random number n of VRs to be grouped.

(c) Randomly choose the other n-1 VRs and assign them together with VR q to one far cluster.

(d) If the number of available VRs are less than n, regenerate n.

10.3.2 VR distribution

For simplicity, the implementation defines the cell range independently of the BSs distributions in a multi-link scenario. The uniform distribution of the VRs is generated in the cell area by the following way:

1. Generate a uniform distribution of the VRs by the VR density in a square area large enough to cover the cell.

2. Tail the cell from the square area. Only VRs inside the cell are kept.

10.3.3 Cluster parameterization

The delay, AoD, EoD, AoA, EoA, and the shadowing of a cluster are correlated random numbers, which are generated by:

$$\begin{bmatrix} \tau \\ \phi_{C,BS} \\ \theta_{C,BS} \\ \phi_{C,MS} \\ \theta_{C,MS} \\ SF \end{bmatrix} = \begin{bmatrix} \mu_\tau 10^{M_1\sigma_\tau/10} \\ \mu_{\phi_{C,BS}} 10^{M_2\sigma_{\phi_{C,BS}}/10} \\ \mu_{\theta_{C,BS}} 10^{M_3\sigma_{\theta_{C,BS}}/10} \\ \mu_{\phi_{C,MS}} 10^{M_4\sigma_{\phi_{C,MS}}/10} \\ \mu_{\theta_{C,MS}} 10^{M_5\sigma_{\theta_{C,MS}}/10} \\ 10^{M_6\sigma_{SF}/10} \end{bmatrix}, \quad \begin{bmatrix} M_1 \\ M_2 \\ M_3 \\ M_4 \\ M_5 \\ M_6 \end{bmatrix} = \boldsymbol{AV} \tag{10.1}$$

where $\boldsymbol{V}$ is an iid normal distributed vector, and $\boldsymbol{A}$ is the Cholesky factorization of the correlation matrix $\boldsymbol{\rho}$.

10.3.4 MultiPath Component

MPCs in a local cluster have a uniform distribution in space. MPCs in a far cluster have Gaussian distribution in space. The fading of the MPCs in a cluster has to be normalized so that the total power of the MPCs does not exceed the power of the cluster, as:

$$A_{MPC,n,p} = A_{MPC,n,p} / \sqrt{\sum_{p=1}^{P} |A_{MPC,n,p}|^2} \tag{10.2}$$

10.3.5 Dense Multipath Component

The clustered DMCs are modeled as having omni-directional spread in space. Implementing a DMC clustering is the same as implementing a MPC clustering. The DMC grouping shares the cluster parameters, including the shadowing, the visibility gain, the cluster link-delay, and the power attenuation. As described in Sec. 8.3, the sub-clustering of DMCs with respect to each MPC in the cluster has extra delay and spatial spread to capture the residual channel spectrum. To fulfill this, a DMC is attributed by an extra delay, which is generated depending on the delay spread of the residual channel spectrum. To describe the dense scattering effect, a random phase is assigned to each DMC.

10.3.6 MIMO channel matrix synthesis

The synthesis of MIMO channel matrix follows Eq. 8.2. Practical MIMO systems should also consider the pulse-shaping of the CIR to meet the bandwidth limitation, as by [Pro00].

10.4 Implementation example

In this section, we present an implementation example of the single-link COST 2100 model in macrocell. We define a dynamic scenario where a MS is passing by the BS along a single direction and at a constant velocity. The external and stochastic parameters of the model are referred in [Cor06]. Additional parameters are given in Table 10.1.

Environment	macrocell
Input power	0 [dB]
BS position (x, y, z)	(0, 0, 0) [m]
MS initial position (x, y, z)	(-200, 5, 0) [m]
MS velocity (x, y, z)	(4, 0, 0) [m/s]
Channel sampling rate	1 [s]
Number of channel sample	200

Table 10.1: Implementation settings of a single-link channel in marcocell

The local cluster at MS side is enabled in the implementation to mark the MS movement.

The implementation results are presented by the time-varying power profiles of the channel in delay and angular domains respectively, as shown in Fig. 10.2.

In the power-delay profile presented in Fig. 10.2(a), the MS-local cluster and the remote clusters show distinct lifetimes and delays. The MS-local cluster has the smallest delay and strongest power, whose lifetime last throughout the simulation, as observed in Fig. 10.2. The remote clusters have limited lifetimes when the MS is passing their related VRs, which appear as a short duration of the cluster in the power-delay profile. The time-variation of the delay of the MS-local cluster also reflects the MS movement when it approaches and leaves the BS.

The difference between the MS-local cluster and remote clusters can also be observed in the power-AoA profile in Fig. 10.2(d). The local cluster surrounding the MS causes an omni-directional power distribution throughout the AoA, while the remote clusters form a limited AoA spread and short lifetime in the power-AoA profile in Fig. 10.2(d).

As the MS eventually moves away from the BS, the azimuth spread in the power-AoD profile in Fig. 10.2(b) decreases accordingly.

Both the power-EoD and power-EoA profiles of the channel have small elevation spread as shown in Fig. 10.2(c) and Fig. 10.2(e), which are determined by the cluster elevation spread in macrocell.

The implementation has also been evaluated in indoor environment as in [HPL$^+$10].

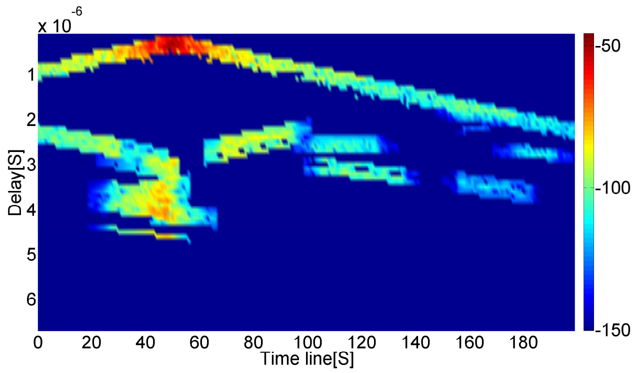

(a) Power-delay profile

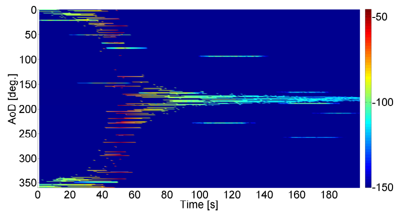

(b) Power-AoD profile

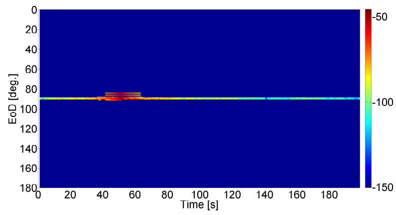

(c) Power-EoD profile

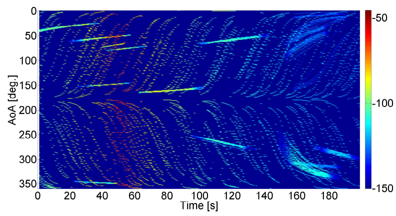

(d) Power-AoA profile

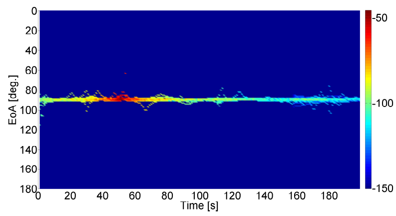

(e) Power-EoA profile

Figure 10.2: Implementation results of a single-link macrocell communication

CHAPTER 11

Analysis of cooperative MIMO in cellular networks

In this chapter, we investigate the impact of cluster link-commonness to cooperation mobile networks. In general, a cooperative network between multiple BSs and multiple MSs is a distributed MIMO system. We then focus on the sum-rate capacity of a distributed MIMO system.

11.1 Sum-rate capacity of cooperative MIMO

Although MIMO systems are well-known for their ability to improve the spectra efficiency, realistic collocated MIMO systems are usually limited by the cross-channel correlation due to limited MPCs or keyhole effect [SL03, CFGV02]. A distributed MIMO system is a generalized MIMO system which can better capture the signals by allocating multiple antenna clustering in different positions. This technique can be found in CoMP and general cooperative MIMO systems [WHG+10].

Considering a distributed MIMO system with n_t Tx terminals and n_r Rx terminals, each Tx terminal equipped with an antenna array of M antennas and each Rx terminal equipped with an antenna array of N antennas. By having cooperation among the terminals, a large virtual MIMO system is formed [ZD04], which is expressed as:

$$
\begin{aligned}
\boldsymbol{y} &= \mathrm{H}\boldsymbol{x} + \boldsymbol{n} \\
\boldsymbol{y} &= [\boldsymbol{y}_1, \boldsymbol{y}_2, ...\boldsymbol{y}_{n_r}] \\
\boldsymbol{x} &= [\boldsymbol{x}_1, \boldsymbol{x}_2, ...\boldsymbol{x}_{n_t}] \\
\boldsymbol{n} &= [\boldsymbol{n}_1, \boldsymbol{n}_2, ...\boldsymbol{n}_{n_r}] \\
\mathbf{H} &= \begin{bmatrix} \mathbf{H}_{1,1} & \mathbf{H}_{1,2} & ... & \mathbf{H}_{1,n_t} \\ ... & & & \\ \mathbf{H}_{n_r,1} & \mathbf{H}_{n_r,2} & ... & \mathbf{H}_{n_r,n_t} \end{bmatrix}
\end{aligned}
\tag{11.1}
$$

where each $\mathbf{H}_{p,q}$ is a $M \times N$ MIMO channel matrix between the pth Tx and the qth Rx terminal.

The sum-rate capacity of distributed MIMO is computed by the joint virtual channel matrix based on Eq. 11.1 as:

$$C = \log_2[\det(\mathbf{I} + \mathbf{H\Sigma H}^T)] \quad (11.2)$$

where $\mathbf{\Sigma}$ is the covariance matrix of the transmitted signal.

Based on the CSI knowledge, the capacity in Eq. 11.2 is divided into two possibilities.

1. If the CSI is unknown at the Tx, equal power allocation should be performed, which turns Eq. 11.2 into:

$$C = \log_2[\det|\mathbf{I} + \frac{\gamma}{n_t N}\mathbf{HH}^H|], \quad (11.3)$$

   where γ is the input SNR.

2. If the CSI is known at the Tx, waterfilling algorithm [CT91] is applied to maximize the channel capacity, which turns Eq. 11.2 into:

$$C = \sum_{i=1}^{n_r M} \log_2[1 + g_i \gamma \Lambda_i], \quad (11.4)$$

   where Λ_i is the ith eigenvalue of $\mathbf{HH}^H$, and g_i is the weight of the power allocation to the ith eigen-channel of $\mathbf{HH}^H$ computed through the waterfilling algorithm.

The ergodic and outage capacities are computed by Eq. 6.3 and Eq. 6.4 as:

$$C_{erg} = E[C]$$
$$Pr(C < C_{out}) = P_{out} \quad (11.5)$$

where the outage probability is also set 10% in our investigation.

11.2 Simulation settings

The COST 2100 model describes the multi-link channel properties by introducing the link-common clusters. In this section, we will evaluate the effect of different cluster BS-commonness ratio in a cooperative multi-BS single-MS scenario. We define a dual-BS single-MS scenario as shown in Fig. 11.2. Both the BSs and the MS are equipped with ideal linear antenna arrays , whose steering vector in azimuth is given by:

$$\boldsymbol{s}(\phi) = [1, e^{j\cos\phi d_a/\lambda}, e^{j\cos\phi 2d_a/\lambda} ... e^{j\cos\phi N d_a/\lambda}] \quad (11.6)$$

where d_a is the space between adjacent antennas, and λ is the wavelength at the carrier frequency. To simplify the analysis, the number of antennas equipped at both the BSs and the MS is fixed at 4, i.e. $N = M = 4$, and the arrays have $0°$ orientation in azimuth as shown in Fig. 11.2.

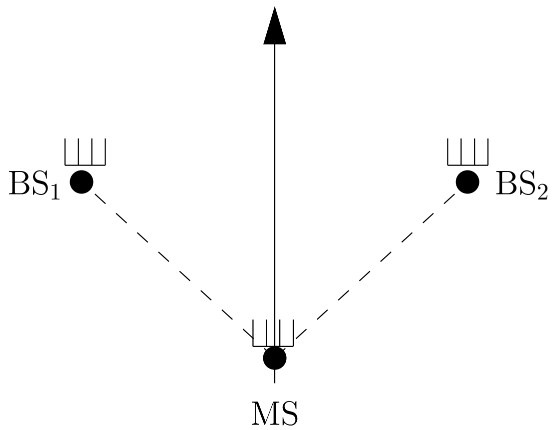

Figure 11.1: Simulation setting of a dual-BS single-MS distributed MISO system where linear 4-antenna arrays are equipped on both BSs and MS, arrow point the moving direction of MS

The MS is located on a line between the BS_1 and BS_2 as in Fig. 11.2 to guarantee that the distances from the MS to the BSs are always equal. Hence, the pathloss levels of the two BS-MS links are always equal.

We consider a macrocell environment with parameters given in [Cor06]. To control the LSPs in different simulation realizations, we fix the number of average visible remote clusters at 4.

There is only one cluster BS-commonness ratio to be investigated in the dual-BS scenario, η_2. We consider three different values of η_2:

1. $\eta_2 = 100\%$, meaning that all the far clusters in the environment are connected to both of the BSs.

2. $\eta_2 = 50\%$, meaning that half of the far clusters in the environment are connected to both of the BSs.

3. $\eta_2 = 0\%$, meaning that all th far clusters in the environment are only connected one BS.

We further remove the local clusters at both BSs and MS to highlight the effects of link-commonness of far clusters.

Table 11.1 lists the details of the simulations.

Environment	macrocell
Frequency	1.8 GHz
Average number of visible far-clusters	4
Local clusters	not visible
BS_1 position	[-200 0 0] [m]
BS_2 position	[200 0 0] [m]
MS initial position	[0 -100 0] [m]
MS velocity	[0 1 0]
Antenna array	ideal linear array
Number of antennas in the antenna array	4
Antenna spacing d	0.5λ
Channel sampling rate	0.5 s
Simulation length	200 s
Simulation repetition	100

Table 11.1: Simulation settings of distributed MIMO communications

11.3 Simulation results

The simulation is repeated at each BS-commonness ratio. The average channel capacities based on equal and waterfilling power allocation are presented in Fig. 11.2 and Fig. 11.3 respectively. In general, under both of the power allocation schemes, the cooperative dual-links exhibit a significant increase of the sum-rate channel capacity as compared to each single link. This is primarily because distributed BSs are capable to see more MPCs, hence the eigenvalues of the virtual MIMO channel matrix are increased.

The ergodic sum-rate capacity shows a small decrease as η_2 increases from 0% to 100%. Recall that as described in Chapter 9, the number of physical remote clusters increases when η_2 drops, therefore the remote clusters in a scenario with $\eta_2 = 0\%$ will have a wider distribution than in a scenario with $\eta_2 = 100\%$. This leads to a richer clustering environment under $\eta_2 = 0\%$ where the dual-link can capture more MPCs.

The outage sum-rate capacity shows a significantly increase when η_2 drops. It highlights the influence of the shadowing and intra-cluster MPC fading from the link-common clusters. The identical MPC fading from the link-common clusters will reduce the spatial diversity between

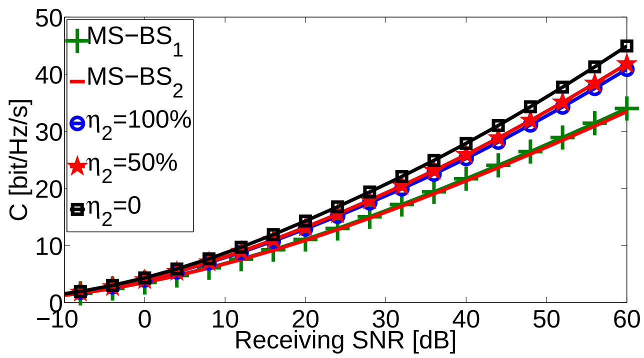

(a) Ergodic capacity

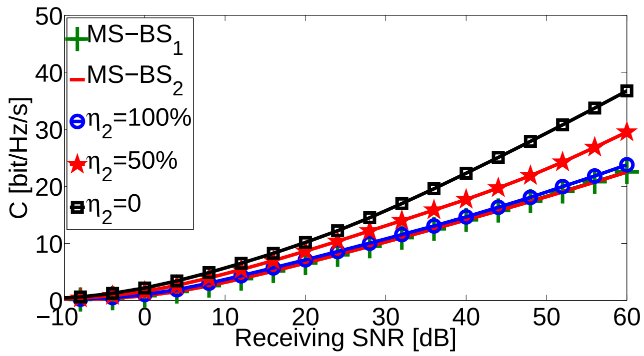

(b) Outage capacity, P_{out}=10%

Figure 11.2: Comparison of sum-rate channel capacity of dual-link MIMO channels in different cluster BS-common ratios, equal-power allocation

the links. Therefore, if more clusters are linked to both BSs, the mitigation of the channel fading by combing the received signals from the two BSs will be reduced, which cause a decrease of the outage sum-rate capacity.

11.4 Conclusion

In this chapter, we have shown the impact of link-common clusters to the sum-rate channel capacity in distributed MIMO systems. By considering a simple dual-BS single-MS network, we have compared the ergodic and outage sum-rate capacity of a macrocell network at different cluster

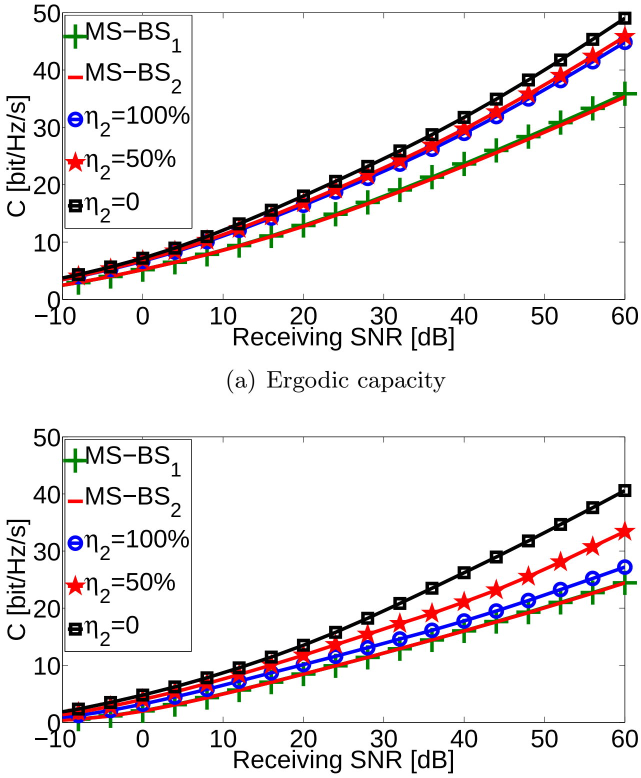

(a) Ergodic capacity

(b) Outage capacity, P_{out}=10%

Figure 11.3: Comparison of sum-rate channel capacity of dual-link MIMO channels in different cluster BS-common ratios, waterfilling power allocation

BS-commonness ratios. The simulations validate that when multi-links share common far clusters, the spatial diversity will be degraded. The same effect is also expected in more complex multi-link configurations and can be well described by the multi-link COST 2100 MIMO channel model.

CHAPTER 12
Dissertation conclusions

This dissertation has presented results on cooperative channel characterization and modeling for various networks. The essential multi-link channel parameters in body area and cellular mobile networks have been covered in the study. Although both networks differ fundamentally from the physical mechanism involved, the study has pointed out the common principles for describing the multi-link channel properties. In general, the scattering commonness has been proposed in both cases to describe the cross-channel correlation in cooperative multi-link communications. Geometric modeling approaches have been effectively applied to model the spatial dependence of channel properties. In addition, in both networks, various cooperative schemes have been evaluated based on realistic radio channels. The results in the study have provided a preliminary understanding of multi-link channels and essential modeling approaches.

12.1 Cooperative channels in body area networks

Extensive dynamic on-body measurements have been conducted to characterize and model the on-body channel statistics in different aspects in the study.

Canonical measurements at 2.45 GHz, as presented in Chapter 3, have focused on the spatial dependence of channel statistics, including pathloss, temporal fading, Doppler spectrum, and spatial channel correlation. Repetitive arm swing motions have been investigated in the measurements. Both tangential and normal polarizations have been covered. The measured channel statistics exhibit a significant spatial dependence. A general conclusion from the measurement results is that channels in normal polarization receive less body scattering effect and show lower pathloss levels and smaller temporal fading. Geometry-based statistical models have been proposed to describe the temporal fading and spatial variation of on-body channels. The repetitive arm swing causes strong patterns on the time-variation of the channels, resulting in frequency harmonics in the Doppler spectrum. The spatial channel correlation shows clear geometric trends in horizontal links in both polarizations. In vertical links, there is no clear relationship between the channel correlation and the link geometries, because arm scattering in the vertical direction involves a much more complicated process than in the horizontal direction.

Scenario-based measurements, as presented in Chapter 4, have focused on different scenarios identified by link geometries, subjects, motion modes, polarizations, and environments. These measurements have been conducted in indoor environments close to practical applications. Two sets of measurements have been performed at 2.47 GHz and 4.2 GHz respectively. Although greatly differing in the subjects and testbeds, similar conclusions are drawn in both measurements:

- Less geometric dependence are observed for on-body channels covering a large area across different body parts. Such observation highlights the complexity of body scattering.

- On-body channels in tangential polarization are sensitive to the antenna impacts, which show large statistical variation. On the contrary, on-body channels in normal polarization are less impacted by the body scattering and offer better link qualities.

- Body motion modes have a strong influence to the time-variation of on-body channels. Frequency harmonics are widely observed in the Doppler spectrum of the on-body channels under repetitive motions.

- Particularly, the temporal fading and spatial correlation of mobile on-body channels (fixed-mobile and mobile-mobile channels) are heavily related with the modes of body motions, because communication nodes move along with the body. This reason explains most of the correlated mobile channels in the measurements. Highly correlated on-body channels can then be predicted based on the motion modes and the link-geometries, which can help the design of cooperative multi-link BAN communications in practical scenarios.

An closed-form electromagnetic analytical model, as presented in Chapter 5, has been developed to provide a simplified physical explanation of the dynamic body scattering. The model offers a generic full-wave field solution of body scattering by simplifying the shape of the body. The model has been validated by deterministic and statistical comparisons with the canonical measurements. In general, the model successfully predict the on-body pathloss on the trunk in different polarizations and dimensions. It also well simulates the time-variation of horizontal channels in $\vec{z}$ polarization. Moreover, the simulation results by the model well match the measurements on the spatial channel correlation as a function of the distance difference in horizontal links. This model gives two important conclusions:

- On-body pathloss on the trunk, arms, or legs can be well modeled on a cylindric surface.
- On-body channels are formed by a limited number of propagation components scattered from different body parts. Therefore synthesizing an on-body channel can be made by a few components with proper gains and temporal fading.

The model has also been applied to describe the on-body antenna radiation pattern in off-body communications, which shows a consistent observation with the measurements on the reflection and shadowing effects of the body to the on-body antennas.

Simple cooperation schemes deployed in BANs, as presented in Chapter 6, have been investigated. single-relay, multi-relay, and cooperative dual-link have been evaluated based on realistic indoor channel measurements. The performances of the cooperation strategies have been evaluated in terms of capacity and/or diversity gains under different channel conditions. Based on the observation of generally uncorrelated on-body links in the measurements, the evaluation has considered the effects of pathloss difference and fading variance. It shows that simple cooperations can achieve significant capacity and/or diversity gains only when the channels in multi-link have close pathloss levels and large fading variances. Channels in realistic applications often fails this prerequisite due to large changes of the posture and motion modes, which impair the performance of simple cooperation schemes.

The presented results serve as a preliminary knowledge of radio propagation in body area. The investigations are expected to be improved in the following aspects:

1. Currently, only on-body channels on the trunk have been investigated in a canonical way and modeled by geometric approaches.
2. Channel polarization mismatch has not been covered, although it is frequently observed in the measurements. Since body scattering effect is sensitive to the channel polarization, the mismatch/change

of the polarization during movement will significantly increase the fading variation.

3. The antenna impacts have not been fully analyzed and have not been separated from the physical channels.

4. The number of investigated subjects is limited, which may hinder the model generality. On the contrary, increase the number of subjects in the investigation may increase the spatial variation of on-body channel statistics, which may lose the geometric dependence of the channel statistics.

5. Only narrowband on-body channels have been investigated.

6. Off-body propagation have not been investigated, and the on-body antenna properties in off-body communications have not been fully characterized.

Therefore, it will be interesting to cover the following aspects in future works:

1. The canonical measurements and geometric characterization of on-body links on other body parts such as on the leg/arm is expected. The analytical model is also expected to be applied in other link geometries.

2. Channel cross-polarization should be investigated, as well as the time-varying polarization mismatch in dynamic scenarios.

3. Subject variability is expected to be covered in the characterization and modeling of the BAN channels.

4. Joint studies between antennas and physical BAN channels will better describe the mutual coupling between the devices and the body.

5. Time-variation of on-body antenna radiation pattern in dynamic scenarios are expected to be characterized.

6. Off-body propagation, inter-body propagation, and the influence of off-body propagation to on-body channel in realistic environments are expected to be investigated.

12.2 Cooperative channels in cellular mobile networks

Our study on cooperative multi-link MIMO channels in cellular networks is based on the single-link and multi-link COST 2100 MIMO channel model. The study was carried out under the COST 2100 action with participants from various institutes. The major achievements in our study include a complete parameterization and implementation of the COST 2100 channel model, and a compatible multi-link modeling extension under the framework of the COST MIMO channel model.

In Chapter 8, the single-link COST 2100 MIMO channel model has been built based on the COST 273 model framework. While inheriting the essential modeling concepts from the COST 273 model, we have given concrete interpretation, parameterization and implementation methods to these concepts. Furthermore, advanced parameters, including the polarization and DMC, have also been included in the COST 2100 model in details.

The multi-link COST 2100 model, as presented in Chapter 9, has been developed within the COST 2100 action. The cluster link-commonness has been introduced in the model to describe the inter-link relationship in a multi-link scenario. The multi-link modeling has been introduced without modification on the cluster physics, which guarantees the model compatibility to single-link scenarios. The VR assignment table has been introduced to give an efficient implementation solution of the cluster link-commonness. Additional parameterization of multi-link modeling has also been described.

Detailed implementation algorithms have been presented in Chapter 10. A Matlab implementation program has been developed, which can be found in [Liu].

Investigation on distributed MIMO systems under the multi-link COST 2100 model has been presented in Chapter 11. The sum-rate capacity of a dual-BS single-MS in a macrocell environment has been evaluated under different cluster BS-commonness ratio. By using ideal linear antenna arrays and defining single-direction MS movement, the evaluation has shown significant increase of the sum-rate outage capacity when the ratio of link-common clusters drops. This observation confirms the influence of the link correlation to the performance of distributed MIMO systems.

The future work on the multi-link channel modeling in cellular networks is expected to get improved on the following aspects:

1. Parameterization and validation of the COST 2100 model in various environments.

2. Multi-link modeling, parameterization, and validation by measurements in different link scales, i.e. with different number of BSs and MSs in the communications.

3. Geometry-based characterization of cluster link-commonness in multi-link COST 2100 models, i.e. the determination of cluster link connections based on the positions of BSs and VRs.

4. Full BS-independent and environmental centric channel modelings.

5. Cross-layer study of cooperative multi-link communications in more complex topologies.

Publications

Journals:

- Stéphane Van Roy, François Quitin, Lingfeng Liu, et al. Dynamic channel modeling and validation for multisensor body area networks, *Submitted to IEEE Trans. on Antennas and Propagation*, 2012

- Lingfeng Liu, J. Poutanen, et al. The COST 2100 channel model. *Submitted to IEEE Wireless Communications Magazine*, 2011

- Lingfeng Liu, R. D'Errico, et al. Dynamic Channel Modeling at 2.4 GHz for On-Body Area Networks. *Journal of Advances in Electronics and Telecommunications*, vol. 2(4), 2011

- Lingfeng Liu, F. Keshmiri, et al. An analytical modeling of polarized time-variant on-body propagation channels with dynamic body scattering. *EURASIP Journal on Wireless Communications and Networking*, vol. 2011, apr. 2011

Book chapter:

- (ed.) R. Verdone . *Pervasive Mobile & Ambient Wireless Communications, The COST Action 2100, Chapter 3: Radio Channel Modeling for 4G Networks*, 2011

Conference proceedings:

- Lingfeng Liu, V. Bhatnagar, et al. Investigation of channel spatial diversity for dual-link cooperative communications in WBAN. *In Proc. EUCAP*, pp.2972-2976, 11-15 April 2011

- Lingfeng Liu, J. Poutanen, et al. The COST 2100 channel model. *In Proc. JNCZW NEWCOM++/COST2100 Joint Workshop*, mar. 2011

- R. D'Errico, Lingfeng Liu, et al., Dynamic Channel Modeling at 2.4 GHz for On-Body Area Networks. *In Proc. JNCW NEWCOM++ / COST2100 Joint Workshop*, mar. 2011

- Lingfeng Liu, F. Keshmiri, et al. 3-D body scattering interference to vertically polarized on-body propagation. *In Proc. IEEE APS/URSI*, pp.1-4, 11-17, jul. 2010

- K. Haneda, J. Poutanen, Lingfeng Liu, et al. Comparison of delay and angular spreads between channel measurements and the COST 2100 channel model. *In Proc. LAPC 2010*, nov., 2010.

- A. Fort, Lingfeng Liu, et al. Analysis of wave propagation including shadow fading correlation for BAN applications, *In Proc. 2nd IET Seminar on Antennas and Propagation for Body-Centric Wireless Communications*. apr., 2009.

- Lingfeng Liu, S. Van Roy, et al. Azimuth radiation pattern characterization of omnidirectional antennas near a human body. *In Proc. ICEAA '09*, pp.461-464, 14-18 sep., 2009

- Lingfeng Liu, N. Czink, and C. Oestges. Implementing the COST 273 MIMO channel model. *In Proc. Newcom++ ACoRN Joint Workshop*, 2009

- Lingfeng Liu, P. De Doncker, et al. Fading correlation measurement and modeling on the front side of a human body. *In Proc. EuCAP*, pp.969-973, 23-27 mar. 2009

- X. Yin, Lingfeng Liu, et al. Modeling and estimation of the direction-delay power spectrum of the propagation channel. *In Proc. IS-CCSP*, 2008

COST 2100 action TDs

- Lingfeng Liu, J. Poutanen, et al. A multi-link extension of the COST2100 MIMO channel model. COST 2100 TD(10)11012, Aalborg, Denmark, 20-24 june, 2010

- Lingfeng Liu, F. Keshmiri, et al. 3-D body scattering interference to on-body propagation with polarized point source. COST 2100 TD(10)11013, Aalborg, Denmark, 20-24 june, 2010

- Lingfeng Liu, P. De Doncker, and C. Oestges. Time-variant On-body Channel Fading Characterization and Modelling with Dynamic Human Body. COST 2100 TD(09) 919, Wien, Austria, 28-30 sep., 2009

- Lingfeng Liu, C. Oestges, and N. Czink. The COST 273 Channel Model Implementation. COST 2100 TD(08) 638, Lille, France, 6-8 oct., 2008

- Lingfeng Liu, P. De Doncker, and C. Oestges. Fading Correlation Measurement and Modeling on the Front and Back side of a Human Body. COST 2100 TD(08) 642, Lille, France, 6-8 oct., 2008

- Lingfeng Liu, P. De Doncker, and C. Oestges. Fading correlation analysis for front abdomen propagation in body area networks. COST 2100 COST 2100 TD(08) 522, Trondheim, Norway, 6-8 oct., 2008

Bibliography

[3GP03] 3GPP TR 25.996 V6.1.0 (2003-09)technical report, 2003.

[AANH10] L. Akhoondzadeh-Asl, Y. Nechayev, and P.S. Hall. Surface and creeping waves excitation by body-worn antennas. In *Proc. LAPC 2010*, pages 48 –51, nov. 2010.

[Agi] http://www.home.agilent.com.

[AGM+06] H. Asplund, A.A. Glazunov, A.F. Molisch, K.I. Pedersen, and M. Steinbauer. The COST 259 directional channel model-part II: Macrocells. *IEEE Trans. on Wireless Communications*, 5(12):3434 –3450, dec. 2006.

[AHH+06] A. Alomainy, Y. Hao, X. Hu, C.G. Parini, and P.S. Hall. UWB on-body radio propagation and system modelling for wireless body-centric networks. *IEE Proceedings-Communications*, 153(1):107 – 114, feb. 2006.

[Ala98] S.M. Alamouti. A simple transmit diversity technique for wireless communications. *IEEE Jnrl. on Selected Areas in Communications*, 16(8):1451 –1458, oct 1998.

[ANP+09] J.B. Andersen, JO Nielsen, G.F. Pedersen, G. Bauch, and G. Dietl. Doppler spectrum from moving scatterers in a random environment. *IEEE Trans. on Wireless Communications*, 8(6):3270–3277, 2009.

[ANT] http://www.thisisant.com/ant/ant-alliance.

[AP09] P. Agrawel and N. Patwari. Correlated link shadowing fading in multi-hop wireless networks. *IEEE Trans. on Wireless Communication*, 8:4024–4036, 2009.

[APL11] T. Alves, B. Poussot, and J.-M. Laheurte. Analytical propagation modeling of BAN channels based on the creeping-wave theory. *IEEE Trans. on Antennas and Propagation*, 59(4):1269 –1274, april 2011.

[ASM64] M. Abramowitz, I. A. Stegun, and P. M. Morse. *Handbook of mathematical functions.* GPO, 1964.

[BKRL06] A. Bletsas, A. Khisti, D.P. Reed, and A. Lippman. A simple cooperative diversity method based on network path selection. *IEEE Jnrl. on Selected Areas in Communications*, 24(3):659 – 672, march 2006.

[CAG08] V. Chandrasekhar, J. Andrews, and A. Gatherer. Femtocell networks: a survey. *IEEE Communications Magazine*, 46(9):59 –67, september 2008.

[CBY07] N. Czink, E. Bonek, and J. Ylitalo. Parameterizing geometry-based stochastic MIMO channel models from measurements using correlated clusters. In *Proc. ITG/IEEE Workshop on Smart Antennas*, feb. 2007.

[CFGV02] D. Chizhik, G.J. Foschini, M.J. Gans, and R.A. Valenzuela. Keyholes, correlations, and capacities of multielement transmit and receive antennas. *IEEE Trans. on Wireless Communications*, 1(2):361 –368, apr 2002.

[CG79] T. Cover and A.E. Gamal. Capacity theorems for the relay channel. *IEEE Trans. on Information Theory*, 25(5):572 – 584, sep 1979.

[CH01] Nelson Costa and Simon Haykin. *Multiple-Input Multiple-Output Channel Models: Theory and Practice*. Wiley-Interscience, 2001.

[Che95] W. C. Chew. *Waves and Fields in Inhomogeneous Media.* New York: IEEE Press, 1995.

[CNHM10] S. Chamaani, Y.I. Nechayev, P.S. Hall, and S.A. Mirtaheri. In-body to off-body channel modelling. In *Proc. 2010 LAPC*, pages 609 –612, nov. 2010.

[Cor99] L. M Corria. Digital mobile radio towards future generation systems, COST 231 final report, 1999.

[Cor06] L. M. Correia. *Mobile Broadband Multimedia Networks.* Academic Press, 2006.

[CT91] T. M. Cover and J. A. Thomas. *Elements of Information Theory.* New York: John Wiley & Sons, Inc., 1991.

[CTea09] Y. Chen, J. Teo, and et al. Cooperative Communications in Ultra-Wideband Wireless Body Area Networks: Channel Modeling and System Diversity Analysis. *IEEE Jnrl. on Selected Areas in Communications*, 27(1):5 –16, jan. 2009.

[dCI05] A. del Coso and C. Ibars. Capacity of decode-and-forward cooperative links with full channel state information. In *Proc. Conference Record of the Thirty-Ninth Asilomar Conference on Signals, Systems and Computers*, pages 1514 – 1518, 28 - november 1, 2005.

[DE01] V. Degli-Esposti. A diffuse scattering model for urban propagation prediction. *IEEE Trans. on Antennas and Propagation*, 49(7):1111 –1113, jul. 2001.

[DO09] R. D'Errico and L. Ouvry. Time-variant ban channel characterization. In *Proc. IEEE 20th PIMRC*, pages 3000 –3004, sep. 2009.

[DO11] R. D'Errico and L. Ouvry. Doppler characteristics and correlation proprieties of on-body channels. In *Proc. 5th EUCAP*, pages 2977 –2981, april 2011.

[DPB01] K. Van Dam, S. Pitchers, and M. Barnard. Body area networks: Towards a wearable future. In *Proc. WWRF kick off meeting, Munich, Germany*, 6-7 march 2001.

[ea07] IST-WINNER D1.1.2 P. Kyösti et al. WINNER II channel models, ver 1.1, 2007.

[Els94] Atef Z. Elsherbeni. A comparative study of two-dimensional multiple scattering techniques. *Radio Sci.*, 29(4), 1994.

[FDR+05] A. Fort, C. Desset, J. Ryckaert, P. De Doncker, L. Van Biesen, and S. Donnay. Ultra wide-band body area channel model. In *Proc. IEEE ICC*, volume 4, pages 2840 – 2844, may 2005.

[FKC+10] A. Fort, F. Keshmiri, G.R. Crusats, C. Craeye, and C. Oestges. A body area propagation model derived from fundamental principles: Analytical analysis and comparison with measurements. *IEEE Trans. on Antennas and Propagation*, 58(2):503 –514, feb. 2010.

[FLK+09] A. Fort, L. Liu, F. Keshmiri, P. De Doncker, C. Oestges, and C. Craeye. Analysis of wave propagation including shadow fading correlation for ban applications. In *Proc. 2nd IET Seminar on Ant. and Prop. for Body-Centric Wireless Communications*, pages 1 –28, apr. 2009.

[GA08] A. Gupta and T.D. Abhayapala. Body area networks: Radio channel modelling and propagation characteristics. In *Proc. Australian Communications Theory Workshop (AusCTW) 2008*, pages 58 –63, jan. 2008.

[GGV+09] J.-M. Gorce, C. Goursaud, G. Villemaud, R. D'Errico, and L. Ouvry. Opportunistic relaying protocols for human monitoring in ban. In *Proc. IEEE 20th PIMRC*, pages 732 –736, sept. 2009.

[GJJV03] A. Goldsmith, S.A. Jafar, N. Jindal, and S. Vishwanath. Capacity limits of mimo channels. *IEEE Jnrl. on Selected Areas in Communications*, 21(5):684 – 702, june 2003.

[G.N22] Watson G.N. *Theory of Bessel Functions*. Cambridge at the University Press, 1922.

[Gud91] M. Gudmundson. Correlation model for shadowing fading in mobile radio system. *IEEE Electronics Letters*, 27(23):2145–2146, November 1991.

[HAZ+06] Yang Hao, A. Alomainy, Yan Zhao, C.G. Parini, Y. Nechayev, P. Hall, and C.C. Constantinou. Statistical and deterministic modelling of radio propagation channels in WBAN at 2.45 GHz. In *Proc. IEEE APS Int. Symp.*, pages 2169 –2172, jul. 2006.

[HH06] P. S. Hall and Y. Hao. *Antennas and propagation for body-centric wireless communications*. Artech House Publishers, 2006.

[HMRG09] L.W. Hanlen, D. Miniutti, D. Rodda, and B. Gilbert. Interference in body area networks: Distance does not dominate. In *Proc. IEEE 20th PIMRC*, pages 281 –285, sept. 2009.

[HPL+10] K. Haneda, J. Poutanen, Lingfeng Liu, C. Oestges, F. Tufvesson, and P. Vainikainen. Comparison of delay and angular spreads between channel measurements and the COST2100 channel model. In *Proc. 2010 LAPC*, pages 477 –480, nov. 2010.

[HPT+11] K. Haneda, J. Poutanen, F. Tuvfesson, L. Liu, V. Kolmonen, P. Vainikainen, and C. Oestges. Development of multi-link geometry-based stochastic channel models. In *Proc. LAPC, 2011 Loughborough*, pages 1 –7, nov. 2011.

[Ibe05] Oliver Ibe. *Fundamentals of Applied Probability and Random Processes*. Academic Press, 2005.

[IEE] http://ieee802.org/15/pub/tg6.html.

[IXTS09] K. Ito, W. Xia, M. Takahashi, and K. Saito. An implanted cavity slot antenna for medical communication systems. In *Proc. 3rd EuCAP*, pages 718 –721, march 2009.

[KC10] Farshad Keshmiri and Christophe Craeye. Wave propagation from sources with arbitrary polarization next to the human body. In *Proc. IEEE Int. Symp. APS/USNC/URS*, jul. 2010.

[KFV06] M.K. Karakayali, G.J. Foschini, and R.A. Valenzuela. Network coordination for spectrally efficient communications in cellular systems. *IEEE Wireless Communications*, 13(4):56 –61, aug. 2006.

[KHea10] V.-M. Kolmonen, K. Haneda, and et al. Measurement-based evaluation of interlink correlation for indoor multi-user mimo channels. *IEEE Anetenna and Wireless Propagation Letters*, 9(2):311–314, apr 2010.

[KMY07] G. Kramer, I. Marić, and R. D. Yates. *Cooperative Communications (Foundations and Trends in Networking)*. Now Publishers Inc., 2007.

[LDDO09] L. Liu, P. De Doncker, and C. Oestges. Fading correlation measurement and modeling on the front side of a human body. In *Proc. 3rd EuCAP*, pages 969 –973, mar. 2009.

[LhH09] Y.-L. Li and Z. h. Huang. Modeling of body area network in medical healthcare applications. In *Proc. IEEE Int. Symp. on ITIME '09.*, volume 1, pages 100 –104, aug. 2009.

[Liu] L. Liu. A public cost 2100 channel model matlab source code,. 2010. [Online]. Available: http://ftp.COST2100.org/WG2.3 Model/.

[LLR10] M. Li, W. Lou, and K. Ren. Data security and privacy in wireless body area networks. *IEEE Wireless Communications*, 17(1):51 –58, february 2010.

[LTW04] J.N. Laneman, D.N.C. Tse, and G.W. Wornell. Cooperative diversity in wireless networks: Efficient protocols and outage behavior. *IEEE Trans. on Information Theory*, 50(12):3062 – 3080, dec. 2004.

[LVRDDO09] Lingfeng Liu, S. Van Roy, P. De Doncker, and C. Oestges. Azimuth radiation pattern characterization of omnidirectional antennas near a human body. In *Proc. ICEAA*, pages 461 –464, sep. 2009.

[MAH+06] A.F. Molisch, H. Asplund, R. Heddergott, M. Steinbauer, and T. Zwick. The COST259 directional channel model-part i: Overview and methodology. *IEEE Trans. on Wireless Communications*, 5(12):3421 –3433, dec. 2006.

[MB00] J. Medbo and J.-E. Berg. Simple and accurate path loss modeling at 5 GHz in indoor environments with corridors. In *Proc. IEEE 52nd VTS-Fall VTC 2000.*, volume 1, pages 30–36, 2000.

[MBea04] A. F. Molisch, K. Balakrisnan, and et al. IEEE 802.15.4a channel model - final report. 2004.

[MCC+06] A.F. Molisch, D. Cassioli, Chia-Chin Chong, S. Emami, A. Fort, B. Kannan, J. Karedal, J. Kunisch, H.G.

Schantz, K. Siwiak, and M.Z. Win. A comprehensive standardized model for ultrawideband propagation channels. *IEEE Trans. on Antennas and Propagation*, 54(11):3151 –3166, nov. 2006.

[MTKM09] A.F. Molisch, F. Tufvesson, J. Karedal, and C. Mecklenbrauker. Propagation aspects of vehicle-to-vehicle communications - an overview. In *Proc. IEEE RWS '09.*, pages 179 –182, jan. 2009.

[MZ09] D. Ma and W.X. Zhang. Analytic propagation model for body area network channel based on impedance boundary condition. In *Proc. 3rd EuCAP*, pages 974 –978, mar. 2009.

[NBK04] R.U. Nabar, H. Bolcskei, and F.W. Kneubuhler. Fading relay channels: performance limits and space-time signal design. *IEEE Jnrl. on Selected Areas in Communications*, 22(6):1099 – 1109, aug. 2004.

[NG06] C.T.K. Ng and A.J. Goldsmith. Capacity and power allocation for transmitter and receiver cooperation in fading channels. In *Proc. ICC '06.*, volume 8, pages 3741 –3746, june 2006.

[NHH04] A. Nosratinia, T.E. Hunter, and A. Hedayat. Cooperative communication in wireless networks. *IEEE Communications Magazine*, 42(10):74 – 80, oct. 2004.

[OC07] Claude Oestges and Bruno Clerkx. *MIMO Wireless Communications: From Real-World Propagation to Space-Time Code Design.* Academic Press; 1 edition, 2007.

[OC10] C. Oliveira and L.M. Correia. A statistical model to characterize user influence in body area networks. In *Proc. IEEE 72nd VTC 2010-Fall*, pages 1 –5, sept. 2010.

[Pap91] Athanasios Papoulis. *Probablity, Random Variables, and Stochastic Processes.* McGraw-Hill Companies, 1991.

[PG03] A. Paulraj and D. Gore. *Introduction to Space-Time Wireless Communications.* Cambridge University Press, 2003.

[PHL+10] J. Poutanen, K. Haneda, L. Liu, C. Oestges, F. Tufvesson, and P. Vainikainen. Inputs for the cost2100 multi-link channel model implementation. Technical Report TD(10)10067, COST2100, Athens, Greece, Feb. 2010.

[PHL+11] J. Poutanen, K. Haneda, Lingfeng Liu, C. Oestges, F. Tufvesson, and P. Vainikainen. Parameterization of the COST 2100 mimo channel model in indoor scenarios. In *Proc. 5th EUCAP*, pages 3606 –3610, april 2011.

[PHS+10] J. Poutanen, K. Haneda, J. Salmi, V. Kolmonen, F. Tufvesson, T. Hult, and P. Vainikainen. Significance of common scatterers in multi-link indoor radio wave propagation. In *Proc. 4th EuCAP*, pages 1 –5, april 2010.

[Pou11] J. Poutanen. Geometry-based radio channel modeling: Propagation analysis and concept development, mar. 2011.

[Pro00] John Proakis. *Digital Communications 4th edition*. McGraw-Hill Science/Engineering/Math, 2000.

[PSH+10] J. Poutanen, J. Salmi, K. Haneda, V. Kolmonen, F. Tufvesson, and P. Vainikainen. Propagation characteristics of dense multipath components. *IEEE Antennas and Wireless Propagation Letters*, 9:791 –794, 2010.

[PSH+11] J. Poutanen, J. Salmi, K. Haneda, V. Kolmonen, and P. Vainikainen. Angular and shadowing characteristics of dense multipath components in indoor radio channels. *IEEE Trans. on Antennas and Propagation*, 59(1):245 –253, jan. 2011.

[PTH+10] J. Poutanen, F. Tufvesson, K. Haneda, L. Liu, C. Oestges, , and P. Vainikainen. Adding dense multipath components to the COST 2100 MIMO channel model. Technical Report TD(10)10067, COST2100, Athens, Greece, Feb. 2010.

[QOHDD10] F. Quitin, C. Oestges, F. Horlin, and P. De Doncker. A polarized clustered channel model for indoor multi-antenna systems at 3.6 GHz. *IEEE Trans. on Vehicular Technology*, 59(8):3685 –3693, oct. 2010.

[R.02] Theodore S. R. *Wireless Communications: Principles and Practice.* Prentice Hall, 2002.

[RDDM+04] J. Ryckaert, P. De Doncker, R. Meys, A. de Le Hoye, and S. Donnay. Channel model for wireless communication around human body. *Electronics Letters*, 40(9):543 – 544, april 2004.

[Rei09] A. Reichman. Standardization of body area networks. In *Proc. IEEE COMCAS 2009.*, pages 1 –4, nov. 2009.

[RJV+07] E. Reusens, W. Joseph, G. Vermeeren, L. Martens, B. Latre, I. Moerman, B. Braem, and C. Blondia. Path loss models for wireless communication channel along arm and torso: measurements and simulations. In *Proc. IEEE APS*, pages 345 –348, jun. 2007.

[SAF+08] M. Sukor, S. Ariffin, N. Fisal, S.K.S. Yusof, and A. Abdallah. Performance study of wireless body area network in medical environment. In *Proc. 2nd AICMS 08*, pages 202 –206, may 2008.

[Sch92] R.W. Scharstein. Acoustic scattering from two parallel soft cylinders. In *Proc. IEEE Southeastcon '92*, pages 534 –537 vol.2, April 1992.

[SL03] H. Shin and J. H. Lee. Capacity of multiple-antenna fading channels: spatial fading correlation, double scattering, and keyhole. *IEEE Trans. on Information Theory*, 49(10):2636 – 2647, oct. 2003.

[Sør99] T.B. Sørensen. Slow fading cross-correlation against azimuth separation of base station. *IEEE Electronics Letters*, 35(2):127–128, January 1999.

[SPYH+09] K. Sayrafian-Pour, Wen-Bin Yang, J. Hagedorn, J. Terrill, and K.Y. Yazdandoost. A statistical path loss model for medical implant communication channels. In *Proc. IEEE 20th PIMRC*, pages 2995 –2999, sept. 2009.

[Ver11] (ed.) R. Verdone. *Pervasive Mobile & Ambient Wireless Communications, The COST Action 2100.* Springer, 2011.

[VLODD09] S. Van Roy, Lingfeng Liu, C. Oestges, and P. De Doncker. An ultra-wideband SAGE algorithm for body area networks. In *Proc. ICEAA'09*, pages 584 –587, sep. 2009.

[vROHDD10] S. van Roy, C. Oestges, F. Horlin, and P. De Doncker. A comprehensive channel model for UWB multisensor multiantenna body area networks. *IEEE Trans. on Antennas and Propagation*, 58(1):163 –170, jan. 2010.

[WCL09] C.-X. Wang, X. Cheng, and D. Laurenson. Vehicle-to-vehicle channel modeling and measurements: recent advances and future challenges. *IEEE Communications Magazine*, 47(11):96 –103, november 2009.

[WHG+10] C.-X. Wang, X. Hong, X. Ge, X. Cheng, G. Zhang, and J. Thompson. Cooperative mimo channel models: A survey. *IEEE Communications Magazine*, 48(2):80 –87, february 2010.

[WTN06] Z. Wang, E. K. Tameh, and A. Nix. Simulating correlated shadowing signals in mobile multihop relay/ad-hoc networks. Tech Report IEEE C802.16j-06/060, IEEE 802.16 Broadband Wireless Access Working Group, July 2006.

[XZ09] Jiang Xing and Yunru Zhu. A survey on body area network. In *Proc. 5th International Conference on WiCom '09.*, pages 1 –4, sept. 2009.

[YH10] Kamya Yekeh Yazdandoost and Kiyoshi Hamaguchi. Antenna polarization mismatch in body area network communications. In *Proc. 4th EuCAP*, pages 1 –4, apr. 2010.

[YK06] K.Y. Yazdandoost and R. Kohno. UWB antenna for wireless body area network. In *Proc. APMC 2006*, pages 1647 –1652, dec. 2006.

[YK07] K. Yekeh and R. Kohno. Wireless communications for body implanted medical device. In *Proc. APMC 2007.*, pages 1 –4, dec. 2007.

[ZD04] H. Zhang and H. Dai. A geometrically based model for line-of-sight multipath radio channels. In *Proc. 38th CISS 2004, Princeton University, New Jersey*, pages 83–88, March 17-19 2004.

[ZHAP06] Yan Zhao, Yang Hao, A. Alomainy, and C. Parini. UWB on-body radio channel modeling using ray theory and sub-band FDTD method. *IEEE Trans. on Microwave Theory and Techniques*, 54(4):1827 – 1835, jun. 2006.

[Zig] http://www.zigbee.org/.

[ZLK07] Bin Zhen, Huan-Bang Li, and R. Kohno. Ieee body area networks for medical applications. In *Proc. 4th ISWCS 2007.*, pages 327 –331, oct. 2007.

[ZSH+09] Y. Zhao, A. Sani, Y. Hao, S.-L. Lee, and G.-Z. Yang. A simulation environment for subject-specific radio channel modeling in wireless body sensor networks. In *Proc. 6th Int. Workshop on Wearable and Implantable Body Sensor Networks (BSN)*, pages 23 –28, jun. 2009.

[ZT03] L. Zheng and D.N.C. Tse. Diversity and multiplexing: a fundamental tradeoff in multiple-antenna channels. *IEEE Trans. on Information Theory*, 49(5):1073 – 1096, may 2003.